EFFECTS OF ION IRRADIATION ON THE SURFACE MECHANICAL BEHAVIOR OF HYBRID SOL-GEL DERIVED SILICATE THIN FILMS

By

RUDY GHISLENI

Master of Science
Oklahoma State University
Stillwater, Oklahoma
2001

Laurea in Ingegneria Meccanica
Politecnico di Milano
Milano, Italy
2002

Submitted to the Faculty of the
Graduate College of the
Oklahoma State University
in partial fulfillment of
the requirements for
the Degree of
DOCTOR OF PHILOSOPHY
May, 2007

EFFECTS OF ION IRRADIATION ON THE SURFACE MECHANICAL BEHAVIOR OF HYBRID SOL-GEL DERIVED SILICATE THIN FILMS

Thesis Approved:

Don A. Lucca

Thesis Adviser

C. Eric Price

Daniel R. Grischkowsky

Eduardo A. Misawa

A. Gordon Emslie

Dean of the Graduate College

ACKNOWLEDGMENTS

I would like to thank my adviser Prof. Don A. Lucca, a dedicated professor who taught me the fundamentals that are so important to original scientific thought and for his constant readiness to advise me in my academic research. I would also like to thank my committee members, Prof. C. Eric Price, Prof. Daniel R. Grischkowsky, and Prof. Eduardo A. Misawa for their willingness to share their time and expertise in providing critical and constructive suggestions which improved this work. I extend my thanks to Dr. Michael Nastasi[1] for his intellectual guidance and stimulating ideas. I express my appreciation to Prof. Ekkard Brinksmeier[2] and Prof. Hans-Werner Zoch[2] for their direction of this work as part of the DFG Transregionaler Sonderforschungsbereich SFB/TR4. Additional thanks are extended to Drs. Andreas Mehner[2] and Juan Dong[2], and Mr. Walter Datchary[2] for the design and production of the sol-gel films and for their comments and suggestions, as well as to Drs. Lin Shao[1] and Yongqiang Q. Wang[1] for their assistance with the ion irradiation and elastic recoil detection experiments. I would like to thank my colleagues, Mr. Vu Doan, Dr. Matthew J. Klopfstein, Dr. David W. Hamby, Dr. Sedat Kilic, Mr. Ashay Gude, Mr. Oscar Mejia, Mr. Luca Rossettini, Mr. Tres Harriman, Mr. Benjamin Dvorak, and Ms. Golnaz Bassiri for all their help.

This work is dedicated both to my wife and friend for life, Marie Christine, and my Lord and Savior, Jesus Christ, to whom I am infinitely grateful for their encouragement and support. Without them this work could not be completed. A special thought to our daughter Léonie.

Un ringraziamento particolare va ai miei genitori, papá Mauro e mamma Lory, per il costante supporto ed incoraggiamento mostratomi durante questi quattro anni. I loro insegnamenti di vita mi hanno consentito di raggiungere questo traguardo.

The financial support of the National Science Foundation through Grant Nos. OISE-0352377 and OISE-0128050 is gratefully acknowledged. The funding for the Transregionaler Sonderforschungsbereich SFB/TR4 by the Deutsche Forschungsgemeinschaft is also gratefully acknowledged. I would also like to acknowledge the Oklahoma State Regents for Higher Education and the Noble Foundation for the funding provided. Sincere thanks to the support of the Thomas J. Cunningham Distinguished Graduate Fellowship.

[1]Los Alamos National Laboratory, Los Alamos, NM, USA
[2]Stiftung Institut für Werkstofftechnik (IWT), Bremen, Germany

TABLE OF CONTENTS

LIST OF FIGURES

LIST OF TABLES

NOMENCLATURE

MTES	MethylTriEthoxySilane
TEOS	TetraEthOxySilane
UV	Ultra Violet
PVP	PolyVinylPyrrolidone
PL	PhotoLuminescence
LUMO	Lowest Unoccupied Molecular Orbital
HOMO	Highest Occupied Molecular Orbital
CCD	Charge-Coupler Device
ERD	Elastic Recoil Detection
XPS	X-ray Photoelectron Spectroscopy
AFM	Atomic Force Microscopy
D	Diameter, m
NA	Numerical Aperture
BP	Band-Pass
ν_p	Pinhole Size
λ	Wavelength, nm
d_0	Optical Fiber Diameter, nm
O_m	Objective Magnification
PR	Ion Projected Range, nm
E_0	Ion Incident Energy, keV (J)
ϕ	Ion Fluence, ions/cm^2
$\bar{\phi}$	Ion Fluence Constant, ions/cm^2
σ	Hardening Cross-Section, cm^2
$\bar{\sigma}$	Hardening Cross-Section Constant, cm^2
a	Hardening Coefficient, non-dimensional
Z_1^*	Incident Ion Ionization
Z	Atomic Number

v ..... Velocity, m/s

T ..... Kinetic Energy, J

Δp ..... Momentum, kg m/s

F_0 ..... Interaction Force, N

$V(r)$ ..... Interaction Potential, N m

k_c ..... Coulomb Force Constant, 8.988 x 10^9 Nm^2C^{-2}

e ..... Unit Charge, 1.602 x 10^{-19} C

r ..... Radius, m

m_e ..... Electron Mass 9.1095×10^{-31} kg

p_H ..... Hard Collision Probability H^+ - electron

p_N ..... Hard Collision Probability N^{2+} - electron

Chapter 1

Introduction

The volume production of complex optics (Fresnel lenses, aspherical optics, etc.) requires wear resistant molds with microstructured features. Wear resistant materials like ceramics are difficult to machine since they are very brittle, therefore limiting the ability to obtain microstructured features on the molds. One of the possible solutions to this problem is the use of sol-gel films that can be structured in the green ceramic state and then heat treated or ion irradiated into hard ceramic films.

The sol-gel technology used to produce the thin films analyzed throughout this study is an alternative process to both sintering and sputtering to obtain coatings of refractory ceramics. The main advantages of this technique are low processing temperature, high workability in the green ceramic state, high purity and homogeneity [1].

Sol-gel processes are based on the synthesis of molecules that possess an inorganic backbone and an organic side group. The organic side groups are eliminated during the condensation of the gel film which can be accomplished either by heat treatment or ion irradiation. During condensation the gel passes from a state referred to as a "green ceramic", characterized by high malleability, to a ceramic state, characterized by high hardness and brittleness. The green ceramic state allows the films to be shaped before being transformed into a ceramic.

Sol-gel films have found numerous applications such as magnetic recording disk coatings, biomedical and prosthetic coatings, sensor films, high reflectivity coatings for optical applications, and thermal barrier and wear resistant coatings for turbine blades.

Sol-gel synthesis has been reported to produce films with fine-scaled microstructure. Pore and particle sizes of two nanometers can easily be obtained in freshly derived gels [2]. The ability of sol-gel synthesis to produce nanoscale structures allows for the study of the changes in the mechanical and optical response of a structure due to changes in the dimensions of a structure.

This study focuses on the investigation of organic/inorganic MTES/TEOS (methyltriethoxysilane/ tetraethoxysilane) sol-gel derived films for potential use as wear resistant coatings. These hybrid films were preferred to inorganic films in order to obtain thicker crack-free films. The drawback of inorganic films like ZrO_2 is in their thin critical film thickness of about 150 nm, which made them unusable. Critical film thickness refers to the maximum crack-free film thickness that can be obtained after the evaporation of the solvent. Film thickness is an important parameter for the wear resistant mold application since the films need to be machined by diamond tools, and the minimum film thickness required by the machining process was evaluated to be 5-10 μm [3]. Molecular manipulation of inorganic microstructures using organic molecules (hybrid materials) has been reported to reduce the stresses during condensation and heat treatment, resulting in higher critical film thicknesses (20-30 μm). The drawback of the hybrid films is the decrease in mechanical properties leading to lower wear resistance; this issue has been addressed in this study by introducing the ion irradiation process in the condensation stage. Hybrid sol-gel films also offer the possibility to control the inorganic microstructures through the use of selected organic molecules, therefore representing a very powerful tool for the design of novel materials [4].

1.1 Objectives

This study is part of a Transregional Co-operative Research Project including the University of Bremen, Germany, the Technical University of Aachen, Germany, and Oklahoma State University. The overall goal of the project is the design of high wear resistant coatings for molds used in replication of high complexity optical components. The two main specifications required by the coating are good wear resistance (Berkovich hardness greater than 3 GPa) and a film thickness greater than 5 μm allowing the film to be diamond machined.

The objective of this work is centered on the understanding of the fundamental science governing the hardening process of the ion irradiated sol-gel derived films. In particular, attention is focused on the role played by the electronic and nuclear stopping power on the hardening process. The cause of the observed hardening will also be considered, analyzing the variation in structure by Raman spectroscopy.

1.2 Contributions

The contributions of this work are in the following four areas: characterization of the sol-gel system before and after ion irradiation, understanding the role of electronic and nuclear stopping power on the hardening process, modeling of the hardening process, and analysis of the cause behind the hardening process.

The characterization tools used for this study include nanoindentation, atomic force microscopy, photoluminescence spectroscopy and Raman spectroscopy. The nanoindentation instrument enabled the measurement of the reduced elastic modulus and hardness of the films. Atomic force microscopy was used to measure not only the topography of the films, but also to measure the film thickness variation between the non-irradiated and the irradiated films. Photoluminescence spectroscopy allowed the characterization of the light emission of the films while Raman spectroscopy allowed determination of the presence of C-C bond formation after irradiation. Raman spectroscopy was also used to differentiate between the formation of graphite and diamond-like structure.

This study indicates that electronic stopping is principally responsible for the film conversion (hardening), and that the role of nuclear stopping is minimal in this regard. A linear dependence of both hardness and hydrogen loss with electric stopping power was observed.

A model describing the effectiveness of various ion species and fluencies on the hardening process has been put forth. This model is based on Gibbons' study [5] on the amorphization of crystalline material by ion irradiation.

The hypotheses formulated on the cause of the mechanical hardening of the sol-gel films by ion irradiation are: 1.) a cross-linking mechanism and 2.) the formation of diamond-like structure. Both of these hypotheses have been investigated in this study.

Chapter 2

Background

2.1 Sol-Gel Derived Thin Films

The sol-gel technique is used to obtain ceramic like coatings as an alternative route to sintering and sputtering. The term sol-gel can be broadly defined as the preparation of ceramic materials by producing a sol (colloidal suspension of solid particles in a liquid), gelation of the sol and removal of the solvent. Figure 2.1 shows the sol-gel process for a spin coating deposition. The sol produced (liquid form) is shown in a beaker. The gelation and solvent removal are going to take place as soon as the sol is deposited on the substrate transforming the sol in gel. After sintering or ion irradiation, the gel transforms into a ceramic film.

2.1.1 Sol Preparation

The starting compounds (precursors) used to prepare the sol consist of a metal (e.g., Zr) or metalloid (e.g. Si) element surrounded by various ligands which can be inorganic or organic. In this study, only organic ligands such as alkoxy (ethoxy $\bullet OCH_2CH_3$) and alkyl (methyl $\bullet CH_3$) were used.

Alkoxy ligands are often used because they react readily with water. This reaction is called hydrolysis as it results in the replacement of a ligand with a hydroxyl ion:

$$Me(OR)_4 + H_2O \rightarrow HO\text{-}Me(OR)_3 + ROH \tag{2.1}$$

where Me represents the metal or metalloid element, OR represents the ligand (OR is an alkoxy group while R alone is an alkyl group), and ROH is an alcohol. Two partially hydrolyzed molecules

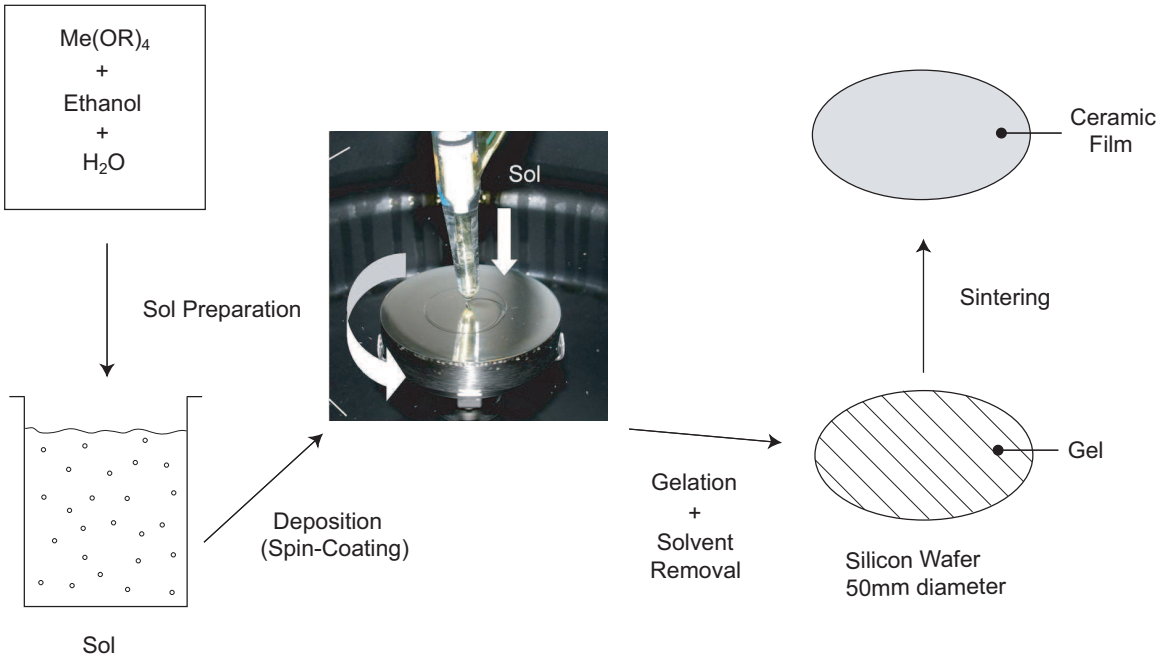

Figure 2.1: Sol-Gel process

can link together in a condensation reaction such as:

$$(OR)_3Me\text{-}OH + HO\text{-}Me(OR)_3 \rightarrow (OR)_3Me\text{-}O\text{-}Me(OR)_3 + H_2O \tag{2.2}$$

or

$$(OR)_3Me\text{-}OR + HO\text{-}Me(OR)_3 \rightarrow (OR)_3Me\text{-}O\text{-}Me(OR)_3 + ROH \tag{2.3}$$

Alkyl groups do not react in water, thus they do not actively participate in the hydrolysis reaction. Alkyl ligands are usually used as a condensation block in order to control the size of the molecule generated through condensation.

2.1.2 Gelation and Solvent Removal

A monomer that can make more than two bonds has no limit on the size of the molecule that can form during condensation. If such a molecule reaches a macroscopic dimension extending throughout the solution, the substance is then called a gel. Thus, a gel is a state that contains a continuous solid skeleton enclosing a continuous liquid phase.

Gelation and solvent removal overlap in the case of film deposition. For bulk systems, the condensation, gelation and drying are separate events that might take weeks to complete, whereas in films they occur in seconds to minutes during dipping or spinning deposition. After deposition,

the resulting thin film is in the so called green ceramic state. This state is characterized by a good malleability compared to the final ceramic state, which is reached by further elimination of the liquid phase and organic components (in the case of a hybrid sol) present in the gel. Heat treatment is a process of densification whose goal is the reduction of the solid-vapor interfacial area. In gels, that area is extremely large, so the driving force (interfacial energy) is great enough to densify the film at a relatively low temperature. Higher temperatures (greater than 400 °C) or, as it will be discussed in this study, ion irradiation are needed to eliminate the organic components remaining in the film after densification. Heat treatment and ion irradiation result in film hardening.

2.1.3 Thickness Limitations

The cracking in sol-gel films is caused by the stress related to the volumetric shrinkage and by capillary forces arising from the evaporation of the solvent [6]. One way to decrease the stresses during shrinkage is by producing organic/inorganic hybrid sol-gel films through the introduction of organic components during the synthesis of the sol-gel solution. The film thickness of hybrid sol-gel films can reach two orders of magnitude higher than that of inorganic sol-gel films. However, such an increase in thickness leads to a reduction in hardness (estimated to be an order of magnitude [7]).

2.2 Hybrid Silica Based Sol-Gel Films

Molecular manipulation of inorganic microstructures using organic molecules (hybrid materials) has been reported to reduce the stresses during condensation and heat treatment, resulting in a higher critical film thickness (20-30 μm) [6]. Moreover, hybrid sol-gel films offer the possibility to control the inorganic microstructures through the use of selected organic molecules, therefore representing a very powerful tool for the design of novel materials [4]. The drawback of the hybrid films is the decrease in mechanical properties leading to lower wear resistance. This limitation can be addressed by novel process techniques like ion irradiation employed in this study.

A literature review on the applications, structural evolution, mechanical properties, photoluminescence and Raman spectroscopy, ion irradiation, and UV irradiation of hybrid silica based sol-gel films is reported below.

2.2.1 Applications

Hybrid sol-gel thin films have found application in many fields such as mechanical, optical and electrical.

The two main mechanical applications are wear/abrasion resistance and corrosion protection [8]. The substrates that have employed hybrid silica sol-gel films for wear resistance purposes are mostly glasses and polymers [9–11].

Concerning optical applications, hybrid sol-gel films have been used as photonic materials since they can be produced with a tailored refractive index and a thickness up to 22 μm. The refractive index can be controlled by varying the organic molecule type and concentration [6]. Thus, these types of films were used in integrated optical circuits for passive and active data processing devices [12] (the refractive index of these films ranged from 1.40 to 1.55). Optical memory disks were also obtained using a mixture of methyltriethoxysilane (MTES) and tetraethoxysilane (TEOS) on a glass substrate [13]. Hybrid sol-gel films have often been used as a host matrix for guest molecules that have desired optical properties, such as coumarin-4 which has been used as gain media for laser materials, non-linear optical materials and optical memory [14].

Hybrid sol-gel films can also be produced with a very low dielectric constant, which is a requirement for resistance-capacitance coupling used in electrical fields [15].

2.2.2 Structure

Before introducing the structure of a TEOS/MTES mixture sol (the system investigated throughout this study) a simpler structure which results from pure TEOS sol will be briefly described. In this case, the Si-O-Si network is built from the Si-(O-C_2H_5)$_4$ tetrahedral configuration once the ethyl group (C_2H_5) concentration is drastically reduced during hydrolysis and condensation of the film, as described in greater detail in Section 2.1. The ethyl group (C_2H_5) disappears almost completely after heat treatment (around 250 °C [16]) allowing for the reconstruction of an amorphous SiO_2 network. Silica based sol-gel films contain an amorphous structure up to 1350 °C [17].

The introduction in the TEOS precursor with one or more organic groups attached to the silicon by a non-hydrolysable bond (like in MTES) is a way to incorporate organic molecules in the material [18]. In the MTES precursor, a methyl group (CH_3) replaces one of the oxygen-ethyl group (O-C_2H_5), thus leading to the formation of Si-C bonds. The Si-C bond is not affected by hydrolysis but it can be broken at about 500 °C by oxidation (reaction with oxygen), or at around 700 °C by thermal cracking. In Santucci et al. [19], it is shown that the Si-C bond is broken at 500 °C, with the consequent loss of the methyl group. Other researchers reported the loss of CH_3 at 450 °C [16, 20, 21].

After heat treatment above 500 °C, the end product of TEOS and TEOS/MTES sols appear to

be the same: amorphous SiO_2. The major difference is the presence of organic components up to approximately 500 °C for the TEOS/MTES sol. The gradual decomposition of the organic components with heat treatment is the key point in the reduction of the stress related to the volumetric shrinkage during heat treatment and, thus, resulting in film thicknesses two orders of magnitude higher than that of inorganic sol-gel films (TEOS sol) [18].

The literature review on the effect of heat treatment on the hydrolysis byproduct (hydroxyl group), the catalyst (acetylacetone), and the binder (polyvinylpyrrolidone, PVP) is also reported.

After the hydrolysis of both TEOS and MTES precursor molecules is completed, many hydroxyl (OH) groups are bound to Si through substitution of one of the Si-O bonds [19]. These groups can either be free or bridged [16]. In the first case, the OH group is bound to one Si atom, whereas in the second case, the OH group is bound to two Si atoms through a hydrogen bond. It has been shown that the number of OH groups decreases with increasing heat treatment temperature, and that the relative concentration between free and bridged groups changes with increasing heat treatment temperature. In particular, the OH groups are in the bridge form for temperatures up to 100 °C, the remaining OH groups are mainly in the free form for temperatures higher than 300 °C, and the OH disappears almost completely [16] for temperatures higher than 500 °C. The silanol groups (Si-OH) were reported to burn out completely between 500 and 600 °C [18] with most of the loss occurring around 375 °C [22].

The thermo stability of polyvinylpyrrolidone (PVP) is reported to be up to approximately 450 °C [23–25], while acetylacetone evaporates at 150-250 °C [23]. These two elements are used in the synthesis of the films studied in this work. The first is used as a binder and the second as a catalyst.

PVP is a water-soluble macromolecular compound with strong bonding ability. This polymer is added to the solution in order to create a flexible binder capable of absorbing the stresses generated during heat treatment, resulting in crack-free films [23, 26]. PVP molecules bond with the inorganic molecules through a hydrogen bond between the C=O groups, present in the PVP molecules, and a hydrogen termination of the silica clusters in the form of Si-H, Si-OH or $Si-CH_3$ [24, 25].

2.2.3 Mechanical Properties

The values of reduced elastic modulus and hardness published in the literature for sol-gel derived thin films similar to those used in this study are here reported.

Yu et al. [15] investigated the reduced elastic modulus and hardness (measured by a Berkovich indenter) for a series of films heat treated at 450 °C and with various ratios of MTES/TEOS. The

extrapolated values of reduced elastic modulus and hardness for a MTES/TEOS ratio of 1.5 are 5 GPa and 0.5-0.75 GPa, respectively. The values reported here have been extrapolated since the value reported by Yu et al. are for MTES/TEOS ratios equal to 1 and 2. Also, Matsuda et al. [13] evaluated the hardness of sol-gel films prepared with various ratios of MTES/TEOS and various heat treatment temperatures ranging from room temperature up to 600 °C and at holding times of 30 minutes. Since these experiments were conducted using a dynamic ultra-microhardness tester, which uses a different indenter shape and loading speed, the absolute values are not compared to the results reported in this study, described in Chapter 4. All the films exhibited an increase in hardness with increase in heat treatment temperature. It was also observed that films with greater amount of MTES exhibited lower hardness and a slower hardening process with an increase in heat treatment temperature. The hardness was correlated to the presence of hydroxyl (Si-OH) groups, i.e., the lesser the amount of OH groups present, the harder the film. An increase in the molar ratio of precursors having methyl groups (CH_3) was found not only to decrease the hardness of the films, but also to decrease the reduced elastic modulus [9, 27, 28]. An increase in organic components has been shown to have the same effect [28, 29].

Films produced with only the TEOS precursor had a measured reduced elastic modulus of 43 GPa and hardness measured using a Berkovich indenter of 2.3 GPa [10]. For comparison, it is reported that the Vickers hardness of silica glass is 635 kg/mm^2 (5.8 GPa) [30]. The Vickers and Berkovich indenters have the same area function ($A = f(h)$, where A is the cross sectional area of the indenter and h is the distance of such cross section from the tip of the indenter), thus the two can be compared.

The hardness of sol-gel derived films, produced with an MTES precursor, were studied as a function of heat treatment temperature [16]. One interesting result is the relative increase in hardness, which doubled as the heat treatment temperature increases from 300 to 800 °C. This increase was attributed to the formation of Si-O-Si bonds that result from polymerization of Si-OH bonds and/or burning of CH_3 groups.

2.2.4 Photoluminescence Spectroscopy

Sol-gel-derived silicate networks have been found to be spectroscopically active and their luminescence emission strongly effected by chemical and physical variables. Chemical variables include the concentration of the interacting species, their ratios, reaction medium (solvent), pH, catalyst, temperature during condensation [31] and presence of organic molecules [32, 33]. Physical variables can

include pore size and density [34], aging time [35], surface morphology and roughness [36], nanocrystalline silicon concentration [37], heat treatment temperature [38] and environment [39], and laser excitation power, energy and time of exposure [34, 37, 40, 41].

Luminescence in sol-gel films has been attributed to a delocalized electron-hole recombination process. Han et al. [31] stated that the origin of the luminescence from all types of hybrid sol-gel derived silica is similar, irregardless of how the sol-gel solutions are prepared. Even though the luminescence in sol-gel derived silica gels is not yet well understood, Han et al. [31] have proposed three possible mechanisms: a defect mechanism [34, 42–44], a charge transfer mechanism [40], and a carbon impurity mechanism [35, 41, 45, 46].

The predominant defects in silicate networks, that can be pointed to as a source of luminescence emission, are the oxygen deficiency centers. In the bulk of silica clusters these appear in the form of a neutral oxygen vacancy ≡Si-Si≡ (2.7 eV) [47], a nonbridging oxygen hole center •O-Si≡O_3 (≈ 2.7 eV) [43] and/or twofold coordinated silicon lone pair centers O-Si-O (3.0 eV) [48]. On the surface of the silica clusters, the oxygen deficiency centers appear as OH related surface centers (3.7 eV) [44] and H related surface centers (2.35 eV) [49–51]. Zyubin et al. [51] reported that in order to excite the green photoluminescence emission from H related surface centers in silicon-based nanoscale materials, approximately 3.5 eV energy is required, which corresponds to the direct band gap transition in Si [51]. On the other hand, H related surface centers on silica-based nanoscale materials need a much higher excitation energy, on the order of 4.7-6.4 eV.

A charge transfer mechanism was postulated by Garcia et al. [40], where the charge transfer occurred between the silicon and oxygen atoms in the Si-O bonding. This was supported by the fact that an intense UV excitation was needed to produce a broad emission peak (2.88 eV). Moreover, calculations found that each Si atom had a net charge of +1.649 e and each ligand O atom had a -0.597 e charge. Garcia et al. also recognized that the organic components might play a role in the luminescence process: "the blue emission appears to be related not only to a charge transfer process but also to the presence of organic radicals, which make this process more likely in a way not yet understood [40]."

Carbon impurities, in the carbonyl form, embedded into a silicate network have been believed to be the cause of blue light emission [35, 45, 46]. Defects of these kinds have shown an emission maximum between 450 and 600 nm (2.07-2.76 eV). Green et al. [45] suggested that during heat treatment, some carbon present in the unhydrolyzed precursor's organic ligands can decompose to create a C substitutional defect for Si. This fourfold C defect can absorb the photon's energy, which breaks two single-bonded oxygen atoms, resulting in the formation of a double bond with one of the

oxygen atoms and a Si^+ and an O^- at the terminations. By the inverse process, light is emitted. Bekiari et al. [41] also attributed the luminescence of silica sol-gel films to carbon impurities. In this case, the individualized emitting centers (C=O groups, 3.15 eV) were localized on the surface of silica clusters. The luminescence emission was seen to be influenced by the size of the silica clusters. In particular, larger clusters are reported to emit at longer wavelengths than smaller clusters.

The luminescence properties of sol-gel films have been studied under a wide range of temperatures. Carbonaro et al. [38] published an article showing the photoluminescence variation on porous silica at low temperature (300 to 8 K). Garica et al. [40] focused on high temperature photoluminescence (from 200°C to 800 °C) . In particular, the blue emission was seen to increase up to 400 °C, after this temperature the emission began to decrease and disappeared completely at 800 °C. This bleaching effect was also reported by Canham et al. [35]. In the study by Garcia et al. [40], it is mentioned that above 500 °C a pyrolytic effect took place in the sample; a color change to a brown tone was observed.

PVP (polyvinylpyrrolidone) was found by Fujihara et al. [22] to exhibit a bluish emission centered at 440 nm. This blue emission band is attributed to radiative relaxation of electrons from LUMO (lowest unoccupied molecular orbital) to HOMO (highest occupied molecular orbital) levels in PVP.

2.2.5 Raman Spectroscopy

Raman spectroscopy is a useful tool to investigate the chemical and structural nature of hybrid sol-gel materials [52]. In particular, this technique has been employed to study the evolution of the siloxane (Si-O-Si) [53], silanol (Si-OH) [53–55] and methylsilane ($Si\text{-}CH_3$) [56] groups in silica based sol-gel derived thin films. The modification in intensity and peak position of siloxane bands was found to correlate with the density of hybrid sol-gel films [53].

Carbon clusters with sizes in the 0.2 to 2 μm range where characterized by confocal Raman spectroscopy [57]. The results showed a clear difference between the particles having a diamond structure (1332 cm^{-1}) compared to those particles having a graphite structure (1382 cm^{-1} and 1580 cm^{-1}). Thus, Raman spectroscopy can be used to verify the hypothesis of carbon cluster formation in ion irradiated hybrid MTES/TEOS films. Moreover, this technique can be used to investigate the structure type (graphite versus diamond-like carbon) of these clusters.

2.2.6 Ion Irradiation

Ion beams have become an integral part of numerous surface processing schemes and surface modification techniques of solids.

Pivin's research group [58–60] has analyzed the effects of ion-irradiation on Si-based polymers as an alternative route to heat treating green ceramics. The transformation of Si-based gels to ceramics using ion-irradation offers several advantages over heat treatment, such as the selective release of hydrogen which allows more compact and harder films while also retaining adherence to the substrate without showing signs of cracking. Concerning the release of hydrogen, the heat treatment process has been reported to affect the entire organic molecule CH_3 (i.e., MTES) with consequent loss of C atoms, which in irradiated films can precipitate out in the form of either graphite or diamond-like clusters. Pivin has worked with several different materials such as MTES (methyltriethoxysilane) [60–64], PTES (phenyltriethoxysilane) [62,64], TH (triethoxisilane) [60,64], PCS (polycarbosilane) [61,65], and TEOS (tetraethoxysilane) [60,62]. The irradiations were carried out with a variety of ions including He, Au, Ag, C, Si, Cu, and Xe at different energies (200 keV - 3 MeV) and fluences (1 x 10^{11} - 5 x 10^{16} ions/cm^2). Pivin et al. [60–62] observed an increase in hardness and photoluminescence intensity with increasing irradiation fluence. These increases were suggested to be linked to hydrogen radiolysis, which allows the carbon atoms to cluster creating a diamond-like carbon compounds and would explain an increase in hardness. Transmission electron microscopy examination was used to provide direct evidence of carbon cluster formation [60], and Raman spectroscopy experiments showed peaks of diamond as opposed to graphite [60,61].

In other studies, the hardening of polymeric materials having a sp^2 carbon structure (graphite) has been linked not to the transformation of the structure toward a rigid sp^3 carbon structure (diamond-like) but to the formation of a rigid three-dimensional sp^2 carbon bonded network [66]. In the case of ion irradiated PMMA [67], the surface hardening was attributed to the transformation of polymeric materials into hydrogenated amorphous carbon under electron irradiation.

Venkatesan et al. [58] also reported the formation of a diamond-like clusters after ion irradiation, but contrary to Pivin's work, it was stated that the diamond-like carbon clusters did not play much of a role in the mechanical strengthening. Venkatesan et al. found a cross-linking mechanism to be the cause of the hardness increase. Rangel et al. [68] came to the same conclusion, stating that the increase in hardness of ion irradiated plasma polymer films has been associated with the depletion of H and increase in cross-linking with fluence. In particular, the hardness increased an order of magnitude (up to 4.2 GPa) after He implantation with a fluence of 10^{21} ions/m^2. Also, in the same

study [68], a shrinkage of the optical gap and diminution in the electrical resistivity with the increase in fluence was measured.

Concerning the cause of the observed increase in hardness, electronic stopping has been indicated as the primary cause for sol-gel derived Si-based films conversion, and the role of nuclear stopping was found to be minimal [69,70]. Kucheyev et al. [71] observed in a study of ion irradiated polyimide that for a given value of electronic energy loss, irradiation with different ion species results in different values of mechanical properties (including hardness, elastic modulus and tensile strength). The efficiency for increasing the material's hardness was shown to have an exponential dependence on electronic stopping power.

The variation in hardness and reduced elastic modulus with the indentation depth is shown in the work of Brun et al. [72], and the phenomena was attributed to the gradual loss of the ion's energy as the ions penetrate the target.

Kumar et al. [63] found experimentally that ion irradiated silica based sol-gel derived films showed an increase in photoluminescence response. The maximum photoluminescence emission intensity occurred when the product of electron stopping power and fluence (ϕ) was between 4.9 and 8.4 eV/atom. This increase in photoluminescence intensity, along with a red shift, was associated with an increase in carbon cluster size.

Chapter 3

Experimental

3.1 Sol-gel Thin Film Synthesis and Modification

MTES [$CH_3Si(OC_2H_5)_3$] and TEOS [$Si(OC_2H_5)_4$] based films were prepared by the sol-gel technique at the Stiftung Institut für Werkstofftechnik (IWT) in Bremen, Germany. The starting solution was composed of 5 mol of ethanol, 1 mol of water, 1 mol of acetic acid, and 0.4 mol of TEOS. Under vigorous stirring, 0.6 mol of MTES was then added to the starting solution drop by drop. The resulting solution was stirred for 10 minutes before adding 0.25 mol of PVP (polyvinylpyrrolidone) [$(C_6H_9NO)_n$] [23, 26]. Finally, the solution was stirred for 30 minutes at 50 °C. The molecular structures of the MTES, TEOS, and PVP are shown in Appendix A

Spin coating was used to deposit the solution on 50 mm diameter polished silicon wafers. Dip coating was also used in some preliminary work which has been reported elsewhere [73]. After the films were allowed to dry in air for 3-5 minutes, they were heat treated in a pre-heated furnace at temperatures ranging from 300 to 800 °C, and held at constant temperature over time periods ranging from 10 to 60 minutes. Ion irradiation was carried out on films heat treated at 300 °C for 10 minutes and also on films heat treated at 800 °C for 10 minutes. Film thickness measurements were obtained through ball cratering (European Standard ENV 1071-2) [74] and by atomic force microscopy (AFM) using a step-height technique. An estimate of the film density was made using the measured film thickness, the areal dimensions of the film, and the measured weight gain after coating.

Thickness Measurement

The thickness values obtained by ball cratering (European Standard ENV 1072-2) have been shown to agree with the thickness measurements obtained by observations using Scanning Electron Microscopy (SEM) on cleaved films for film thicknesses greater than 1 μm by our collaborators at the IWT. On the contrary, ball cratering was found to be inadequate for the measurement of films with thicknesses less than 1 μm.

In order to improve the ability to measure the thickness of the sol-gel films a step-height measurement was performed. The step on the green ceramic state film was created by scratching the film with a razor blade. The step created was analyzed using Raman Spectroscopy in order to verify that the scratch completely eliminated the sol-gel film from the silicon wafer (Figure 3.1). It was observed that the silicon wafer was not scratched by the blade since the surface of the silicon wafer at the bottom of the step had an rms roughness of 1.5 nm over a scan size of 1 μm^2, which was comparable to the surface roughness of the uncoated wafer. Nanoindentation experiments were also performed at the bottom of the scratch confirming that it was in fact the silicon substrate having a reduced elastic modulus of 160 GPa and hardness of 11 GPa.

At first, the use of a White Light Interferometer (WLI) was considered for the step-height measurement. This method was discarded since this technique requires knowledge of the refractive index of the hybrid sol-gel film in order to accurately determine the film thickness. Unfortunately this is an unknown and can also vary throughout the thickness of the film, and as well with different processing techniques (heat treatment temperature and holding time, ion irradiation species, energy, fluence, etc.). To overcome this problem, an AFM in tapping mode was employed. The concern with this technique was the limited scan size of this instrument, which is on the order of 70 μm, and thus may be not large enough to include the step generated by the razor blade. It was found that the step created with the razor blade presented a relatively sharp edge, with a lateral dimension on the order of 10 μm and thus created no problems for the AFM step-height measurements. In Figure 3.2 the scratch obtained using a razor blade observed with an optical microscope at a magnification of 40x can be seen. Also, in the same figure, the average step-height and the single section step-height measurement are shown. Recall that each scan is composed by 256 lines, the average step-height is the average of all the 256 section measurements taken in a scan.

The film thicknesses measured by the step-height are reported in Table 3.1, where the maximum and minimum values are the maximum and minimum of five to nine measurements recorded on the full wafer. Every wafer was cleaved into smaller specimens with dimensions of approximately 8 mm

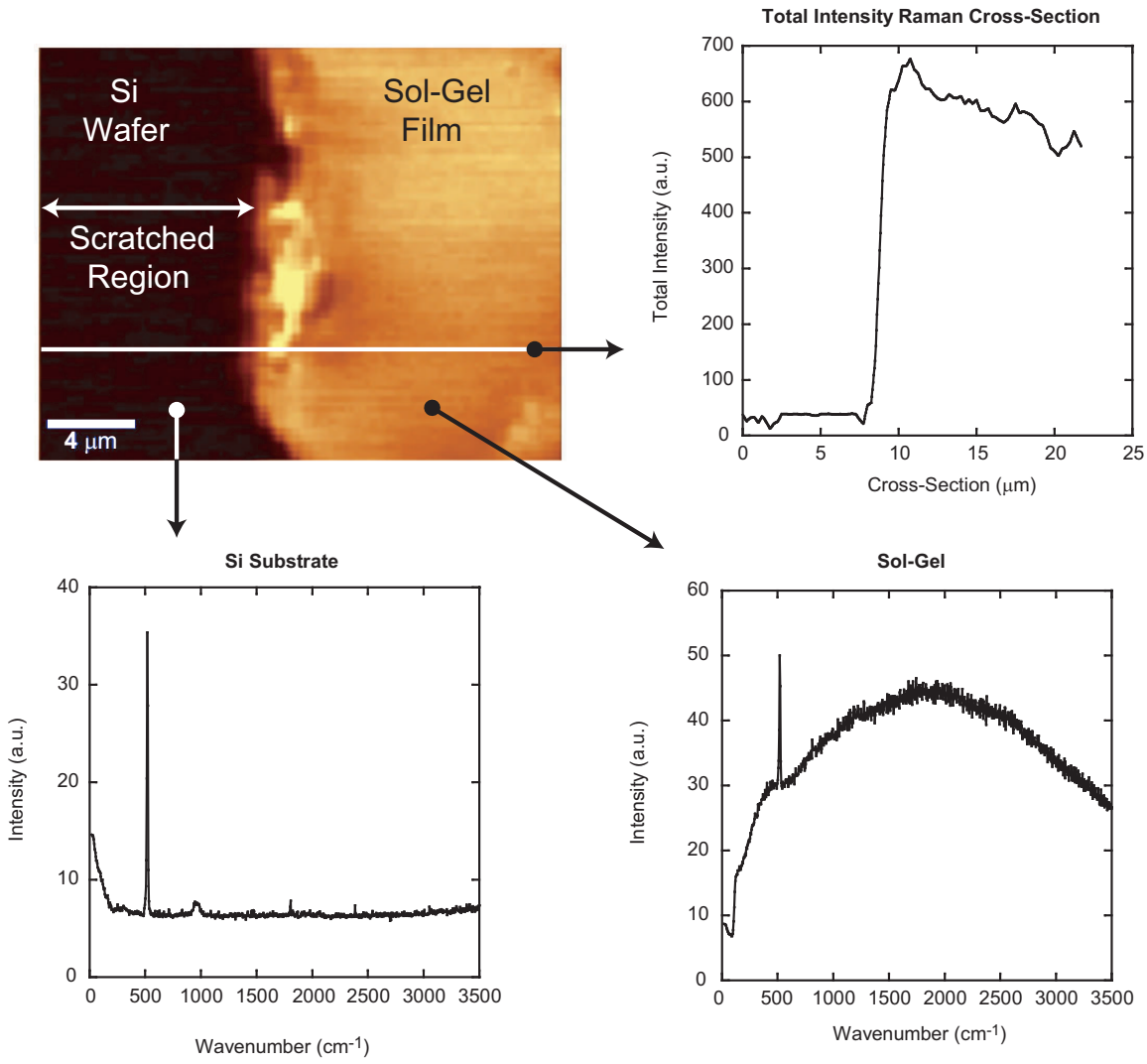

Figure 3.1: Confocal Raman spectra (532 nm excitation) showing that at the bottom of the scratch only the Si-Si (Si wafer) Raman signal is present

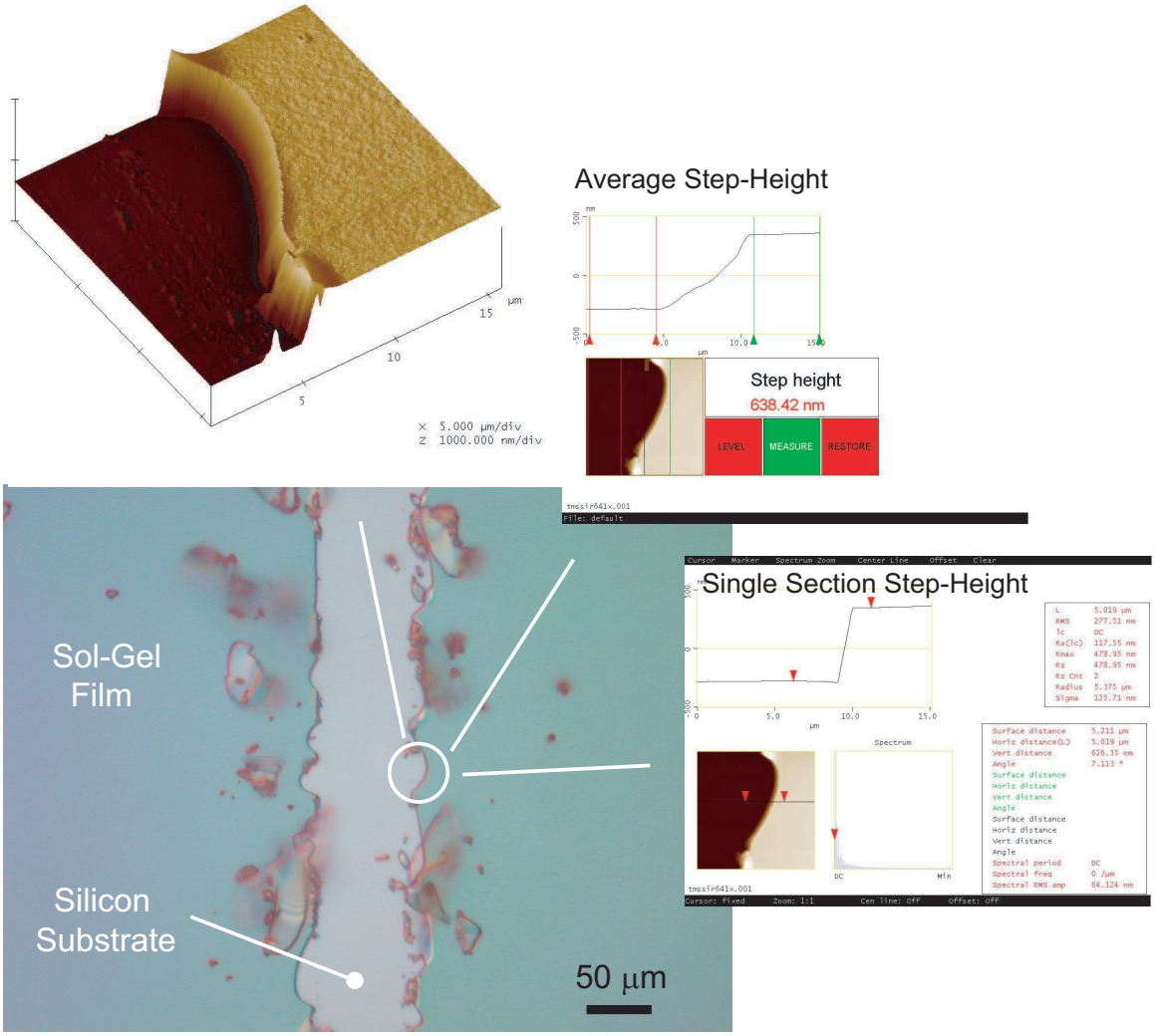

Figure 3.2: Step height measurement performed by AFM.

by 8 mm. The thickness of every specimen was measured and the variation in thickness in a single

Substrate	**Sample**	**Thickness**			**Heat**	**Holding**
		Mean	Max	Min	**Treatment**	**Time**
		nm	nm	nm	°C	min
Silicon Wafer	MSSiR 62	**600**	630	560	300	10
Silicon Wafer	MSSiR 63	**620**	640	590	300	10
Silicon Wafer	MSSiR 64	**655**	720	580	300	10
Silicon Wafer	MSSiR 108	**830**	920	700	600	10
Silicon Wafer	MSSiR 112	**670**	710	640	800	10

Table 3.1: Sol-gel film thicknesses measured by AFM step-height.

specimen was found to be less than ± 20 nm. These specimens were subsequently ion irradiated with different ion species and fluences, and the variation in film thickness was evaluated by measuring the step-height after irradiation took place.

Concerning the spatial variation, the WLI measurements showed the following two features:

1. A background waviness with a peak to valley of approximately 30 nm and a cycle of 400 μm (the sinusoidal waves did not possess a particular orientation)

2. Surface defects - hillocks with height reaching up to 800 nm. From the WLI images it was estimated that those hillocks covered anywhere from 0 to approximately 15 % of the scanned area (1.3 mm x 1 mm) - the values reported here are just an estimation. The hillocks were proven by AFM to be artifacts of the interferometry related to the variation of refractive index of the film and not topographical defects. In the possibility that the variation in refractive index could affect the value obtained by nanoindentation, it was decided to perform nanoindentations at 200 μm apart so that the value of reduced elastic modulus and hardness will not be taken all on a region having the same refractive index. Since the error bars, representing the maximum and minimum value obtain in five experiments, in all the results reported in Chapter 4 are very small, the effect of refractive index variation on the mechanical properties is consider negligible.

3.1.1 Ion Irradiation

As an alternative to high temperature heat treatment, ion irradiation was used to convert the deposited gel into a ceramic coating.

Ion irradiation consists of bombarding a target with ions that have been accelerated through a potential of 10 - 100 kV. The fundamental parts of an irradiation system are an ion source, an acceleration column, a mass-separator, and a target chamber.

The interaction of the ion with the target matter causes a loss of energy leading to a lower ion velocity. The loss of energy per distance traveled can be divided in two physical events: the inelastic collisions of the ions with the electromagnetic cloud, i.e., the electrons of the target, also known as the electronic stopping power $\left(\frac{dE}{dx}\big|_e\right)$; and elastic collisions of the ion with the nucleus of the target atoms, also known as the nuclear stopping power $\left(\frac{dE}{dx}\big|_n\right)$.

The total energy loss per distance traveled can be expressed as:

$$\frac{dE}{dx} = \left.\frac{dE}{dx}\right|_e + \left.\frac{dE}{dx}\right|_n \tag{3.1}$$

where the subscripts e and n refer to electronic and nuclear stopping. The electronic collisions involve a small energy loss for each collision and both the deflection of the ion trajectory and lattice distortion can be considered negligible. The nuclear collisions typically result in larger energy losses than that of the electronic collisions and involve ion trajectory changes and the introduction of lattice disorder. The relative importance of these two losses varies with the energy and mass of the incoming ion along with the atomic number of the target.

The variation in electronic and nuclear stopping power as a function of the penetration depth into the target material is plotted in Figure 3.3 for the case of Si^+ ions, with an incident energy of 100 keV, encountering a 300 °C TEOS/MTES sol-gel derived film with a density of 1.1 g/cm^3.

The penetration depth, also called the projected range of the ions, PR, is determined by the rate of energy loss along the trajectory of the ion (assumed perpendicular to the target surface):

$$PR = \int_{E_0}^{0} \frac{1}{dE/dx} dE \tag{3.2}$$

where E_0 is the energy of the incident ions (100 keV for the case shown in Figure 3.3). The projected ion range distribution for an amorphous material can be assumed to be Gaussian and thus described by a projected range (mean value) and a straggling (distribution FWHM).

The computer program entitled the Stopping and Range of Ions in Matter (SRIM) developed by Ziegler [75] was used in order to calculate the value of projected range, surface electronic and

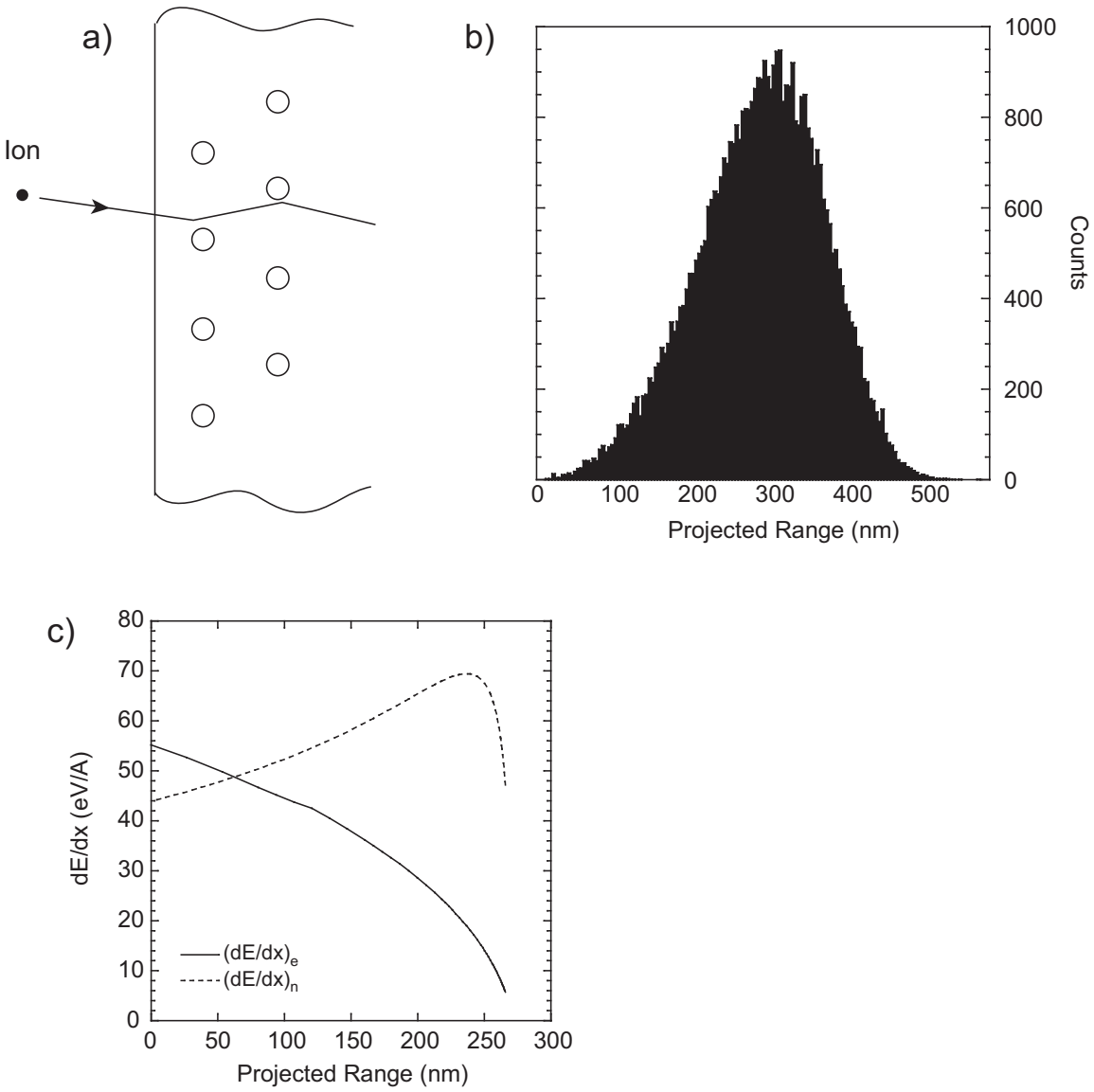

Figure 3.3: a) Sketch of the nuclear collision between the incident ion and the nucleus of the target; b) Projected ion range Gaussian distribution; c) Variation in electronic and nuclear stopping power as a function of the penetration depth into the target material. Plot b) and c) are for the case of Si^+ ions with an incident energy of 100 keV encountering a 300 °C TEOS/MTES sol-gel derived film with a density of 1.1 g/cm^3.

nuclear stopping power, as well as electronic and nuclear stopping power as a function of projected range.

Experimental

Ion irradiation was performed on, 300 °C heat treated sample, using several ions such as H^+, He^+, O^+, N^+, N^{2+}, Si^+, and Cu^{2+}, with energies ranging between 30 keV and 2 MeV and fluences ranging between 1 x 10^{14} ions/cm^2 and 1 x 10^{17} ions/cm^2. The projected ion range, the surface electronic and nuclear stopping powers, and the electronic and nuclear energy deposited at the surface were calculated using the Stopping and Range of Ions in Matter (SRIM) computer program developed by Ziegler [75]. The ion beam had an angle of 5 degrees with respect to the normal direction of the target surface.

Ion irradiation was conducted using a 3.2 MV Tandem ion accelerator (MeV beam energy) and an ion implanter (keV beam energy) at the Los Alamos National Laboratory.

3.2 Nanoindentation

A method of measuring the surface mechanical properties of materials on submicron length scales has been made possible by the development of instruments that continuously measure force and displacement [76–78]. The mechanical properties can be obtained from the loading [79] or unloading [78,80,81] portion of the force-displacement curve irrespective of the small size of the indentation imprint. In the present work, the Oliver and Pharr method [80] was used for the analysis of the force-displacement data. The steps employed are described below.

The elastic modulus (E) is the most commonly measured mechanical property along with the hardness (H). To do so, the unloading data is analyzed according to a model relating the contact area at the peak load to the elastic modulus by considering the deformation of an elastic half space by an elastic punch. The contact area is then estimated from the indenter shape function. Once the contact area is known, it is possible to obtain a separate measurement for E and H.

The elastic contact problem, of fundamental importance in the analysis procedure, was originally considered in the late 19th century by Boussinesq [82] and Hertz [83]. Boussinesq developed a method based on potential theory for computing the stresses and displacements in an elastic body loaded by a rigid, axisymmetric indenter. The method was used to derive the solutions of several indenter geometries such as cylindrical and conical indenters [84]. Hertz analyzed the problem of elastic contact between two spherical surfaces with different radii and elastic constants. The work of Hertz

was used as a model to remove the assumption of a rigid indenter. Another major contribution was made by Sneddon [85], who derived general relationships between the load, displacement, and contact area for any punch that can be described as a solid of revolution of a smooth function . His results show that the load-displacement relationship for a simple punch geometry can be written as:

$$P = \alpha h^m \tag{3.3}$$

where P is the load applied to the indenter, h is the elastic displacement of the indenter, and α and m are constants where m depends on the geometry of the indenter.

To consider the plastic effect on the above elastic problem involves dealing with nonlinear constitutive equations and a number of material parameters describing the material behavior. An early experiment of Tabor [86], concerning the shape of the indentation imprint after the elastic recovery of the material, sheds considerable light on the effects of plasticity in indentation. Tabor's experiments showed that, at least in metals, the imprint left by a spherical indenter is still spherical with a slightly larger radius than the indenter, and the imprint left by a conical indenter is still conical with a larger included tip angle. The significance of these experiments is that since the elastic contact solution exists for several geometries, the ways in which plasticity affects the indentation of elastic unloading data can be dealt with by taking into consideration the shape of the perturbed surface in the elastic analysis. Tabor used this result to relate the elastic modulus to the size of the impression left after indentation. This intuition was further resolved in the early 1970's, by the work of Bulychev, Alekhin, and Shorshorov who put forth the following equation:

$$S = \frac{dP}{dh} = \frac{2}{\sqrt{\pi}} E_r \sqrt{A} \tag{3.4}$$

where $S = dP/dh$ is the experimentally measured stiffness obtained from the unloading data, E_r (or E^*) is the reduced elastic modulus, and A is the projected area of the elastic contact. The reduced elastic modulus is another result of Tabor's experiments, and was defined to account for the non-rigidity of the indenter. It is defined as:

$$\frac{1}{E_r} = \frac{\left(1-\nu^2\right)}{E} + \frac{\left(1-\nu_i^2\right)}{E_i} \tag{3.5}$$

where E and ν are the elastic modulus and Poisson's ratio for the specimen and E_i and ν_i are the same parameters for the indenter. Equation (3.4) which relates the reduced elastic modulus to the measured stiffness and to the projected area was developed for a conical indenter. It has been shown, however, to apply not only for conical indenters but also for pyramidal indenters as well [87].

To obtain E_r from Eqn. (3.4), the contact area A must also be determined. The projected area can be measured optically but, for small dimensions, this is a time consuming and difficult task.

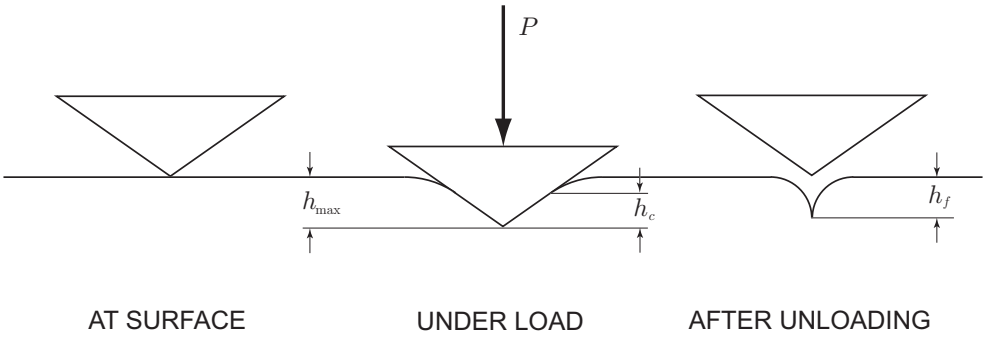

Figure 3.4: Schematic representation of the indenting process showing h_c, contact depth, $h_{\max}$, maximum depth, and h_f, final depth

To avoid measurement of the imprint, Oliver et al. [88] suggested a simple method to evaluate the projected area based on the load-displacement data and a knowledge of the indenter area function (or shape function), i.e., the cross-sectional area of the indenter as a function of the distance from its tip. This method is based on the assumption that at the peak load the material deforms conformally to the shape of the indenter, as shown in Fig. 3.4 where the behavior of the indenter-surface during indentation is shown. From Fig. 3.4 three depths can be distinguished: $h_{\max}$, the maximum depth which the indenter reaches at maximum load evaluated from the undeformed surface; h_f , the final depth left once the load is completely removed; and h_c , the contact depth evaluated at the peak load considering the deformation undergone by the surface (curvature of the surface resulting from the elastic response). The maximum and final depths can be easily determined from a typical load-displacement curve obtained by indentation as shown in Fig. 3.5, and then the maximum depth can be used to determine the projected contact area [88]. An improvement of this method was made by considering the contact depth to evaluate the projected area (from now on referred to as the contact area) which is between the maximum and final depth (Fig. 3.5). An empirical method was proposed by Doerner and Nix [78] to evaluate the contact depth based on extrapolating the initial linear portion of the unloading curve to zero load. This empirical method was subsequently modified [80] by considering the initial stage of unloading to be not linear, but to follow a power law of Sneddon type, Eqn. (3.3). This results in a increment of the contact depth towards the maximum depth and the magnitude is a function of ε, the geometry of the indenter (for example $\varepsilon = 1$ for a flat punch and 0.72 for a conical indenter). Once the contact depth is known, the contact area could be determined by the indenter area function. Then, the elastic modulus and the hardness can be

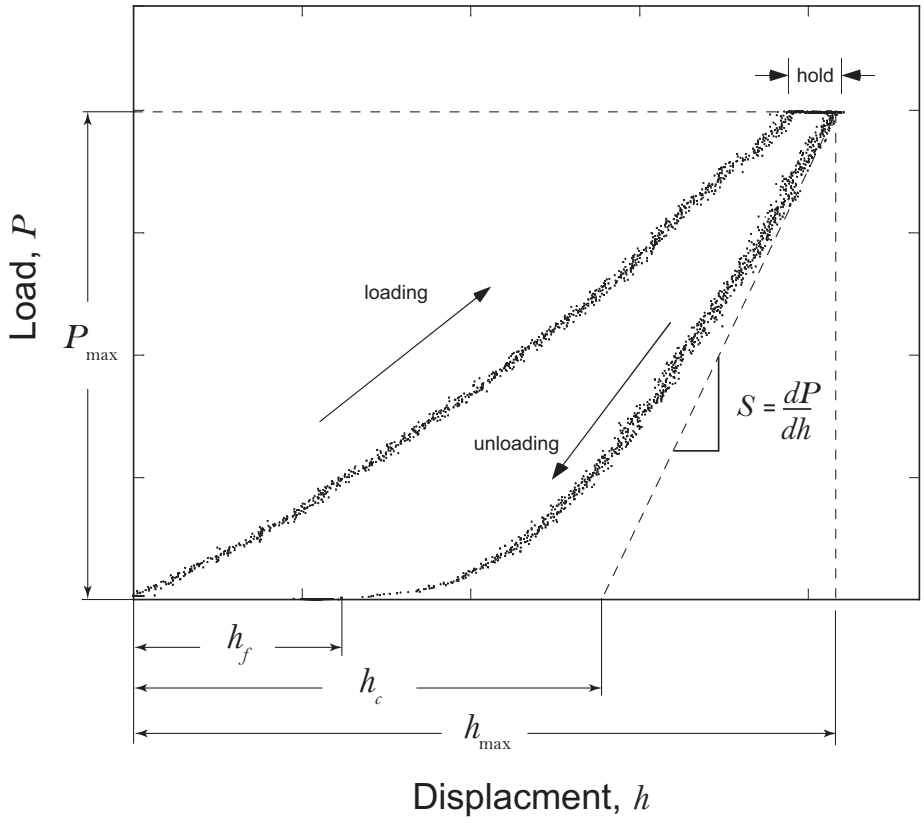

Figure 3.5: Typical load-displacement curve showing: $P_{\max}$, the maximum load, $h_{\max}$, the maximum depth, h_f, the final depth, h_c, the contact depth which is a function of the indenter geometric constant ε, and S the measured stiffness.

evaluated separately, the elastic modulus with Eqn. (3.4), and the hardness from the definition:

$$H = \frac{P_{\max}}{A} \tag{3.6}$$

The uncertainties resulting from the use of the method described above have been reported elsewhere [89].

Experimental

In this study, nanoindentation experiments were performed using a load-controlled commercial nanoindenter. The instrument enables indentation to be performed with maximum loads < 25 μN, and $h_{max} < 5$ nm. A Berkovich indenter was used for all the experiments. The geometry of this diamond indenter is a three-sided pyramid with an ideal area function the same as that of a Vickers indenter. The compliance and area function for the Berkovich indenter were obtained following the calibration procedure proposed by Oliver and Pharr [80]. Before each set of experiments,

the instrument and the sample were allowed to thermally equilibrate for 10-12 hours in a thermal enclosure.

Single loading indentations were performed to investigate the reduced elastic modulus and hardness of the films. A loading rate of 50 μN/sec was used, with a holding time of either 10 seconds or twice the loading time (depending on which one was greater) at peak load to allow for time dependent effect to diminish. Maximum applied loads ranged from 15 to 10000 μN which corresponded to maximum depths of 17 to 245 nm. Indentations were performed to a maximum depth of approximately 8 percent of the film thickness, if not otherwise stated, to assure that there was no influence of the substrate on the measured mechanical properties of the film. The rms roughness of all samples was characterized by atomic force microscopy, and found to be less than 3 nm over a 1 μm^2 scan area. All nanoindentations were performed in darkness and at room temperature. All reported data represent the average of five indentations.

3.3 Optical Spectroscopy Techniques

3.3.1 Photoluminescence Spectroscopy

Photoluminescence spectroscopy is a technique that analyzes the re-emission of light resulting from the photo excitation of a material. In particular, a photoluminescence active material is a material that, once optically excited, absorbs the excitation photons creating electron-hole pairs which, after recombining, result in the re-emission of less energetic photons characteristic of the material under study. The description of the instrument used has been described in great detail in previous work by a former colleague, D. Hamby [90].

In this study photoluminescence emission was excited using the 351 nm (3.532 eV) line from an Ar^+ laser with 10 mW power. The experiments were conducted at room temperature and at 4 K. The emitted light collected was dispersed by a 0.5 m monochromator with a 1200 grooves/mm grating, and detected with a liquid N_2 cooled CCD (123 K). The spectral resolution of the system used was 0.55 nm at 630 nm (1.7 meV at 1.97 eV). During the photoluminescence experiments, the laser beam was focused to a 0.4 mm^2 area on the surface of the film. The increase in temperature due to the laser excitation was calculated to be 4 °C, considering a continuous circular heat source on the surface of a semi-infinite medium [82]:

$$T = \frac{2q_0 R}{\pi K} \tag{3.7}$$

where q_0 is the heat supply rate (25 mW/mm^2), R is the radius of the circular source (0.357 mm),

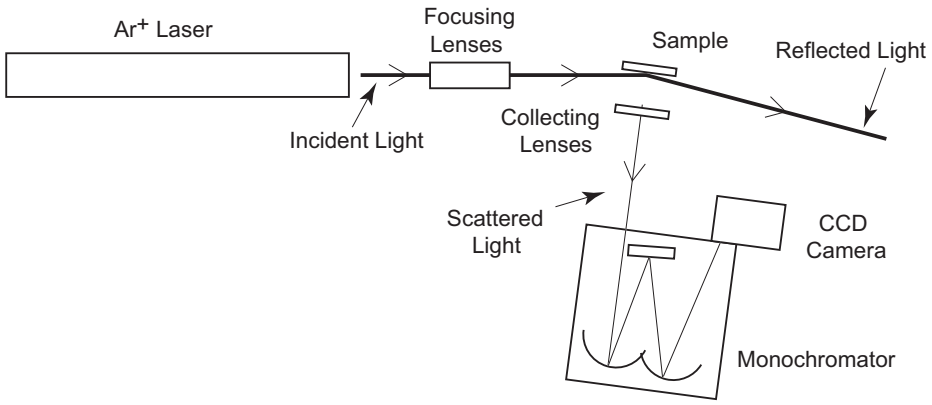

Figure 3.6: Photoluminescence setup.

and K is the conductivity of silica (1.4 x 10^{-3} W/(mm °C) [91]) assume to be the same as the conductivity of the sol-gel film. For all experiments, the shutter of the monochromator was set at a 100 μm aperture, and the integration time at 1 sec.. The acquisition of a spectrum took approximately 3 min.. A schematic of the system setup can be seen in Figure 3.6.

3.3.2 Confocal Raman Spectroscopy

Raman spectroscopy refers to the study of vibrational and rotational modes of matter by analysis of the inelastic scattered light resulting from exposing the matter to laser light (monochromatic and polarized light).

When laser light interacts with matter some of the light will be reflected and some will be transmitted, as shown in Figure 3.7. Of the transmitted light, some will be absorbed and some will be scattered. Raman spectroscopy is used to analyze the portion of light that is scattered, while photoluminescence spectroscopy deals with photon emission resulting from the absorbed light.

The general Raman effect will be discussed first before focusing on confocal Raman spectroscopy which has been utilized in this study. In confocal Raman spectroscopy the laser light is focused by a microscope objective to its diffraction limit, thus to a spot size on the order of half the wavelength of the laser used (hundreds of nanometers spot size). An advantage of confocal Raman is that scattered light from a small region close to the focal point is collected, allowing for a Raman depth profile of the specimen under study.

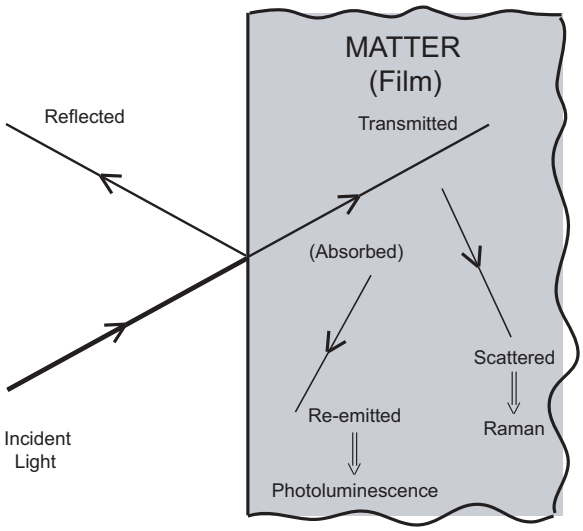

Figure 3.7: Processes involved in the interaction of laser light with matter.

Theory - Raman Effect

The Raman effect is a result of the inelastic scattering process involving the interaction of an electromagnetic wave with the vibrational and rotational modes of the system studied. The scattering process of light involves at least two quanta of light interacting at the same time on the light-matter system. The scattered light can be divided into two scattering regimes, elastic (Rayleigh) and inelastic (Raman effect). The elastic scattering, also called Rayleigh scattering, is the most intense process and is characterized by having the scattered quantum energy identical to the incident quantum energy. The efficiency of the elastic scattering is on the order of 10^{-3} with respect to incident intensity. In the case of inelastic scattering, the incident and scattered quanta energies are different producing a net change in energy. If the scattered photon is less energetic than the incident one, the scattered light is observed at a lower frequency than that of the excitation photon. This is called Stokes Raman scattering. On the contrary, if the scattered photon is more energetic than the incident one, the scattered light is observed at a higher frequency than that of the excitation photon. This is called anti-Stokes Raman scattering. The efficiency of the Raman effect is less than 10^{-6} with respect to incident intensity. The scattering process described above is illustrated in Figure 3.8.

The Stokes shift has a higher intensity with respect to the anti-Stokes shift due to the fact that the population of the less energetic ground states are higher than the more energetic ground states, thus the probability of having a Stokes shift is higher. From a quantum mechanical approach the electron population is higher in lower states obeying Maxwell-Boltzmann statistics [92]:

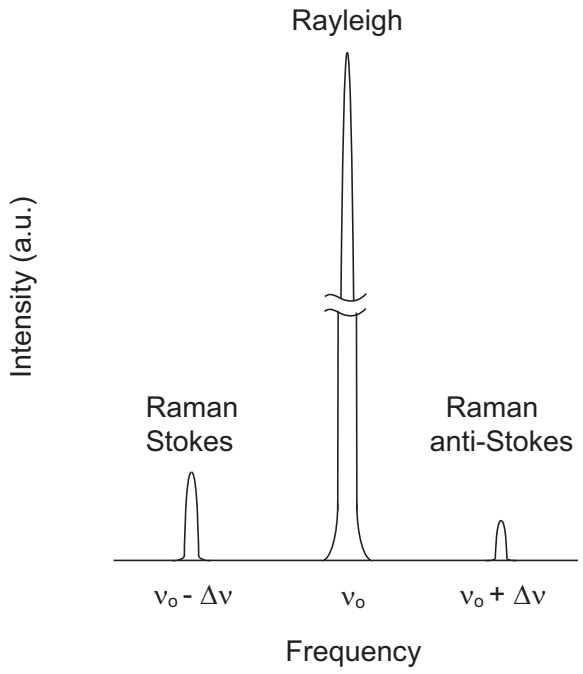

Figure 3.8: Raman effect and Rayleigh scattering spectrum for an excitation of frequency ν_o.

$$\frac{I_a}{I_s} = \left[\frac{(\nu_0 + \Delta\nu)}{(\nu_0 - \Delta\nu)}\right]^4 exp\left(-\frac{h\Delta\nu}{kT}\right) \tag{3.8}$$

where I_a is the intensity of the anti-Stokes Raman, I_s is the intensity of the Stokes Raman, ν_0 is the excitation frequency, h is Planck's constant (6.626 x 10^{-34} J·s), k is the Boltzmann constant (1.38 x 10^{-23} J·K^{-1}), and T is the absolute temperature. In the case of diamond-like carbon Raman shifts ($\Delta\nu$ = 4 x 10^{13} Hz) excited at room temperature (T = 293 K) with a Nd:YAG at 532 nm wavelength (ν_0 = 5.64 x 10^{14} Hz) the ratio I_a/I_s is equal to 1.4 x 10^{-3}.

Raman spectra are commonly represented as intensity versus relative wavenumber and not frequency, as shown in Figure 3.8. The wavenumber ($\bar{\nu}$) unit is cm^{-1} and it is obtained from the frequency (ν) using the following equation:

$$\bar{\nu} = \frac{\nu}{c} = \frac{1}{\lambda} \tag{3.9}$$

where c is the speed of light and λ the quantum wavelength. "Relative" wavenumber refers to the difference between the absolute wavenumber of the incident and scattered quanta.

The scattering process, annihilation and creation of photons at the same time, can also be described using the electron energy states by the introduction of "virtual" states is shown in Figure 3.9. The virtual states are imaginary states of the molecule under analysis to which an electron is excited

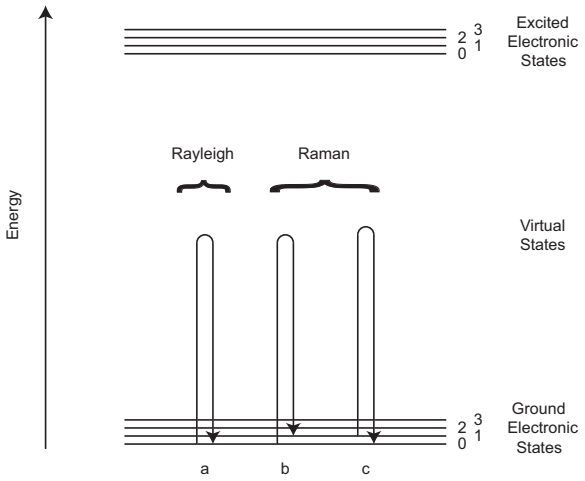

Figure 3.9: Raman effect and Rayleigh scattering mechanism. a) Rayleigh, b) Stokes, c) anti-Stokes

to by the incident photon. The excited electron cannot station on the virtual state but immediately falls to a ground electronic state and thus a photon is generated. As mentioned previously, if the incident photon has the same energy of the created one the process is a Rayleigh process, while if the two photons are of different energies the process is known as the Raman effect.

Instrument

The main components of a Raman set-up are an excitation source, a diffraction grating (used to disperse the scattered light) and a detection system (used to quantify the intensity of the dispersed photon energies).

The excitation source must be monochromatic light, thus a laser is ideal. The wavelength of the laser used does not influence the Raman spectra of the matter under study, but it does play a role in the Raman efficiency. Specifically, a higher energy laser has a higher efficiency than a lower energy laser. Luminescence activity of the specimen under study is a very important aspect to consider in the choice of the laser energy used in Raman experiments. Luminescence emission is a process with an efficiency on the order of 10^3 greater than the Raman effect. In the case of a luminescence active material, the laser wavelength has to be chosen carefully in order to limit the luminescence activity. In particular, high wavelength quanta have less probability to be absorbed by the matter, thus less probability of luminescence activity (Figure 3.9).

The laser source used in this study was a 532 nm frequency doubled Nd:YAG laser with a power of 70 mW. The laser light is directed to the microscope objective using a 100 μm diameter optical fiber. The maximum laser power at the sample that can be obtained was measured to be 5 mW.

The spot size at the focal plane has been estimated to be 380 nm using a 100x objective lens with a numerical aperture of 0.90 using the following equation:

$$D \cong \frac{2\,\lambda}{n\,\pi\,NA} \tag{3.10}$$

where D is the spot size at the focal plane, λ is the wavelength of the laser source, n the refraction index of the immersion medium (air), and NA is the numerical aperture of the microscope objective.

The commercial monochromator used in this study has a focal length of 300 mm and an aperture ratio of 1/3.9 with respect to the focal length. The monochromator used contained three gratings, all blazed at 500 nm, 150, 600, and 1800 grooves per mm, mounted on a rotating turret (providing the possibility to select the grating without opening the monochromator). The aspheric mirrors possessed an 88 - 90 % reflectance at 200 nm.

The detector used is a charged-coupled device (CCD) thermoelectrically cooled to 200 K with a quantum efficiency peak of 94 % at 750 nm and a quantum efficiency of 65 % at 500 nm. The detector resolution at 500 nm, based on the technical specifications provided by the monochromator manufacturer, are 0.033 nm (1800 grooves/mm), 0.126 nm (600 grooves/mm), and 0.530 nm (150 grooves/mm) for the different gratings. The detector resolution (also called Band-Pass, BP) can also be calculated using the following approximate equation:

$$BP \cong \frac{slit\ width * groove\ width}{monochromator\ focal\ length} \tag{3.11}$$

where the *slit width* is the larger between the entrance and exit monochromator slit. The entrance slit is the diameter of the optical fiber used (three choices available for this study: 25, 50, and 100 μm) and the exit slit is the width of a CCD pixel, 26.6 μm. The *groove width* depends on the grating used, and can be either 1/150 mm, 1/600 mm, or 1/1800 mm. The $focal\ length$ of the monochromator used is 300 mm. Thus, BP is equal to 0.049 nm for a 25 μm fiber and a 1/1800 mm *groove width*, and equal to 2.22 nm for a 100 μm fiber and a 1/150 mm *groove width*.

The detector resolution is the minimal discrete energy quanta (wavelength) that can be resolved by the detection system. This quantity depends mainly on the number of grooves per mm of the grating used and the distance between the grating, and the detector (monochromator focal length); as can be seen in equation 3.11.

One should notice that an increase in detector resolution, or the ability to resolve narrower peaks and peak center positions with greater accuracy, results in a decrease in collection efficiency of the monochromator. The collection efficiency is directly proportional to the optical fiber diameter used

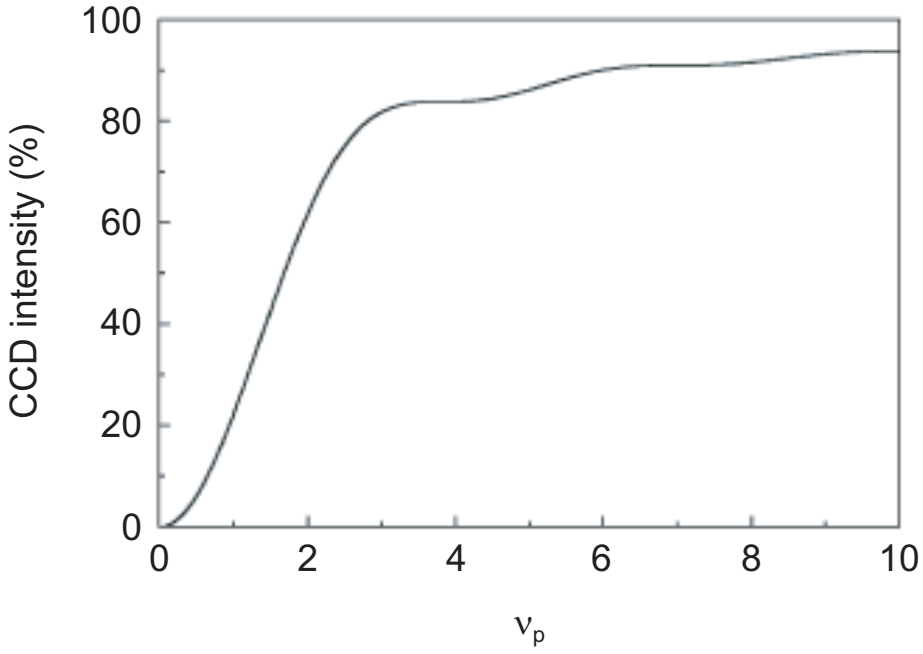

Figure 3.10: Collection efficiency as a function of the pinhole size (optical fiber diameter) in optical coordinates ν_p, figure taken from the WiTec Raman microscope manual

to connect the collection objective to the monochromator, i.e., a smaller fiber results in less efficient collection as can be observed in Figure 3.10. In this figure, the CCD collection efficiency as a function of the pinhole size in optical coordinates is reported. The pinhole size in optical coordinates can be calculated with the following equation:

$$\nu_p = \frac{\pi}{\lambda} d_0 \frac{NA}{O_m} \tag{3.12}$$

where ν_p is the pinhole size in optical coordinates, λ is the laser wavelength (532.2 nm), d_0 is the optical fiber diameter, NA is the objective numerical aperture, and O_m is the objective magnification.

Experimental

Confocal Raman spectroscopy was performed using a commercial Raman microscope manufactured by WiTec. The excitation source used was a 532 nm wavelength Nd:YAG laser with a power at the surface of approximately 3-5 mW. The laser light was focused on the surface of the specimen using a 100x microscope objective with a 0.9 numerical aperture. A portion of the scattered light was collected from the same objective (reflection mode) and dispersed using a 300 mm focal length monochromator and a grating of choice between 150, 600, and 1800 grooves/mm. The dispersed

light was detected with a thermoelectrically cooled CCD camera (200 K).

3.4 Supporting Techniques

3.4.1 Elastic Recoil Detection

Elastic Recoil Detection (ERD) was performed using 3 MeV $^4He^+$ ions to measure the changes in H concentration due to the ion irradiation. A 14 μm thick Mylar film was placed in front of the detector to block the forward-scattered $^4He^+$ ions.

ERD experiments were conducted using a 3.2 MV Tandem ion accelerator (MeV beam energies) in the Ion Beam Materials Laboratory (IBML) at Los Alamos National Laboratory.

3.4.2 X-ray Photoelectron Spectroscopy

X-ray Photoelectron Spectroscopy (XPS) experiments were conducted at the IWT in Bremen, Germany, using a commercial VG Escalab 200i-XL instrument. XPS was used to provide further information on changes in the chemical composition of the films caused by heat treatment and ion irradiation. In particular, the C, O, and Si atomic percentage contents of the films were evaluated. Possible impurities on the surface of the hybrid silica films were removed by sputtering prior to the XPS experiments. The sputtering was performed using a 3 mW Ar^+ ion beam, which removed the top 3 to 10 nm of the surface in a 3 x 4 mm^2 area. XPS was performed using a Mg-Kα X-ray source at 1253.6 eV and 300 W power.

The XPS data was analyzed using software written by Kwok [93]. The data were translated so that the C1s peak was centered at 285.0 eV for all the spectra obtained [94].

Chapter 4

Results and Discussion

This chapter is centered on the effects of ion irradiation on the surface mechanical behavior of hybrid organic/inorganic modified silicate thin films. All films analyzed were synthesized by sol-gel processing from tetraethoxysilane (TEOS) and methyltriethoxysilane (MTES) precursors and spin-coated onto (100) Si substrates.

This chapter is divided into five sections, the first of which compares the two modification techniques used to convert the sol-gel films from a polymeric material to a ceramic type material: heat treatment versus ion irradiation [95]. The other four sections focus on the ion irradiation process, and in particular they are centered on: 1) the characterization of the surface mechanical properties as a function of the ion projected range and fluence; 2) the effect of electronic and nuclear stopping power, as well as the effect of the surface deposited electronic energy on the mechanical properties; 3) the investigation of the causes and the structural changes undergone by the hardened films; 4) the design of a model describing the ion irradiation hardening, based on a rain-drop type model.

A comparison of the surface mechanical properties, chemical composition, and photoluminescence response was made of films which were heat treated at temperatures ranging from 300 °C to 800 °C and films which were first heat treated at 300 °C and subsequently ion irradiated. The films ion irradiated presented higher values of hardness and reduced elastic modulus (Equation 3.5) with respect to the heat treated films. In particular, both reduced elastic modulus and hardness are seen to increase monotonically with the increase in ion irradiation fluence, with a maximum hardness of 7.7 GPa (19 fold increase with respect to the unirradiated film hardness of 0.4 GPa) and reduced elastic modulus of 84.0 GPa (12 fold increase with respect to the unirradiated film reduced elastic modulus of 7.1 GPa).

The effect of the electronic versus nuclear stopping power and thus inelastic versus elastic ion collisions has been investigated. The electronic stopping has been found to be principally responsible for the film hardening, while the role of nuclear stopping is minimal. Moreover, a linear dependence of hardness with electric stopping power at constant electronic energy deposited to the surface was observed.

The causes of the ion irradiation hardening effect have been investigated. The increase in mechanical properties of hybrid sol-gel films following ion irradiation is thought to be linked to structural changes. Ion irradiation results in a cross-linked silica film as well as the segregation of carbon clusters, both of which contributed to increase the mechanical properties of the films. But neither could explain in full the observed 19 fold increase in hardness.

A model describing the hardening effect of ion irradiated films is presented. Knowing that the hardening process is dependent upon the ion irradiated species, this model characterizes the hardening effectiveness of the ion considering two parameters: the constant hardening cross-section and the hardening coefficient. The constant hardening cross-section represents the cross-sectional area hardened by the interaction of an ion with the target material, and the hardening coefficient represents an index of the cross-sectional area gradient as a function of fluence. The hardening cross-section is considered to vary with fluence, since the hardness of the target material was observed to change with fluence.

4.1 Heat Treatment vs. Ion Irradiation

Hybrid organic/inorganic modified silicate thin films were synthesized by sol-gel processing from tetraethoxysilane (TEOS) and methyltriethoxysilane (MTES) precursors and spin-coated onto (100) Si substrates. A comparison was made between films which were heat treated at temperatures ranging from 300 °C to 800 °C and a film which was first heat treated at 300 °C and subsequently irradiated using 2 MeV He^+ ions with a fluence of 3 x 10^{15} ions/cm^2. Nanoindentation was used to measure the hardness and reduced elastic modulus, both of which exhibited an order of magnitude increase after irradiation. The increase in hardness and reduced elastic modulus of the irradiated film was accompanied by a 50 percent reduction in H concentration. X-ray photoelectron spectroscopy (XPS) was employed to examine the changes in C, O and Si composition resulting from heat treatment and ion irradiation. Photoluminescence spectroscopy was used to examine the sol-gel photon emission with a laser excitation of 351 nm (3.53 eV). Increasing the heat treatment temperature and holding time led to a decrease in emission intensity; the same behavior was observed for the ion

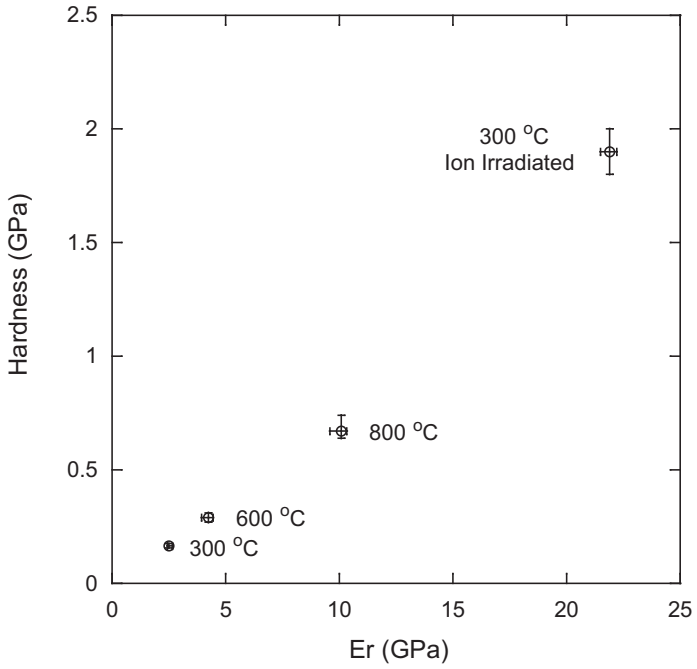

Figure 4.1: Hardness and reduced elastic modulus obtained by nanoindentation for the heat treated and ion irradiated films. All reported data represent the average of five indentations, and the error bars represent the maximum and minimum values obtained.

irradiated film.

4.1.1 Surface Mechanical Properties

The effect of heat treatment temperature on the hardness and reduced elastic modulus (E_r) of the films is shown in Figure 4.1. Both hardness and E_r are seen to increase with increasing heat treatment temperature from 300 °C to 800 °C. Also shown in Figure 4.1 are the results for the film which was heat treated at 300 °C and then subjected to ion irradiation. Both hardness and E_r were observed to increase an order of magnitude over the unirradiated film from 0.16 to 1.93 GPa and 2.5 to 21.9 GPa respectively. In addition, the values for hardness and E_r for the irradiated film were found to be substantially higher than for the film heat treated at the highest temperature studied (800 °C). All reported data represent the average of five indentations, and the error bars represent the maximum and minimum values obtained.

The observed increase in hardness and E_r of the irradiated film is linked to a decrease in H concentration in the film. Elastic Recoil Detection (ERD) showed a loss in H concentration of 50 percent after ion irradiation. This decrease in H concentration is consistent with previously

reported results for several other ion irradiated hybrid sol-gel and inorganic polymer films [59, 60]. The presence of excess H in the film prior to irradiation is due to the organic components Si-CH_3 and PVP (both rich in C-H bonds). These organic components persist in films heat treated at 300 °C since they are thermally stable up to 400-450 °C [20,21,25]. Although studies of H loss occurring in ion irradiated organic polymers have been previously reported [59], the governing mechanism is still under debate [60].

In addition to the increase in both hardness and E_r, the irradiated film showed no signs of cracking or delamination. In contrast, films heat treated at 400 °C were found to exhibit numerous cracks on the surface, which led to the delamination of the film from the substrate. As a result, nanoindentation could not be performed on these films. For films heat treated at the higher temperatures of 600 °C and 800 °C, there were no signs of delamination. The cause of the delamination observed for the film heat treated at 400 °C may be related to the film being held at a temperature close to the thermal stability limit of the organic components. Both heat treated and irradiated films were found to exhibit low roughnesses as measured with atomic force microscopy, with rms values ranging from 1.1 nm to 2.6 nm over a scan size of 1 μm x 1 μm for films heat treated at 300 °C and 800 °C respectively. The surface roughness was found not to change after ion irradiation. Both heat treatment and ion irradiation resulted in film shrinkage. Heat treatment at 800 °C resulted in an 80 percent decrease in film thickness, measured by ball cratering, from that measured for the 300 °C heat treated film. However, after ion irradiation only a 20 percent decrease was observed.

4.1.2 Chemical Composition

XPS was used to provide further information on changes in the chemical composition of the films caused by heat treatment and ion irradiation. The XPS spectra indicate that in addition to the H content discussed above, C, O, and Si are the principal elements present in both the heat treated and ion irradiated films. The results obtained for the atomic percentage of C and O, normalized by the atomic percentage of Si, are shown in Figure 4.2 [95]. For the heat treated films, the atomic ratio of O/Si is seen to increase from 1.4 to 1.8 for heat treatment temperatures from 300 °C to 800 °C, with this ratio increasing from 1.4 to 1.7 for the ion irradiated film. These changes are consistent with the evolution toward silica based films. Also as shown in Figure 4.2, the atomic ratio of C/Si is observed to decrease with increasing heat treatment temperature. Since both Si-CH_3 and PVP are thermally stable up to 400 - 450 °C [20, 21, 25], we expect that for hybrid MTES/TEOS films heat treated at 300 °C the C bonds present are C-H and C-Si, which are both present in the Si-CH_3

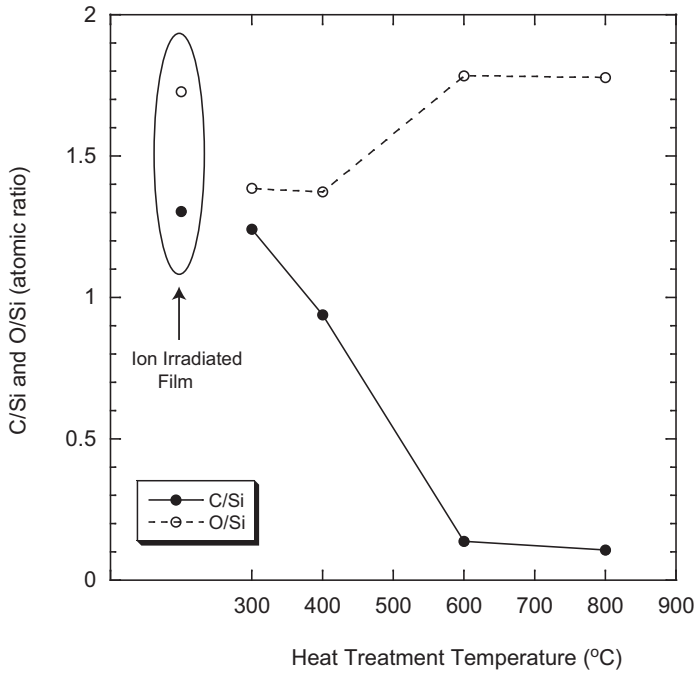

Figure 4.2: C/Si and O/Si atomic ratio obtained by XPS for the heat treated and ion irradiated films.

organic component introduced by MTES (CH_3-Si-$(OC_2H_5)_3$), and C-H and C-N, which are present in the polyvinylpyrrolidone (PVP) molecule. The atomic ratio of C/Si for films heat treated at 600 °C and higher, shows a significant reduction, which is consistent with the thermal decomposition of the Si-CH_3 and PVP organic components. For the ion irradiated film, the atomic ratio of C/Si shows little change from that prior to irradiation. This result suggests different decomposition kinetics of the organic components by ion irradiation when compared to the heat treatment process. That the C atoms are still present in the film after ion irradiation and that the film experiences a drastic loss of H suggest a selective release of H due to ion irradiation and the possibility of C precipitation in the form of clusters, as has been reported by Pivin et al. [62, 96].

4.1.3 Photoluminescence Activity

Changes in photoluminescence response of the hybrid sol-gel films with respect to the heat treatment temperature, holding time, and ion irradiation were investigated. The photoluminescence spectra as a function of heat treatment temperature are shown in Figure 4.3. The luminescence response is found to be more intense in the sample heat treated at 300 °C, where a broad peak (FWHM 100 nm) centered at 510 nm (2.43 eV) and two sharper peaks centered at 445 nm (2.79 eV) and

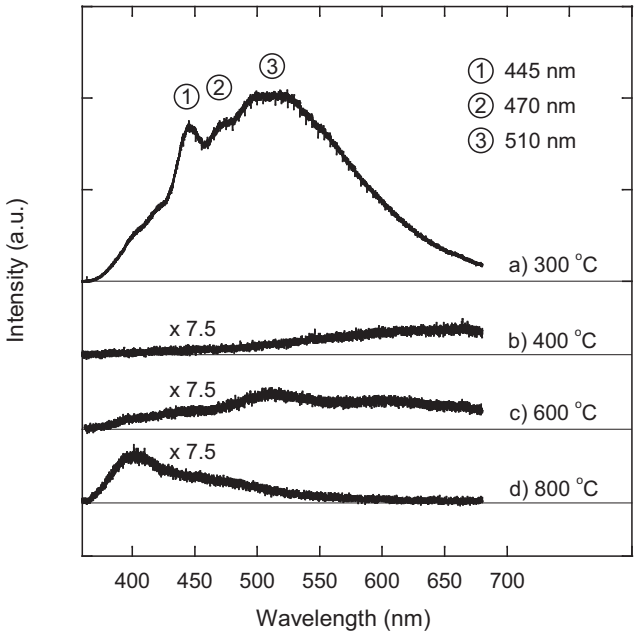

Figure 4.3: Photoluminescence spectra of sol-gel films heat treated at: a) 300 °C, b) 400 °C, c) 600 °C and d) 800 °C. Spectra b), c), and d) have been offset for clarity.

470 nm (2.64 eV) were observed. When the films were heat treated at a higher temperature, the luminescence intensity decreased by a factor of approximately 30.

A possible explanation, for the 445 nm emission peak observed for the films heat treated at 300 °C, is the presence of organic components, in particular PVP molecules. PVP molecules were found to exhibit a bluish emission centered at 430-440 nm by Fujihara et al. [22] and Manzoor et al. [97]. This blue emission band is attributed to the radiative relaxation of electrons from LUMO (lowest unoccupied molecular orbital) to HOMO (highest occupied molecular orbital) levels in PVP. The existence of defects like nonbridging oxygen hole centers (≡Si-O•) [43] (where ≡Si represents 3 Si-O bonds) or oxygen vacancy centers (≡Si•) [47], in the films can be related to the 470 nm peak observed. These defects were reported to present luminescence emission around 460 nm (2.7 eV). Hydrogen atoms can block some of these defects, forming hydrogen related species (≡Si-H and ≡Si-OH) [49] on the surface of silica clusters. Hydroxyl groups are also present as a result of incomplete hydrolysis during film synthesis. Hydrogen surface centers can be associated with the luminescence emission at 510 nm (2.43 eV). That the luminescence emission is completely quenched after a 50% H reduction, as in the case of the ion irradiated film, is consistent with this hypothesis.

All the emission peaks observed for the hybrid sol-gel films heat treated at 300 °C disappeared at higher heat treatment temperature. This is consistent with PVP being thermally stable up to

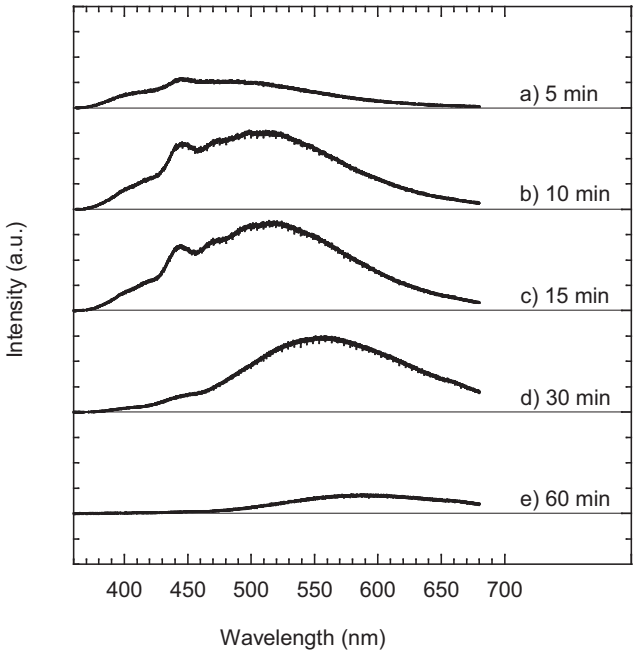

Figure 4.4: Photoluminescence spectra versus heat treatment holding time at 300 °C.

400 °C [23], and the silanol group (Si-OH) drastically decreases in quantity at 375 °C [22].

The changes in photoluminescence spectra as a function of the holding time at 300 °C were also measured. The holding time was varied from 5 to 60 minutes. With increasing holding time, more PVP molecules and OH groups are expected to accumulate enough energy to escape from the film. The decrease in PVP and OH content results in an increase in hardness and a decrease in luminescence intensity. The photoluminescence spectra are shown in Figure 4.4. The luminescence intensity of the peak centered at 445 nm wavelength, generated by PVP, increases going from 5 to 10 minutes holding time (unclear at this point what causes this increase), thence decreases (expected) for holding times greater than 10 minutes. This peak disappears after a 60 minute holding time at 300 °C, suggesting a burn out of the PVP molecules. The broad emission peak centered at 510 nm (associated with the OH group) for the film heat treated at 300 °C for 10 minutes is also observed to decrease in intensity as holding time increases. This peak presents an interesting and unexpected energy shift toward a higher wavelength with increasing holding time, moving from 490 nm to 590 nm wavelength. This red shift could be caused by the condensation constraint on the OH groups [98, 99].

The effect of ion irradiation on the hybrid sol-gel photoluminescence response was investigated for a film irradiated using 2 MeV He^+ ions with a fluence of 3 x 10^{15} ions/cm^2. The ion irradiated

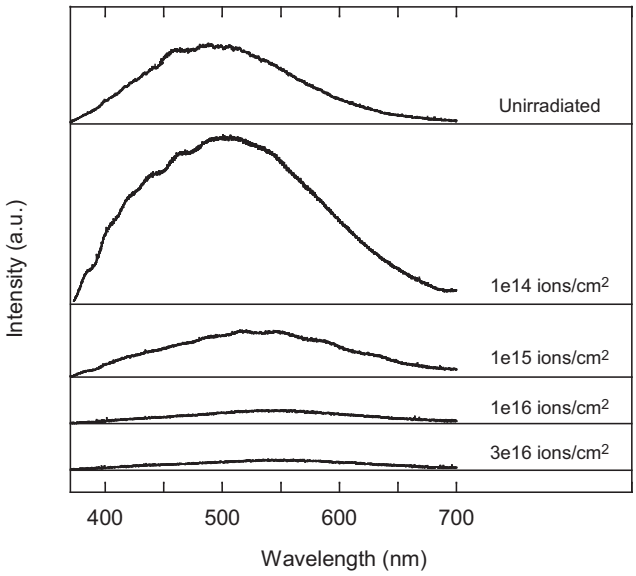

Figure 4.5: Photoluminescence spectra of sol-gel films unirradiated and ion irradiated with 100 keV Si^+ ions with fluence ranging from 1 x 10^{14} to 3 x 10^{16} ions/cm^2.

film did not exhibit any photoluminescence emission. This behavior is similar to the films heat treated at high temperatures, Figure 4.3.

Based on the results obtained for the heat treated films, the presence of silane groups and PVP molecules has been tied to low values of mechanical properties. Therefore, increasing the fluence, which was observed to decrease the H concentration, is expected to result in a decrease in OH concentration and thus an increase in hardness and a decrease in the luminescence intensity of the 445 and 510 nm peaks. The variation of the surface mechanical properties with respect to the ion irradiation fluence is described in Section 4.2. The variation on the photoluminescence response with ion irradiation fluence is reported here.

The relation between the oxygen defects (nonbridging oxygen and oxygen vacancy) and the emission centered at 470 nm has been examined by irradiating Si^+ and O^- into a film previously heat treated at 300 °C for 10 minutes. Theoretically it is thought that Si^+ ion irradiation might result in a decrease in the number of nonbridging oxygen defects (≡Si-O•) since Si and O ions easily react due to a negative recombination energy between them [100]. For the same reason, O^+ ion irradiation has the capability of decreasing an eventual presence of oxygen vacancy defects (≡Si•). Thus, Si and O implantation experiments have been designed to target the luminescence emission centered at 470 nm, with the possibility of discriminating between these two types of luminescence centers.

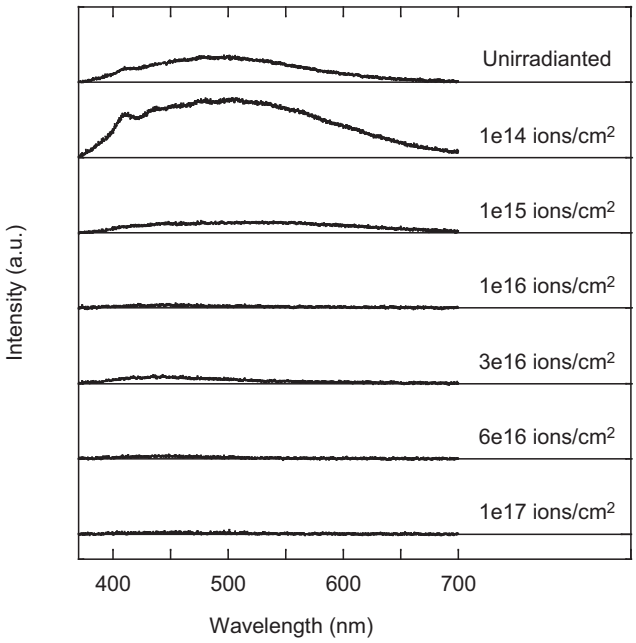

Figure 4.6: Photoluminescence spectra of sol-gel films unirradiated and ion irradiated with 100 keV O^+ ions with fluence ranging from 1 x 10^{14} to 1 x 10^{17} ions/cm^2.

The variation in photoluminescence response due to Si^+ and O^+ irradiations at different fluences are shown in Figures 4.5 and 4.6, respectively. Even though these experiments could not clarify the effect of nonbridging oxygen/oxygen vacancy defects, as theoretically explained above, they allowed the reporting of some observations on the effect of ion irradiation on the photoluminescence response of hybrid silica based sol-gel films. For both irradiation species, the specimens irradiated with a fluence of 1 x 10^{14} ions/cm^2 showed an increase in the luminescence emission intensity. For higher fluences, both irradiation species caused a decrease in the luminescence emission intensity. This observation is in agreement with a study conducted by Kumar et al. [63], in which a maximum in the luminescence intensity as a function of irradiation fluence was observed. Kumar et al. observed the maximum intensity to correspond to an electronic energy deposited at the surface between 4.9 and 8.4 eV/atom. For the ion irradiation performed in this study, the maximum is observed for a fluence of 1 x 10^{14} ions/cm^2 corresponding to at an electronic energy deposited of 4.8 and 4.2 eV/atom for Si^+ and O^+ ions respectively. For the fact that the lowest fluence performed was 1 x 10^{14} ions/cm^2 and that for a fluence of 1 x 10^{15} ions/cm^2 the electronic energy loss at the surface corresponds to 48 and 42 eV/atom respectively, the reported maximum has to be taken as a qualitative value since more data points between these two values are needed to determine more accurately the electronic energy deposited corresponding to the maximum emission intensity. The

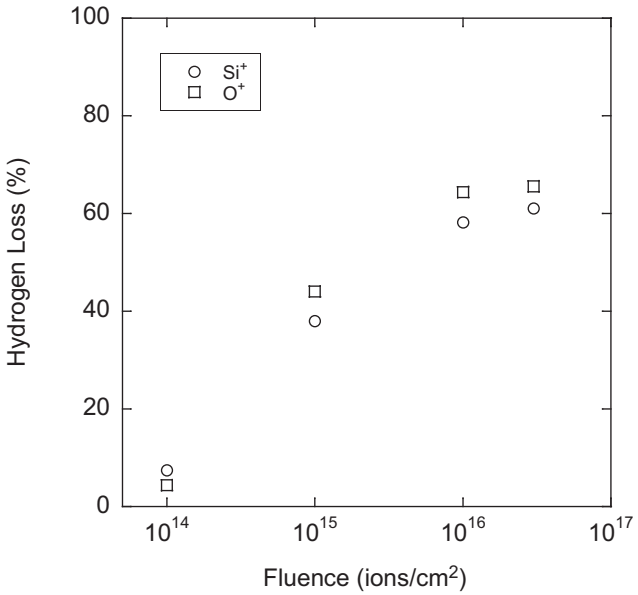

Figure 4.7: Hydrogen loss measured by ERD as a function of ion irradiation fluence for Si^+ and O^+ irradiations at 100 keV.

electronic energy deposited at the surface is defined as the product of the electronic stopping power (Table 4.1) and the fluence with respect to the density of the target (3.98 x 10^{22} atoms/cm^3).

ERD measurements showed a monotonic increase in hydrogen loss for both irradiation species (Figure 4.7). The decrease in H, and consequently of OH groups, can explain the quenching effect with increasing ion irradiation fluence. As a reminder, the concentration of OH groups has been linked to the intensity of broad emission centered at 510 nm. What remains to be understood is the presence of a maximum in the emission intensity, while the hydrogen loss increases monotonically. Kumar et al. [63] believe that the maximum in luminescence emission intensity is attributed to the formation of carbon clusters, although no evidence of this was found in this study.

4.2 Effects of Ion Irradiation on the Surface Mechanical Properties

The modification of hybrid TEOS/MTES sol-gel films by ion irradiation is shown to be more efficient than the heat treatment process in the conversion of the polymer sol into ceramic type coatings. Both reduced elastic modulus and hardness are seen to increase monotonically with the increase in ion irradiation fluence, with a maximum hardness of 7.7 GPa (19 fold increase with respect to the

unirradiated film hardness of 0.4 GPa) and reduced elastic modulus of 84.0 GPa (12 fold increase with respect to the unirradiated film reduced elastic modulus of 7.1 GPa)

All films characterized are hybrid modified silicate thin films, based on a combination of TEOS and MTES precursors, synthesized by sol-gel processing and applied to Si substrates by spin coating. The films thicknesses ranged from 600 nm to 3.0 μm. The film thickness was obtained by ball cratering (European Standard ENV 1072-2) for films thicker than 1 μm and by AFM step height measurement for films thinner than 1 μm. Using the measured film thickness, the dimensions of the film, and the measured weight gain after coating, the film density for unirradiated films was estimated to be 1.1 g/cm^3. Concerning the chemical composition, after the 300 °C heat treatment in addition to the H present, XPS identified the presence of carbon, oxygen, and silicon with relative atomic ratio C/Si equal to 2.29 and O/Si equal to 1.48 (48 at.% C, 31 at.% O, and 21 at.% Si). The concentration of C, O, and Si will be reposted as a ratio with respect to the at.% of Si since the concentration of H is not known. Recall that the XPS measurements do not allow for determining the atomic percent of H, which was estimated to be approximately 40 at.% by Rutherford Back Scattering measurements.

Before nanoindentation was performed, the surface roughness of all the films was characterized by atomic force microscopy and found to range from 1 to 3 nm rms over a scan size of 1 μm^2. Contrary to similar films which had been heat treated [95], the irradiated films showed no signs of cracking or delamination.

In all the experiments performed, the sol-gel films modified by ion irradiation exhibited the same trend for the hardness and reduced elastic modulus as can be observed in Figure 4.8. All reported data represent the average of five indentations, and the error bars represent the maximum and minimum values obtained. Both reduced elastic modulus and hardness increased at constant normalized contact depth (contact depth divided by film thickness, h_c/t) following irradiation.

Initially, this study investigated the effect of ion irradiation on the mechanical behavior of sol-gel film having a thickness of 3 μm (PR/t $<$ 1), Figure 4.9 a). Since these specimens exhibited both reduced elastic modulus and hardness values decreasing with increasing indentation penetration depth, it was postulated that this were affected by the presence of a soft sol-gel layer underneath the hard irradiated film. For this reason, thinner films were produced so that the ration PR/t was kept greater than 1 for all the ion species investigated producing fully irradiated coatings, Figure 4.9 b).

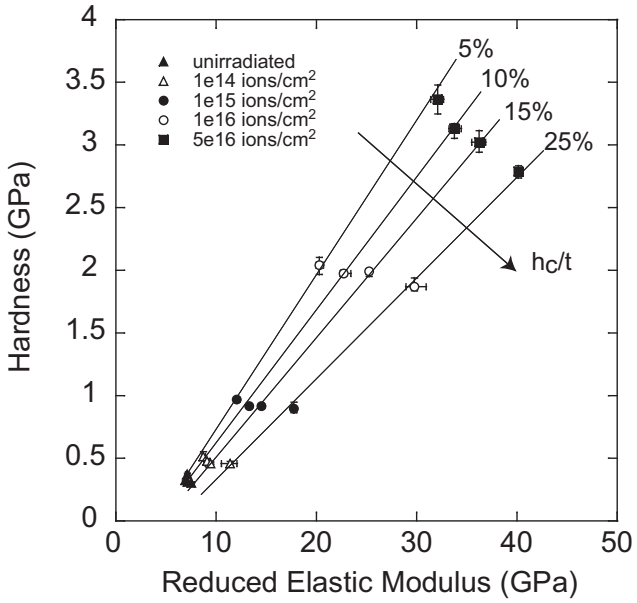

Figure 4.8: Hardness versus reduced elastic modulus for 125 keV H^+ irradiated sol-gel films with fluences ranging from 1 x 10^{14} and 5 x 10^{16} ions/cm^2. All reported data represent the average of five indentations, and the error bars represent the maximum and minimum values obtained.

4.2.1 Preliminary Ion Irradiation

Ion irradiation was carried out at room temperature using 100 keV Si^+, O^+ and N^+ ions with fluences ranging from 1 x 10^{14} to 3 x 10^{16} ions/cm^2 for Si^+ and 3 x 10^{16} ions/cm^2 for O^+ and N^+. The beam current was adjusted for all ions to be approximately 0.4 μA/cm^2.

The effect of ion irradiation on both the near-surface hardness and reduced elastic modulus was investigated [101]. Table 4.1 lists the incident ion energy and fluences used for the three ions considered. Also shown are the values for the film thickness prior to ion irradiation and values for the projected ion range and both the surface electronic and nuclear stopping powers at the surface calculated using SRIM (Stopping and Range of Ions in Matter) [75]. All three ions are seen to have approximately equal electronic stopping power at the surface, however for the case of Si^+ the nuclear stopping power is substantially greater than for O^+ and N^+ and is comparable to its electronic stopping power.

The effect of fluence on the hardness-depth profiles of the films irradiated with Si^+ is shown in Figure 4.10. Also shown is the hardness-depth profile of an unirradiated film. All reported data represent the average of five indentations, and the error bars represent the maximum and minimum values obtained. At depths above 50 nm, the error bars are barely visible. A monotonic increase in

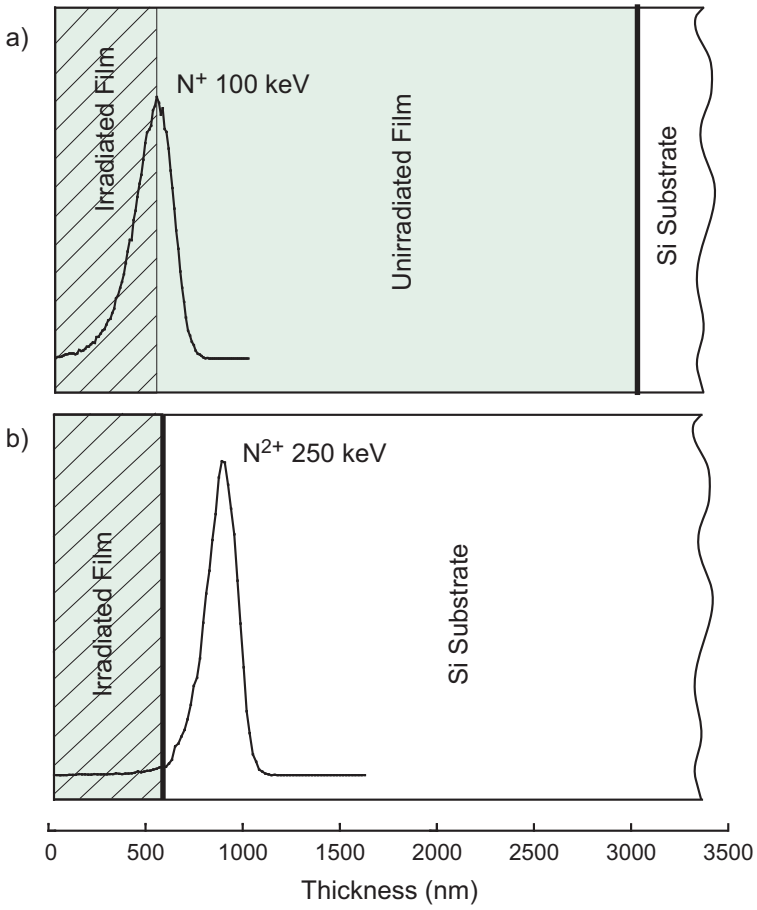

Figure 4.9: Sketch showing the ion distribution (projected range) calculated with SRIM for a) 3 μm thick film irradiated with 100 keV N^+ ion and b) 600 nm thick film irradiated with 250 keV N^{2+} ion.

Ion Irradiation	**Si^+**	**O^+**	**N^+**
Ion Beam Energy (keV)	100	100	100
Fluence (1e15 ions/cm^2)	0.1 - 30	30	30
Projected Range (nm)	260	446	469
Film Thickness (nm)	3000	3000	3000
$(dE/dx)_e$ (eV/Å)	19.3	16.7	17.8
$(dE/dx)_n$ (eV/Å)	15.3	4.6	3.3

Table 4.1: Ion irradiation data for a 3 μm thick film.

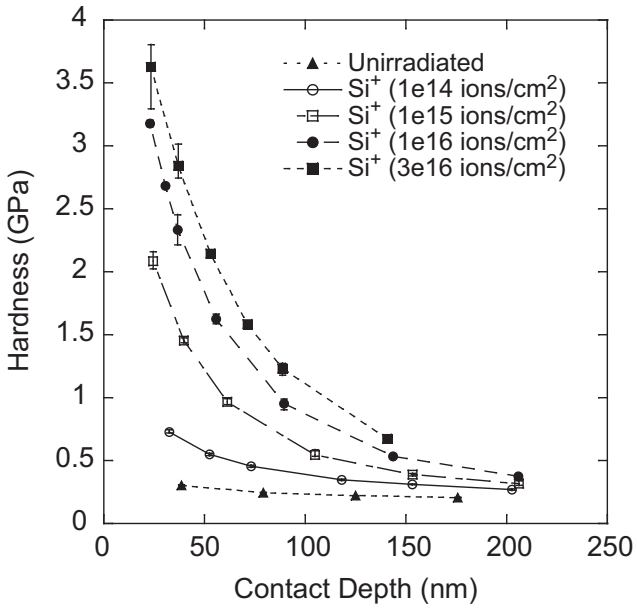

Figure 4.10: Hardness-depth profiles obtained by nanoindentation of the films irradiated with 100 keV Si^+ ions at fluences ranging from 1 x 10^{14} to 3 x 10^{16} ions/cm^2. All reported data represent the average of five indentations, and the error bars represent the maximum and minimum values obtained.

hardness at a given depth is observed with increasing fluence. At the near surface, the hardness of the film irradiated with the highest fluence increased an order of magnitude over that of the unirradiated film. The observation of increased hardness (and reduced elastic modulus) with increased ion fluence is consistent with other recent studies on the ion irradiation of polymers [102, 103]. The measured hardness profiles represent the convolution of several effects. The first is the indentation size effect, where a variety of materials have been shown to exhibit an increased hardness at the surface with respect to the bulk [104]. A slight increase in hardness at the surface is observed for the unirradiated film and it is possible that this indentation size effect increases as the film transforms towards a ceramic with increasing fluences. The second effect is the increased hardness due to the irradiation of the film and the possible depth effect resulting from changes in the energy deposited at a given depth (Figure 3.3). In the first 100 nm, the electronic stopping decreases by about 20 % and nuclear stopping increases by about the same amount. Lastly, at increasing depths the softer unirradiated layer below begins to affect the measured hardness. It is generally accepted [105] that this effect is not present for indentation depths less than 10 % of the layer thickness. Recall from Table 4.1 that the projected ion ranges were calculated to be 260 nm for Si^+ irradiation, 446 nm for O^+ irradiation, and 469 nm for N^+ irradiation. The reduced elastic modulus was also measured and was found to exhibit a similar depth dependence and a 3.5 fold increase (5.2 to 18.1 GPa) with increased fluence at a contact depth of 25 nm (Figure 4.11).

Figures 4.12 and 4.13 show the hardness and reduced elastic modulus depth profiles obtained for irradiations performed with Si^+, O^+ and N^+ with a fluence of 3 x 10^{16} ions/cm^2. Results for an unirradiated film are also shown. No observable differences in either hardness or reduced elastic modulus can be seen for the three different ions used. Recall that all three ions have about the same electronic stopping power, whereas Si^+ has a significantly higher value for nuclear stopping power which was also comparable to its value for electronic stopping. These results suggest that electronic stopping is principally responsible for the film conversion, and that the role of nuclear stopping is minimal. This observation is consistent with the results of Pivin et al. [70] in a 2005 study of sol-gel derived Si-based films.

The results of ERD indicated that the observed increase in hardness and reduced elastic modulus of the irradiated films is linked to a decrease in H concentration in the film, as shown in Figure 4.14. It was found that corresponding to the increase in hardness with increasing fluence, as shown in Figure 4.10, there was a monotonic increase in H loss at the surface from about 7 to 61 %. For the results shown in Figures 4.12 and 4.13, H loss at the surface was between 61-68 % for the three irradiations. This lower level of H concentration is consistent with previously reported results for

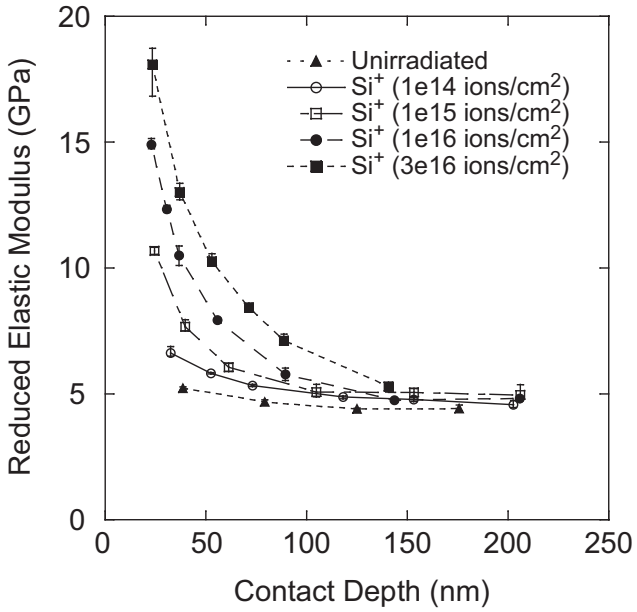

Figure 4.11: Reduced elastic modulus-depth profiles obtained by nanoindentation of the films irradiated with 100 keV Si^+ ions at fluences ranging from 1 x 10^{14} to 3 x 10^{16} ions/cm^2. All reported data represent the average of five indentations, and the error bars represent the maximum and minimum values obtained.

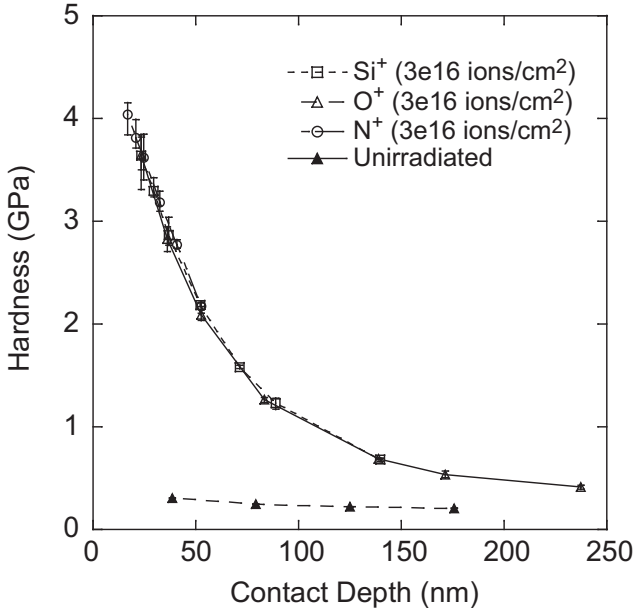

Figure 4.12: Hardness-depth profiles obtained by nanoindentation for films irradiated with 100 keV Si^+, O^+, and N^+ ions at a fluence of 3 x 10^{16} ions/cm^2. All reported data represent the average of five indentations, and the error bars represent the maximum and minimum values obtained.

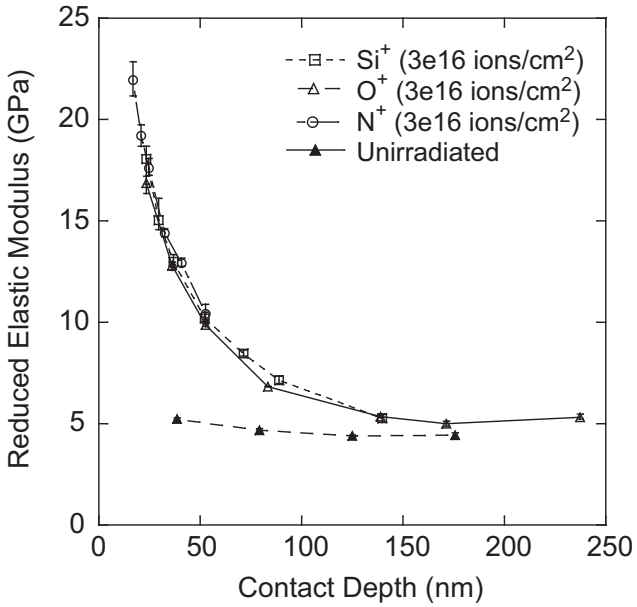

Figure 4.13: Reduced elastic modulus-depth profiles obtained by nanoindentation for films irradiated with 100 keV Si^+, O^+, and N^+ ions at a fluence of 3 x 10^{16} ions/cm^2.

several other ion irradiated hybrid sol-gel and inorganic polymer films [59, 60].

4.2.2 Fully Ion Irradiated Films

Ion irradiation was carried out at room temperature using 125 keV H^+ and 250 keV N^{2+} ions with fluences ranging from 1 x 10^{14} to 5 x 10^{16} ions/cm^2 for H^+ and 1 x 10^{15} to 5 x 10^{16} ions/cm^2 for N^{2+}. The beam current was adjusted for all ions to be approximately 30 μA/cm^2.

The effect of ion irradiation on both the near-surface hardness and reduced elastic modulus was investigated. These sets of experiments were designed in order to eliminate the effect of a soft layer (unirradiated sol-gel film) beneath a hard irradiated film, which was a concern in the results presented in the previous Section. Table 4.2 lists the incident ion energy and fluences used for the two ions considered. Also shown are the values for the film thickness prior to ion irradiation and values calculated using SRIM (Stopping and Range of Ions in Matter) [75] for the projected ion range, the surface electronic and nuclear stopping powers, and the electronic and nuclear energies deposited at the surface. Here, energy deposited is defined as the stopping power multiplied by the fluence.

The effect of fluence on the hardness-depth profiles of the films irradiated with H^+ is shown in Figure 4.15. The hardness is plotted as a function of the normalized contact depth, defined as the

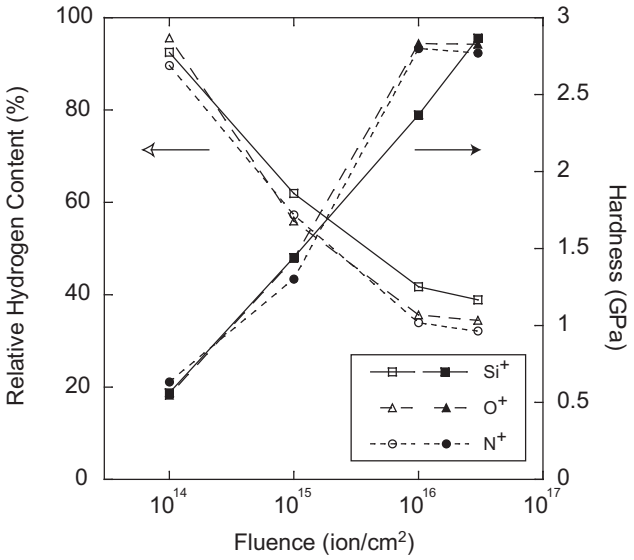

Figure 4.14: Hydrogen loss and hardness as a function of the ion fluence for Si^+, O^+, and N^+ irradiation.

Ion Irradiation	**H^+**	**N^{2+}**
Ion Beam Energy (keV)	125	250
Fluence (1e15 ions/cm^2)	0.1 - 50	1 - 50
Projected Range (nm)	2070	1060
Film Thickness (nm)	600 ± 30	620 ± 30
$(dE/dx)_e$ (eV/Å)	6.4	24.9
$(dE/dx)_n$ (eV/Å)	0.009	1.86

Table 4.2: Ion Irradiation data for 300 °C sol-gel film having a thickness ranging from 600 to 660 nm.

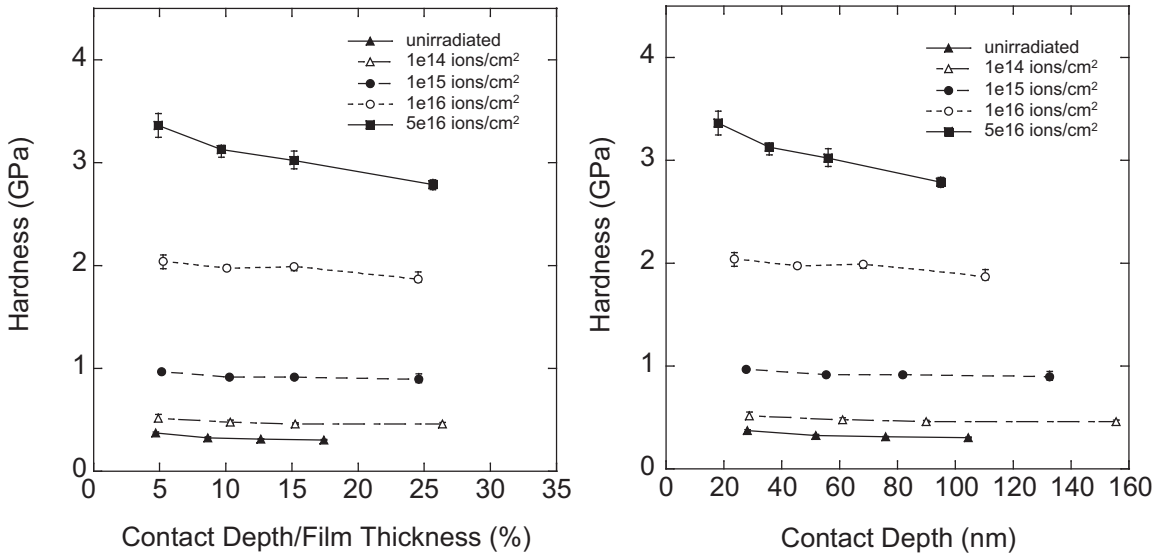

Figure 4.15: Hardness-depth profiles obtained by nanoindentation of the films irradiated with 125 keV H^+ ions at fluences ranging from 1 x 10^{14} to 5 x 10^{16} ions/cm^2. All reported data represent the average of five indentations, and the error bars represent the maximum and minimum values obtained.

ratio between the contact depth and the film thickness. The normalized contact depth allows the comparison of the mechanical properties and hardnesses of films with different thicknesses. The thickness variations result from an increase in film shrinkage with increasing of ion fluence. Also in the same figure the hardness as a function of the contact depth is plotted; this plot helps to relate this data to the implanted results (Figure 4.10). In particular, it can be observed that in the first 100 nm the hardness of the ion (N^+) implanted films drops nearly 75 %, while for the ion (N^{2+}) irradiated films the hardness drops less than 10 %. All reported data represent the average of five indentations, and the error bars represent the maximum and minimum values obtained. A monotonic increase in hardness is observed with increasing fluence. The hardness of the film irradiated with the highest fluence increased an order of magnitude over that of the unirradiated film. The hardness has been observed to exhibit a slight decrease with the increase in penetration depth. The influence of the silicon substrate on these measurements is negligible(the hardness of the substrate was measured to be 11 GPa).

The effect of fluence on the hardness-depth profiles of the films irradiated with H^+ and N^{2+} is shown in Figure 4.16. The hardness of the N^{2+} irradiated film with the highest fluence increased to 7.5 GPa, more than an order of magnitude over that of the unirradiated film. The uncertainty

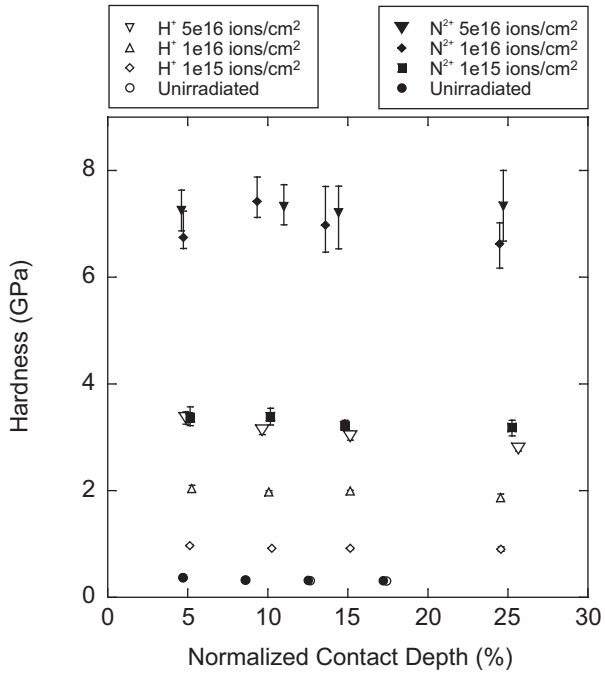

Figure 4.16: Effect of fluence on the hardness for 125 keV H^+ and 250 keV N^{2+} irradiated sol-gel films. All reported data represent the average of five indentations, and the error bars represent the maximum and minimum values obtained.

on the hardness measurements for the N^{2+} irradiation with fluence higher than 1 x 10^{15} ions/cm^2 was seen to increase. It must be noted that the absolute value of the error bars increased, but not the percentage with respect to the mean value of the error bars, which remain under 5 %. The relative increase in hardness for incremental changes in ion fluence was not observed to be constant, but instead varied as a function of the ion species used. This will be investigated in terms of electronic and nuclear stopping power (Section 4.3) as well as hardening cross section (Section 4.5). In particular, the hardening effect exhibited by the sol-gel film after 125 keV H^+ irradiation at a fluence of 5 x 10^{16} ions/cm^2 is similar to the hardening exhibited by a sol-gel film after 250 keV N^{2+} irradiation at a fluence of 1 x 10^{15} ions/cm^2.

The effect of the fluence on the reduced elastic modulus-depth profiles of the films irradiated with H^+ and N^{2+} is shown in Figure 4.17. The reduced elastic modulus was observed to increase with increasing ion fluence. The error bars in this figure represent the maximum and minimum values obtained in 5 experiments conducted for each penetration depth. The reduced elastic modulus was observed to increase with increasing in penetration depth. It was found to exhibit a 4.5 fold increase (7.1 to 32.1 GPa) with increased fluence, for H^+ irradiation, at a normalized contact depth of

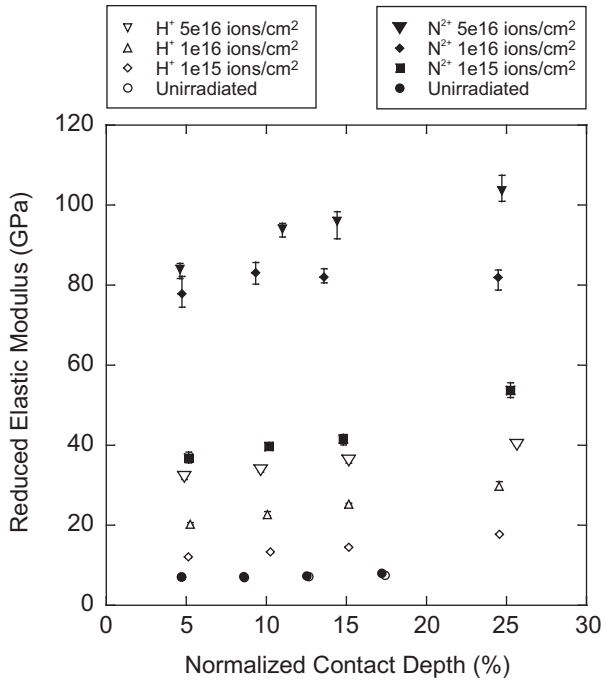

Figure 4.17: Effect of fluence on the reduced elastic modulus for 125 keV H^+ and 250 keV N^{2+} irradiated sol-gel films. All reported data represent the average of five indentations, and the error bars represent the maximum and minimum values obtained.

approximately 5 %. For N^{2+} irradiation, the reduced elastic modulus was found to exhibit a 12 fold increase (7.1 to 84.0 GPa) with increased fluence at a normalized contact depth of approximately 5 %. With the increase in normalized contact depth, the reduced elastic modulus was observed to decrease for ion implanted films and increase for ion irradiated films. This depth profile variation has been attributed to the influence of the reduced elastic modulus of the substrate, which was measured to be 5 GPa for the unimplanted films (implantation) and 150 GPa for the Si substrate (irradiation).

4.3 Effects of Stopping Power and Deposited Ion Energy on the Hardening Process

In this section, results are presented which show that the electronic stopping is the principal responsible for the film hardening, while the role of nuclear stopping is minimal. This result is consistent with similar observations in the literature. This conclusion was drawn by investigating films irradiated with three ion species having similar electronic stopping power but different nuclear stopping

Ion Irradiation	**Si^+**	**O^+**	**N^+**
Ion Beam Energy (keV)	100	100	100
Fluence (1e15 ions/cm^2)	30	30	30
Projected Range (nm)	260	446	469
Film Thickness (nm)	3000	3000	3000
$(dE/dx)_e$ (eV/Å)	19.3	16.7	17.8
$(dE/dx)_n$ (eV/Å)	15.3	4.6	3.3

Table 4.3: Ion irradiation data for ions having approximately equal electronic stopping at the surface $(dE/dx)_e$.

power. The hardening of these three irradiated films was found to be the same.

The hardening process has been observed to depend on the electronic energy deposited in the film. A monotonic increase in hardness with the increase in electronic energy deposited to the film surface was found.

Ion irradiation of the films was performed with a range of ions such that the electronic energy deposited to the films was kept constant. Hardness after irradiation was measured by nanoindentation and was found to depend on the incident ion species. Hardness was also found to have an exponential dependence with H loss in the film. These results indicate that both hardness and H loss are not simply related to electronic energy deposited in the film, but depend also on the ion species. A linear dependence of hardness with electric stopping power at constant electronic energy deposited to the surface was observed.

4.3.1 Electronic vs Nuclear Stopping Power

The electronic and nuclear stopping power effects on the surface mechanical properties of sol-gel films have been investigated. For this purpose, three ion irradiations were considered: Si^+, O^+ and N^+, all performed with a 100 keV energy beam and a fluence of 3 x 10^{16} ions/cm^2. All three ions chosen have approximately equal electronic stopping at the surface, however for the case of Si^+, the nuclear stopping is substantially greater than that of O^+ and N^+. Table 4.3 lists the incident ion energy and fluences used for the three ions considered. Also shown are the values for the film thickness prior to ion irradiation and values for the projected ion range, and the surface electronic and nuclear stopping powers calculated using SRIM [75].

Figures 4.12 and 4.13 (Section 4.2) show the hardness and reduced elastic modulus depth profiles

obtained for the preliminary irradiations performed with Si^+, O^+ and N^+ ions at a fluence of 3 x 10^{16} ions/cm^2. No observable differences in both hardness and reduced elastic modulus can be seen for the three different ions used. Since all three ions have about the same electronic stopping, and Si^+ has a significantly higher value for nuclear stopping, these results indicate that electronic stopping is principally responsible for the film conversion, and that the role of nuclear stopping is minimal. This observation is consistent with the results of Pivin et al. [70] in a recent study of sol-gel derived Si-based films.

4.3.2 Electronic Energy Deposited to the Surface

The electronic energy deposited to the surface has been defined as the electronic stopping power at the surface times the fluence, with units of eV/cm^3 (energy per unit volume). As seen in Section 4.2, Figure 4.16, the hardness of the irradiated films increases monotonically with the increase in fluence. Therefore, since the electronic stopping power at the surface for an ion species with a certain ion beam energy is constant, the increase in hardness can be linked to the increase in electronic energy deposited to the surface. In Figure 4.18, the hardness results seen in Figure 4.16, taken at 5% normalized contact depth, are replotted as a function of the electronic energy deposited to the surface for films irradiated with 125 keV H^+ and 250 keV N^{2+}.

To investigate the effect of electronic stopping on the resulting hardness, the ion fluence was varied such that the electronic energy deposited to the film surface was kept constant at 1.87 x 10^{25} eV/cm^3, while the electronic stopping was varied by the choice of ion. Table 4.4 lists the incident ion energies and fluences used for the Cu^{2+}, N^{2+}, He^+ ions as well as two H^+ ions with different ion beam energy (different projected ranges). Also included for a broader comparison are the ion irradiation parameters for Si^+, O^+ and N^+ ions which were used in a preliminary study on the effects of ion irradiation on surface mechanical properties of nearly identical TEOS/MTES sol-gel films, as discussed in Section 4.2.1 [101]. Table 4.4 also lists the values for the film thickness prior to ion irradiation and values for the projected ion range, the surface electronic and nuclear stopping powers, and the electronic and nuclear energies deposited at the surface calculated using SRIM [75]. In addition to the Cu^{2+}, N^{2+}, He^+ and H^+ irradiations, the Si^+, O^+ and N^+ ions also had approximately equal electronic energy deposited to the film surface.

Recall that for the preliminary ion irradiated films, the hardness measurements were shown to be influenced by the soft unirradiated sol-gel film underneath the hard irradiated layer (Section 4.2.1). Thus, the hardness values which characterizes the ion irradiated layer of the preliminary sol-gel

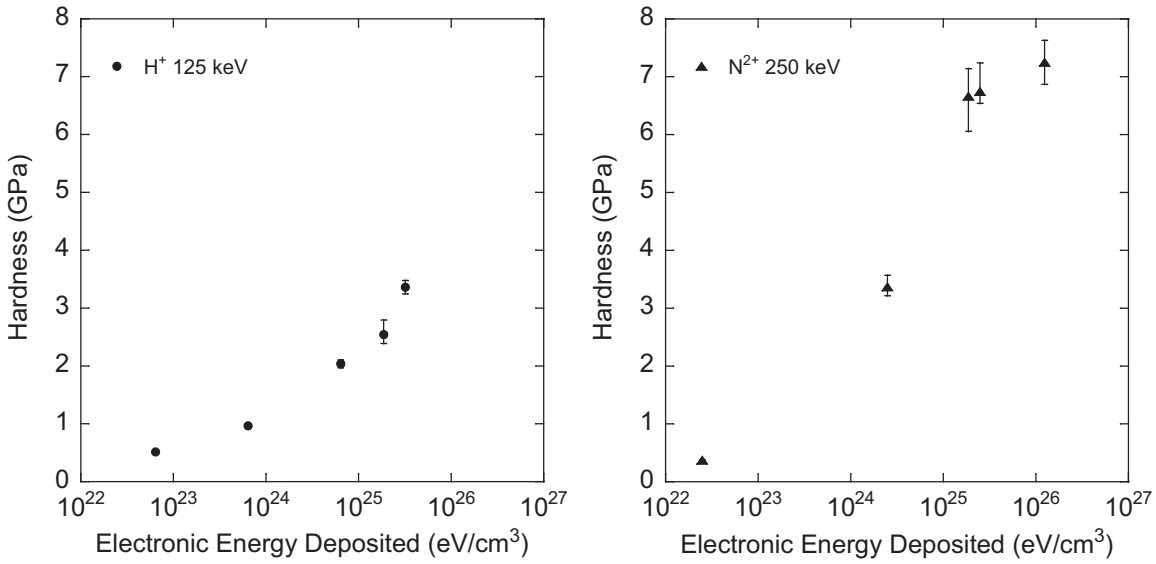

Figure 4.18: Variation of hardness with electronic energy deposited to the surface for H^+ and N^{2+} irradiations. The hardness values here reported are taken at a normalized contact depth of 5%. All reported data represent the average of five indentations, and the error bars represent the maximum and minimum values obtained.

Ion Irradiation	**Cu^{2+}**	**N^{2+}**	**He^+**	**H^+**	**H^+**	**Si^+**	**O^+**	**N^+**
Ion Beam Energy (keV)	2000	250	115	125	115	100	100	100
Projected Range (nm)	2990	1060	1380	2630	1920	260	446	469
Film Thickness (nm)	2700	620	2700	600	2700	3000	3000	3000
Fluence (1e15 ions/cm^2)	3.05	7.5	16.1	29.2	28.8	10.0	10.0	10.0
$(dE/dx)_e$ (eV/Å)	61.2	24.9	11.6	6.4	6.5	19.3	16.7	17.8
$(dE/dx)_n$ (eV/Å)	15.5	1.86	0.12	0.01	0.01	15.3	4.6	3.3
$(dE/dx)_e$* Fluence (1e25 eV/cm^3)	1.87	1.87	1.87	1.87	1.88	1.93	1.67	1.78
$(dE/dx)_n$* Fluence (1e25 eV/cm^3)	0.47	0.14	0.02	0.003	0.003	1.53	0.46	0.33

Table 4.4: Ion Irradiation data

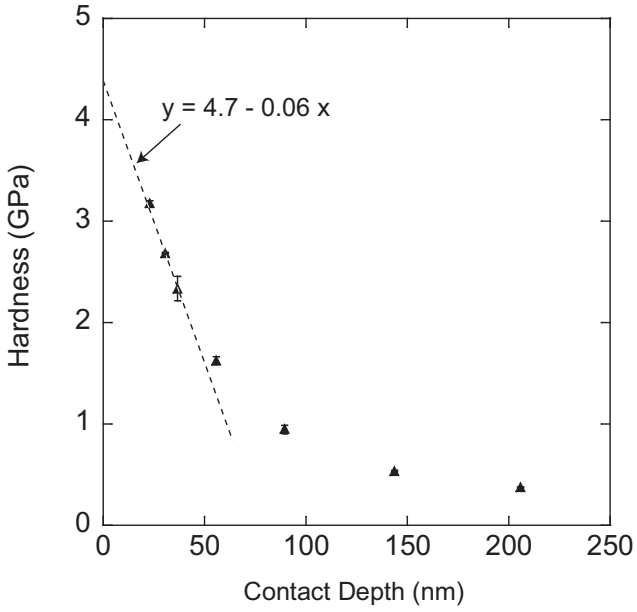

Figure 4.19: Surface hardness extrapolation used for the preliminary sol-gel film irradiated with 100 keV Si^+ ions with a 260 nm projected range, smaller than the film thickness (3 μm). All reported data represent the average of five indentations, and the error bars represent the maximum and minimum values obtained.

films have been considered to be the farthest from the unirradiated layer, i.e., the near film surface hardness. The near film surface hardnesses were extrapolated by a linear fitting of the shallowest data points (those having a contact depth less than 50 nm) of the hardness depth profile, as shown in Figure 4.19. The hardness extrapolated values are used in the plots exhibited in Figures 4.21 and 4.22.

The hardness variation with contact depth for the Cu^{2+}, N^{2+}, He^+, H^+ (115 keV) and H^+ (125 keV) irradiations is shown in Figure 4.20. Also shown is the hardness profile for the unirradiated film. All reported data represent the average of five indentations, and the error bars represent the maximum and minimum values obtained. A significant difference between the hardness measured at the near surface for the various ion irradiation species is observed despite the fact that all irradiations resulted in the same amount of electronic energy deposited at the surface (by design). This indicates that the hardness is not simply related to the electronic energy deposited to the film.

It has been well reported that there is a selective release of H with the irradiation of a wide variety of polymers [70, 106]. Attempts to develop models for this H loss have also been reported [107, 108]. In the present work the variation of hardness with H loss was investigated. Figure 4.21 shows the

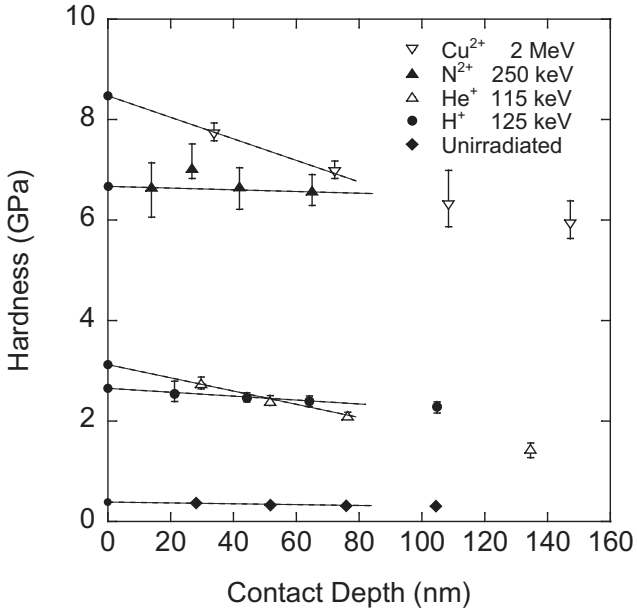

Figure 4.20: Hardness-depth profiles obtained on unirradiated film and for films irradiated with 2 MeV Cu^{2+}, 115 keV He^{+}, 115 keV H^{+}, 250 keV N^{2+}, 125 keV H^{+} ions. All reported data represent the average of five indentations, and the error bars represent the maximum and minimum values obtained.

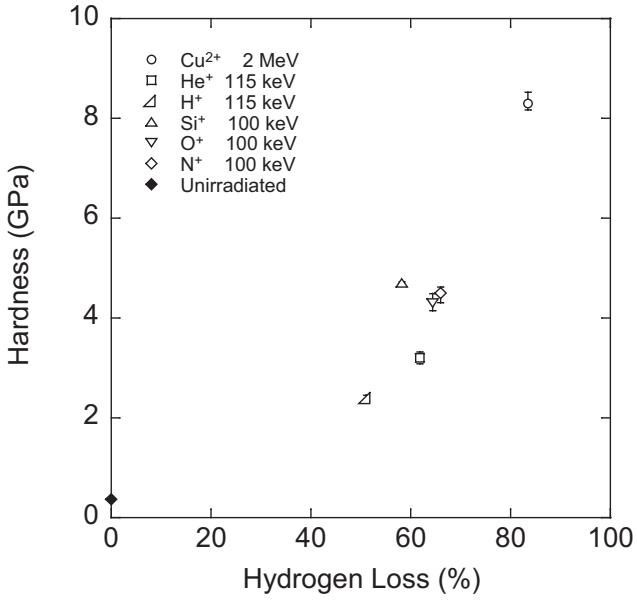

Figure 4.21: Near surface hardness variation with percent hydrogen loss for all ion irradiated films considered. All reported data represent the average of five indentations, and the error bars represent the maximum and minimum values obtained.

results for the increase in hardness with increased H loss as obtained from ERD measurements after irradiation. Shown are the results for the Cu^{2+}, He^{+}, H^{+} irradiations as well as results obtained for films, produced from the same sol, irradiated with Si^{+}, O^{+} and N^{+} ions. A monotonic (exponential) increase in hardness with H loss is observed.

The observation that both hardness and H loss are not simply related to electronic energy deposited to the film surface is consistent with the recent (2004) results of Kucheyev et al. [71] who reported in a study of ion irradiated polyimide that for a given value of electronic energy deposited, irradiation with different ion species results in different values of mechanical properties (including hardness, elastic modulus and tensile strength). The variation of hardness with electronic stopping power at constant electronic energy deposited to the film surface is shown in Figure 4.22. Here, the hardness is seen to monotonically increase with electronic stopping power. In the Kucheyev et al. study on the ion irradiation of polyimide [71], the efficiency for increasing the material's hardness was shown to have an exponential dependence on electronic stopping power, whereas for the present work an approximate linear dependence is observed for electronic stopping power up to 30 eV/Å [109]. For electronic stopping power greater than 30 eV/Å, the hardness increases at a lower rate (compared to those with electronic stopping power less than 30 eV/Å) with increasing

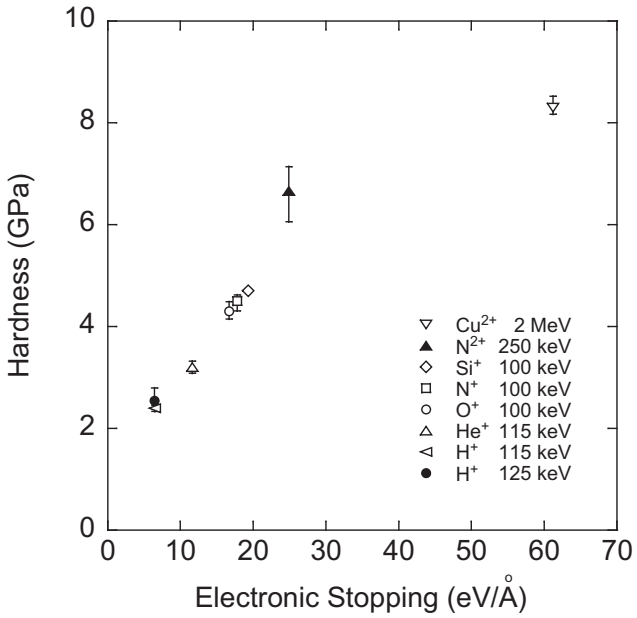

Figure 4.22: Variation of hardness with electronic stopping power for irradiations with nearly the same electronic energy deposited at the surface (1.87 x 10^{25} eV/cm^3). All reported data represent the average of five indentations, and the error bars represent the maximum and minimum values obtained.

electronic stopping power.

4.4 Investigation of the Physical Causes Governing Ion Irradiation Hardening

In this section, the plausible mechanisms for the hardening of the irradiated films are investigated. The increase in mechanical properties of hybrid sol-gel films following ion irradiation is postulated to be linked to structural changes.

In the literature, the hardening of similar sol-gel films due to ion irradiation was explained in terms of either silica clusters cross-linking [58,68], which increased the rigidity of the film, or in terms of carbon cluster precipitation, where the C atoms cluster in a diamond-like structure [60, 61]. In light of the experiments conducted throughout this work, the possibility that these two hypotheses contribute to the observed increase in hardness is investigated in the section below. In particular, ion irradiation was found to result in a cross-linked silica film as well as the segregation of carbon clusters, both of which contribute to increase the mechanical properties of the films. But neither can explain the highest value of hardness.

4.4.1 SiO_2 Cross-linking

The hardening observed after ion irradiation could be justified by the cross linking of silica clusters suggested by the availability of both Si^+ and O^- broken branches on the surface of the silicon cluster, obtained during the sol-gel synthesis, and by the high reactivity among these two ions. Where the Si^+ ions result from the burn out of the methyl group in the Si-CH_3, the O^- ions are provided by the C-O and O-H molecules resulting from incomplete hydrolysis and condensation of the sol-gel film. Moreover, as described in the Section 4.1.2 and shown in Figure 4.2, the atomic ratio of O/Si is seen to increase from 1.4 to 1.7 for ion irradiated films. This movement is consistent with the films' evolution toward a silica based film. That a similar increase in the atomic ratio of O/Si is observed for heat treated films at temperatures from 300 °C to 800 °C, where the hardness increase was much less than irradiated films, suggests that even though the ion irradiated films are transforming into SiO_2 films, this does not justify the hardness increase (0.4 GPa to 7.7 GPa) experienced. This is because the value obtained is higher than the Vickers hardness of silica glass, which is reported to be 635 kg/mm^2 (5.8 GPa) [30]. The Vickers and Berkovich indenters have the same area function ($A = f(h)$, where A is the cross sectional area of the indenter and h is the distance of such cross section from the tip of the indenter), thus the two can be compared.

It was also observed that film shrinkage was correlated with the increase in hardness and reduced

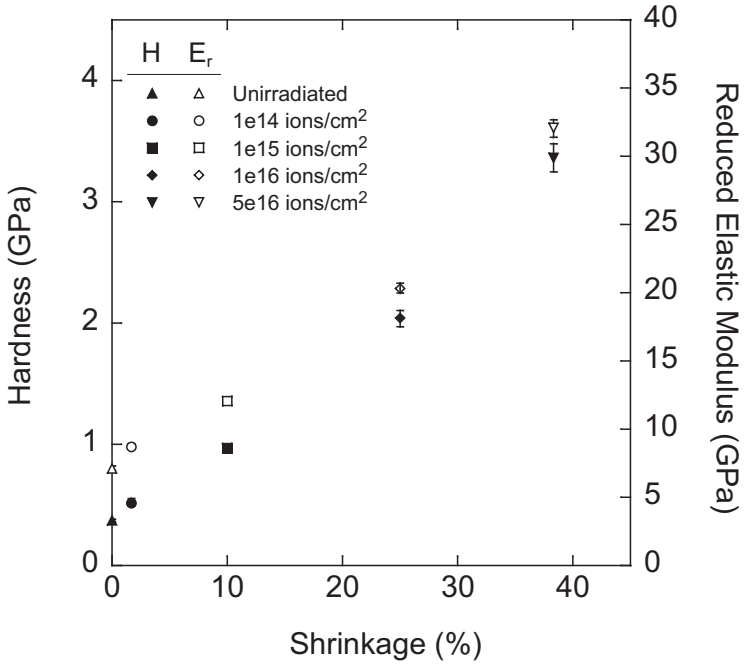

Figure 4.23: Hardness and reduced elastic modulus as a function of film thickness shrinkage for films irradiated with 125 keV H^+ ions at fluences ranging from 1 x 10^{14} to 5 x 10^{16} ions/cm^2. All reported data represent the average of five indentations, and the error bars represent the maximum and minimum values obtained.

elastic modulus as can be observed in Figure 4.23 for the case of 125 keV H^+ irradiated films. The reduced elastic modulus and hardness were observed to increase monotonically with the increase in percentage shrinkage. If the mass is assumed not to change, the shrinkage can be seen as an increase in density. By heat treating a specimen after ion irradiation it was shown that the increase in film density is not the major factor in the hardening process. In particular, a film previously ion irradiated with 125 keV H^+ ions and a fluence of 5 x 10^{16} ions/cm^2 was heat treated at 800 °C for 30 minutes (much higher temperature than the working temperature of these films, 230 °C) and it was found that even though the film shrunk an additional 30 % with respect to the irradiated film, the hardness of the film decreased from 3.4 GPa to 0.8 GPa.

4.4.2 Diamond Like Clusters

The atomic ratio of C/Si, for films heat treated at 600 °C and higher, shows a significant reduction, which is consistent with the thermal decomposition of the Si-CH_3 and PVP organic components, Section 4.1.2. For the ion irradiated film, the atomic ratio of C/Si shows little change from that

prior to irradiation (Figure 4.2). This result suggests different decomposition kinetics of the organic components by ion irradiation when compared to the heat treatment process. The fact that the C atoms are still present in the film after ion irradiation and that the film experiences a drastic loss of H, suggests a selective release of H due to ion irradiation and the possibility of C precipitation in the form of clusters as has been reported by Pivin et al. [62, 96].

In the present work, the formation of carbon clusters and their nature, graphite or diamond like structure, was investigated by Raman spectroscopy. The films irradiated with high fluences showed the presence of carbon clusters in the form of amorphous carbon, with two Raman shift peaks centered at 1386 and 1584 cm^{-1} [57]. In order to determine the influence of those carbon clusters on the ion irradiation hardening process, the ion irradiation process was performed on a sol-gel film with very low C content. Recall that the atomic ratio of C/Si showed a significant reduction for films heat treated at 600 °C and higher (Figure 4.2). In particular, the C/Si ratio went from 1.25 to less than 0.1 for films heat treated at 800 °C. For this purpose, a film heat treated at 800 °C for 10 minutes was ion irradiated by 250 keV N^{2+} ions. The hardness results obtained, in comparison with the same type of irradiation for a film heat treated at 300 °C for 10 minutes, are shown in Figure 4.25. This experiment showed that C concentration has no influence on the maximum hardness reached by ion irradiation suggesting that the carbon clusters have little influence on the hardening of the sol-gel films.

4.4.3 Structural Changes

The structural changes of a film heat treated at 300 °C for 10 minutes followed by ion irradiation are investigated by nanoindentation, photoluminescence spectroscopy, Raman spectroscopy, ERD, and XPS.

ERD has shown a loss of more than 50% hydrogen after ion irradiation, as presented in Figure 4.26 (see also Figure 4.21 for the hydrogen loss due to different ion species). Figure 4.26 represent the variation in ERD with respect to channels which can be related to back-scattering energy, thus it can be though as a ERD-depth plot due to the relation between the ion beck-scattered energy and the depth at which the ion was scattered. The presence of excess hydrogen in unirradiated 300 °C films could be due to the presence of organic components like Si-CH_3 and PVP. These two molecules are both thermally stable up to 400-450 °C [20, 21, 24, 25].

The presence of organic molecules in unirradiated 300 °C films was also confirmed by XPS measurements. XPS was used to provide further insight into the changes in chemical bonding

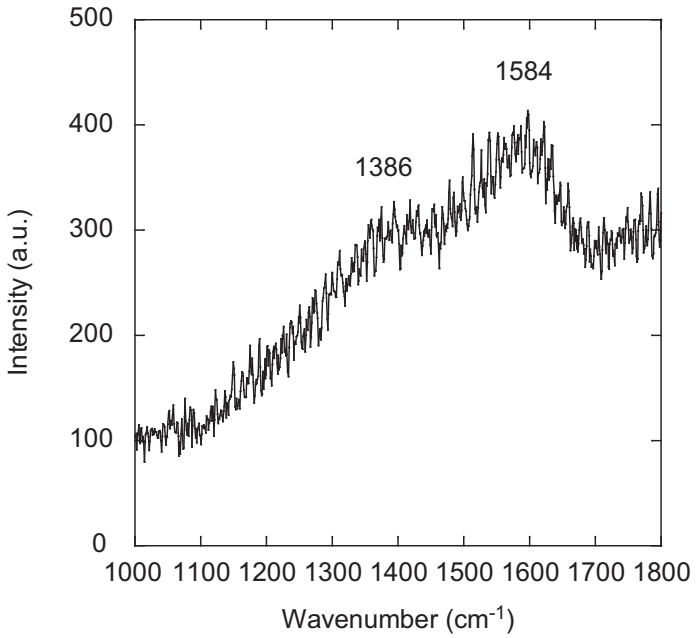

Figure 4.24: Raman spectra for a sol-gel film irradiated with 125 keV H^+ ion with a 5 x 10^{16} ions/cm^2 fluence.

	% C	% O	% Si
Non Irradiated	47.6	31.3	21.1
Ion Irradiated	45.1	33.5	21.4

Table 4.5: Atomic % evaluated by XPS

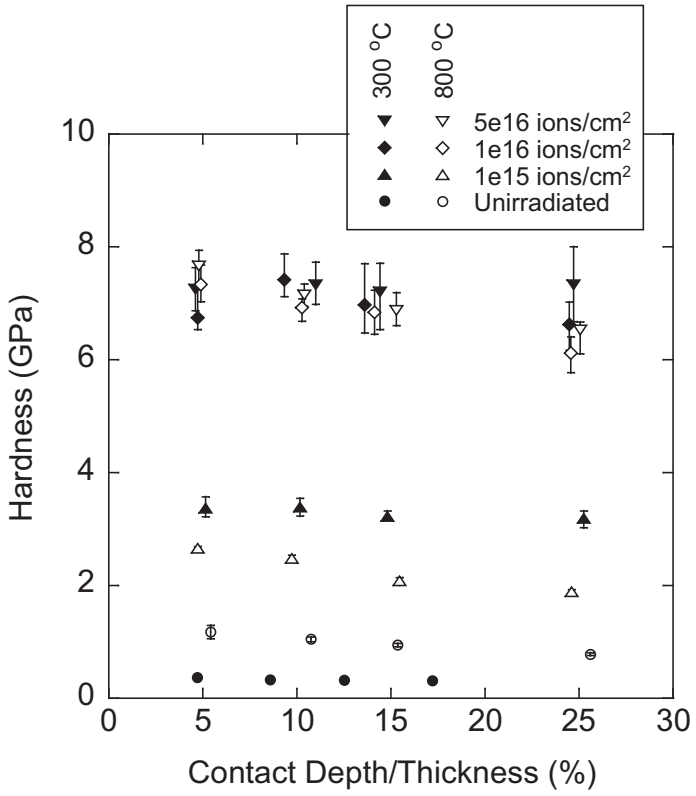

Figure 4.25: Effect of 250 keV N^{2+} ion with the increase in fluence for sol-gel films preheated at 300 and 800 °C for 10 minutes. The full symbols represent the specimens preheated at 300 °C and the empty symbols represent the specimens preheated at 800 °C. All reported data represent the average of five indentations, and the error bars represent the maximum and minimum values obtained.

caused by ion irradiation. XPS measurements indicate that C, O and Si are the principal elements present in both the non irradiated and irradiated samples. The percentage of C, O, and Si does not appreciably change after ion irradiation, as shown in Table 4.5; the uncertainty on the values reported is ±2%. As can be noticed from Table 4.5, the concentration of C is very high suggesting the presence of a high concentration of organic molecules on the films heat treated at 300 °C.

The majority of the carbon atoms in hybrid MTES/TEOS films heat treated at 300°C is expected to be in the form of C-H and C-Si bonds, which are both present in the Si-CH_3 organic component introduced by MTES (CH_3-Si-$(OC_2H_5)_3$). Si-CH_3 is expected to be thermally stable up to 400-450 °C [20, 21]. C atoms are also within carbon-oxygen bonds, and these bonds can be found either in C-O-Si bridging sites [110, 111] or C=O terminal units [24, 25]. C-O-Si bonds are linked to an incomplete hydrolysis of TEOS and MTES [112], as well as the thermal decomposition of the acetic acid used in the sol-gel synthesis [45]. The double carbon-oxygen bonds are mainly present in the PVP molecules, which were added during the sol-gel synthesis, with the intent to increase the critical film thickness. The PVP molecules were reported to be thermally stable up to approximately 430 °C [24, 25].

Since the hardness reached by the ion irradiated film with very low C concentration is identical to the hardness reached by films rich in C, the C atoms are believed to have a marginal effect on

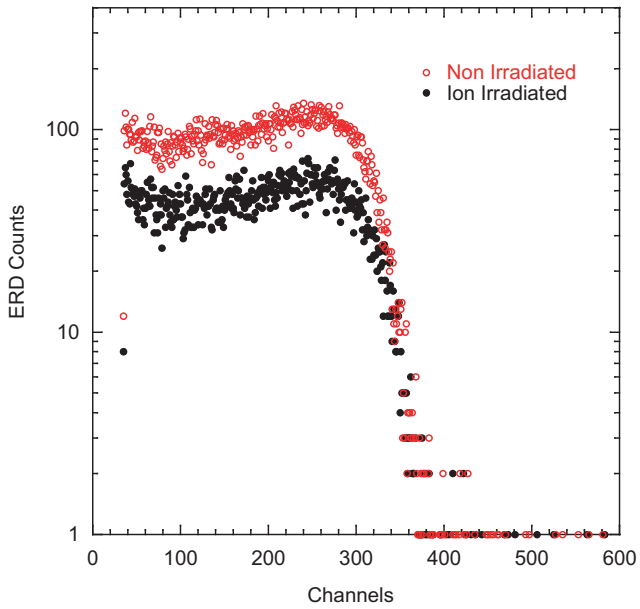

Figure 4.26: Elastic Recoil Detection - 50% decrease in H due to radiolysis for a sol-gel film irradiated with 2 MeV He^+ ions.

the hardening process. Thus, it is believed that ion irradiation reduces the Si-C bond concentration in the hybrid sol-gel films. The Si-C bond represents the bridge between the inorganic SiO_2 clusters and the organic CH_3 molecules in the Si-CH_3 branch. The broken Si- bonds can possibly recombine with oxygen atoms from broken C-O bonds. Another source of oxygen atoms may come from the hydroxyl group (OH), which results from an incomplete condensation [113]. The Si-O recombination is believed to cross-link SiO_2 clusters otherwise separated, forming a compact SiO_2 matrix. The size of the C1s peak (observed by XPS measurements), related to the percentage of C-H/C-C bonds, was found to increase by approximately 28 % as the H content decreased by 50 % after ion irradiation. This suggests that prior to ion irradiation, the XPS peak at 285.0 eV represents mostly C-H bonds. Due to the release of hydrogen during ion irradiation, the carbon atoms from the broken C-H bonds may cluster in the form of C-C [62, 96].

The decrease in H_2 content observed in these experiments was also observed in several other hybrid sol-gel and inorganic polymer ion irradiated films [59, 60]. One advantage of ion irradiation over heat treatment is its selectivity to release only hydrogen atoms. Heat treatment releases instead the entire organic molecule CH_3 with consequent loss of C atoms, which in irradiated films can precipitate out in the form of either graphite or diamond-like clusters [61].

In conclusion, comparing what the literature proposes for hardening mechanisms with the results obtained, it is postulated that both silica clusters cross-linking and carbon segregation are taking place due to ion irradiation, and that both contribute to increase the hardness of the irradiated films. But neither is considered the cause of the highest hardness achieved. Thus, the hardening mechanism is still unclear.

The two structural changes proposed in the literature: silica clusters cross-linking and carbon segregation are schematically represented in Figure 4.27.

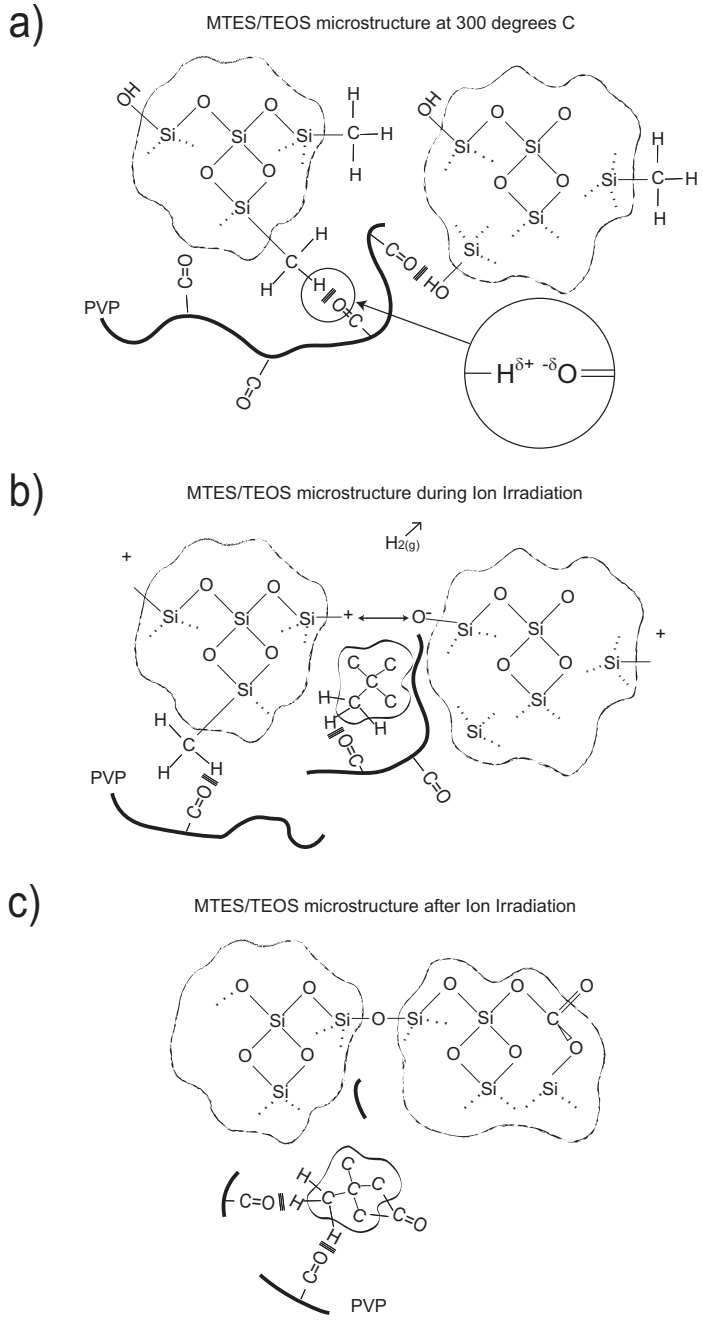

Figure 4.27: Microstructure evolution during ion irradiation.

4.5 Ion Irradiation Hardening - Model

The model put forth is based on the review of a collection of mathematical models describing semiconductors phase transformation induced by ion irradiation introduced by Sickafus et al. [114]. In particular, the simplest rain-drop model of Gibbons [5] known as the, "Direct Impact Model", was modified (Model A below) in order to describe the hardening of the film passing from a soft polymer sol to a hard ceramic type film.

Section 4.3 discussed experiments that showed that the hardening of the sol-gel film depends on the ion species used to irradiate the film. Thus, each ion species has its own hardening efficiency that can be quantified by what will be referred to as a "Hardening Cross-Section", denoted by σ. The hardening cross-section is defined as the cross-sectional area that has been modified (hardened) by the interaction of the impinging ion and the target, in this case the sol-gel film. Thus the greater the cross-sectional area, the more effective the ion is at hardening the film. The size of the cross-sectional area is assumed to be a function of the ion species used. A sketch showing the hardening cross-section is shown in Figure 4.28, where the shaded circular area represents the area that has been modified by an ion impinging on the surface, and the clear area is the unmodified region.

Model - A

This is a simplified model which assumes that the film can only be in one of the two following states: soft unirradiated film or fully hardened irradiated film; thus regions exhibiting multiple hits (hardening cross-section overlapping) have the same hardness as the region hit only once.

Consider a unit surface area, A, and let f_u be the fraction of area A that is not hardened after irradiation with a fluence, ϕ, and let f_h be the fraction of area A that is hardened due to irradiation with a fluence, ϕ. Thus, the probability that a given ion impinging on the surface hits an unirradiated region is $f_u(\sigma, \phi)$ while the probability that it hits a region already irradiated is $f_h(\sigma, \phi)$, where

$$f_u(\sigma, \phi) + f_h(\sigma, \phi) = 1 \tag{4.1}$$

Both f_u and f_h are functions of the hardening cross-section (f_u decreases and f_h increases with increasing σ) and the fluence (f_u decreases and f_h increases with increasing ϕ).

The hardness of a film, H, is defined as the ratio between the maximum load applied to the indenter, P_{max}, and the contact area A between the indenter and the specimen evaluated at P_{max} (Section 3.2):

$$H = \frac{P_{max}}{A}$$

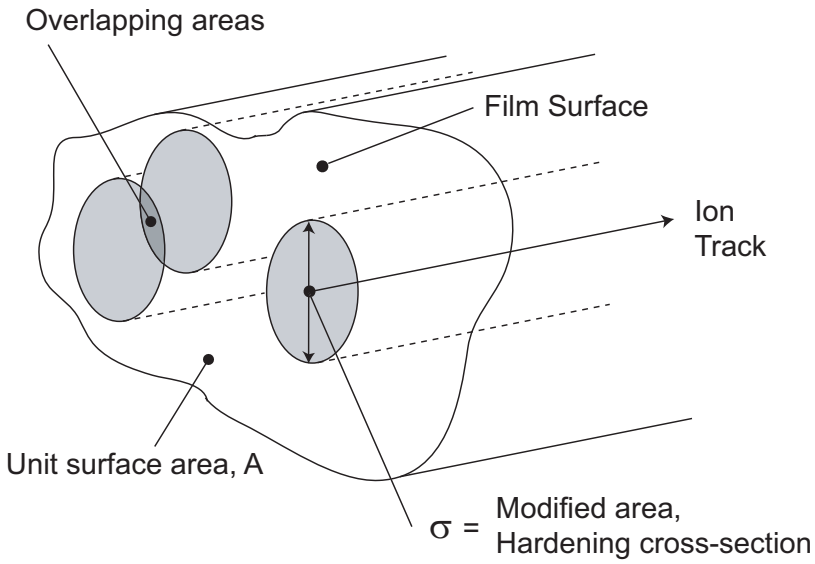

Figure 4.28: The hardening cross-section of an ion impinging on a surface of unit area, A.

Assuming that an ion impact hardens the material from H_{min} to H_{max} and the validity of the superposition principle of the load supported by the unirradiated area and the load supported by the irradiated area:

$$P_{max} = P_u + P_h = H_{min} f_u(\sigma, \phi)A + H_{max} f_h(\sigma, \phi)A$$

where H_{min} represents the hardness of the unirradiated material while H_{max} represents the hardness of the irradiated material. The hardness of the film can then be expressed by:

$$H = H_{min} f_u(\sigma, \phi) + H_{max} f_h(\sigma, \phi) \tag{4.2}$$

or

$$H = H_{max} - \Delta H f_u(\sigma, \phi) \tag{4.3}$$

$$\Delta H = H_{max} - H_{min}$$

As an analogy, this problem can be seen as trying to determine the probability that a rain drop of a certain diameter will fall on a wet piece of land at a certain time after the rain started (also know as the rain-drop model). Taking the rain drop to represent a single bombarded ion, the diameter of the rain drop is analogous to the diameter of the hardening cross-section, and the time is analogous to the fluence (ions/cm^2) times the incident ion energy (eV) divided by the beam current (μA/cm^2) (the incident ion energy and the beam current are both constant).

From the definition of $f_u(\sigma,\phi)$ and $f_h(\sigma,\phi)$, $f_u(\sigma,\phi)$ is expected to diminish while $f_h(\sigma,\phi)$ is expected to grow (by the same quantity) with increasing fluence. In fact, the probability that an ion impinging on the target surface hits an unirradiated region decreases with increasing fluence (negative sign in Equation 4.4 below) and with increasing hardening cross-section, thus the derivative of the probability $f_u(\sigma,\phi)$ and $f_h(\sigma,\phi)$ with respect to σ (representing the variation of $f_u(\sigma,\phi)$ and $f_h(\sigma,\phi)$ with respect to σ) can be expressed as:

$$\begin{aligned} \frac{df_u(\sigma,\phi)}{d\phi} &= -\sigma f_u(\sigma,\phi) \\ \frac{df_h(\sigma,\phi)}{d\phi} &= +\sigma f_u(\sigma,\phi) \end{aligned} \tag{4.4}$$

where, the dimensions of ϕ and σ are ions/cm^2 and cm^2, respectively. The above equations assume that once one ion impinges in a region, that region get hardened to a maximum value H_{max}. This assumption was used by Gibbons in a model describing the transformation from crystalline to amorphous phase in irradiated semiconductor materials [5]. No additional assumptions will be added in the mathematical solution of Model A. The solutions of these differential equations are:

$$\begin{aligned} f_u(\sigma,\phi) &= e^{-\sigma\phi} \\ f_h(\sigma,\phi) &= 1 - e^{-\sigma\phi} \end{aligned} \tag{4.5}$$

and thus the hardness can be described by the following equation:

$$H(\sigma,\phi) = H_{max} - \Delta H e^{-\sigma\phi} \tag{4.6}$$

Model - B

This model take in consideration the hardening cross-section overlapping regions by assuming the derivative of the probability function with respect to the fluence to be dependent upon the fluence.

Consider a unit surface area, A, and let f_0 be the fraction of area A that is not hardened after irradiation with a fluence ϕ, let f_1 be the fraction of area A that has been hit by one ion after a fluence ϕ, and let f_n be the fraction of area A that has been hit by n ions after a fluence, ϕ. Thus, the relation between these probabilities (fractional areas) is:

$$f_0(\sigma_1,\phi) + f_1(\sigma_2,\phi) + \ldots + f_1(\sigma_3,\phi) = 1 \tag{4.7}$$

In this model each probability has a different hardening cross-section, since the effect caused by the ion interaction with a region that has been already hit by an ion might be different than the effect caused by the interaction of the same ion with an unmodified region. Another way to see this is by the fact that the hardening cross-section is expected to depend not only on the ion species but also on the target being irradiated, thus the hardening cross-section is expected to change as a function of the degree of film conversion, i.e., the hardness of the film. In particular, the cross-section is expected to decrease with increasing fluence. Also the hardness of a region hit once might be different than the hardness of a region hit n times, thus the hardness of the film as a function of fluence can be written as:

$$H = H_0 f_0(\sigma_0, \phi) + H_1 f_1(\sigma_1, \phi) + \ldots + H_n f_n(\sigma_n, \phi) \tag{4.8}$$

This model is introducing a very high number of variables (σ_0, σ_1, ..., σ_n, H_1, ..., H_n) which do not help to link the model to the parameters of the ion used as well as to compare different ion sources. Since there is no benefit to determining the intermediate hardness reached by each number of ion hit, this model was modified in order to consider the variation in mechanical behavior of region hit several times by keeping the number of variable limited to only to three: H_{max}, $\bar{\sigma}$, and a, as will be described below. Mathematically this can be done by considering each region hit by n ions as the superposition of a region that has not been hit and a region that has been hit to its maximum hardness:

$$H_1 f_1(\sigma_1, \phi) = H_{min} f_{1u}(\sigma, \phi) + H_{max} f_{1h}(\sigma, \phi) \tag{4.9}$$

where the hardening cross-section is not constant (for a specific incident ion like in Model A) but changes with fluence. Than the hardness of the film at a fluence ϕ can be written as:

$$H = H_{min} f_u(\sigma, \phi) + H_{max} f_h(\sigma, \phi) \tag{4.10}$$

where

$$f_u(\sigma, \phi) = f_0(\sigma_0, \phi) + f_{1u}(\sigma, \phi) + \ldots + f_{(n-1)u}(\sigma, \phi) \tag{4.11}$$

$$f_h(\sigma, \phi) = f_{1h}(\sigma, \phi) + \ldots + f_{(n-1)h}(\sigma, \phi) + f_{nh}(\sigma, \phi)$$

considering the nth hit the one that converts the film to its maximum hardness (saturation).

Equation 4.10 is similar to Equation 4.2 of Model A, with the only difference that the hardening cross-section is fluence dependent, thus the differential equations in Equation 4.4 can be modified as:

$$\frac{df_u(\sigma,\phi)}{d\phi} = -\sigma(\phi) f_u(\sigma,\phi) \tag{4.12}$$
$$\frac{df_u(\sigma,\phi)}{d\phi} = +\sigma(\phi) f_u(\sigma,\phi)$$

These two differential equations have to be solved mathematically by guessing a function for $\sigma(\phi)$ and finding $f_u(\sigma,\phi)$ that satisfy both equations, thus no further assumptions are introduced during the solution of these equations. $\sigma(\phi)$ is guessed to be a power function of the fluence, which is the simpler function which satisfies the unit of $\sigma(\phi)$ (cm^2) and also easier to integrate with respect to ϕ:

$$\sigma(\phi) = \beta^a \phi^{a-1} \tag{4.13}$$

where a (which will be called the hardening coefficient) and β are constants depending on the ion species and target used. Thus the Equations 4.12 can be written as:

$$\frac{df_u(\sigma,\phi)}{d\phi} = -\beta^a \phi^{a-1} f_u(\sigma,\phi) \tag{4.14}$$
$$\frac{df_u(\sigma,\phi)}{d\phi} = +\beta^a \phi^{a-1} f_u(\sigma,\phi)$$

and the solutions of the above differential equations are:

$$f_u(\sigma,\phi) = e^{-\frac{1}{a}(\beta\phi)^a} = e^{-\frac{1}{a}\sigma\phi} \tag{4.15}$$
$$f_h(\sigma,\phi) = 1 - e^{-\frac{1}{a}(\beta\phi)^a} = 1 - e^{-\frac{1}{a}\sigma\phi}$$

In order to compare the hardening effect of two different ion species it is necessary to introduce the hardening cross-section constant, $\bar{\sigma}$, defined as the value of the hardening cross-section evaluated at a fluence for which the hardness of the target matter increases by (1 - 1/e)*100 (corresponding to 63 %) of ΔH (Eq. 4.3). This particular value of fluence, $\bar{\phi}$, can be determined by equating the probability $f_u(\sigma,\phi)$ to 1/e:

$$f_u(\sigma,\bar{\phi}) = e^{-\frac{1}{a}(\beta\bar{\phi})^a} = \frac{1}{e} \tag{4.16}$$

where $\bar{\phi}$ will be called the fluence constant analogous to the time constant in a linear time-invariant system, i.e., RC circuits.

Thus the fluence constant can be calculated to be:

$$\frac{1}{a}(\beta\bar{\phi})^a = 1 \tag{4.17}$$
$$\bar{\phi} = \frac{a^{\frac{1}{a}}}{\beta}$$

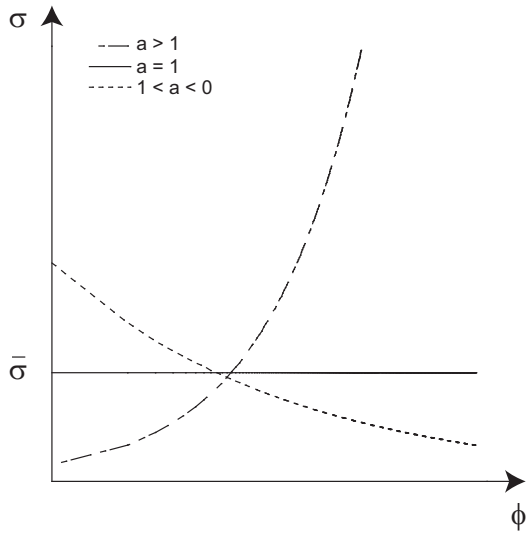

Figure 4.29: Qualitative behavior of the hardening cross-section as a function of the ion fluence for different values of hardening coefficient (thus for different ion species)

and the hardening cross-section constant can than be expressed as:

$$\bar{\sigma} = \sigma(\bar{\phi}) = \beta^a \bar{\phi}^{a-1} = \beta a^{\frac{a-1}{a}} \tag{4.18}$$

Now Equations 4.13 and 4.15 can be rewritten as a function of $\bar{\sigma}$:

$$\sigma(\phi) = \bar{\sigma}^a \left(\frac{\phi}{a}\right)^{a-1} \tag{4.19}$$

Figure 4.29 shows the influence of a on the variation of hardening cross-section. Equation 4.19 will now be substituted into Equations 4.15 to obtain:

$$f_u(\bar{\sigma}, \phi) = e^{-a^{\frac{1-2a}{a}}(\bar{\sigma}\phi)^a} \tag{4.20}$$
$$f_h(\bar{\sigma}, \phi) = 1 - e^{-a^{\frac{1-2a}{a}}(\bar{\sigma}\phi)^a}$$

Figure 4.30 shows the influence of a and $\bar{\sigma}$ on the variation of $f_h(\bar{\sigma}, \phi)$, which is linearly proportional to the increase in hardness.

The increase in hardness can finally be described by the following equation:

$$H(\sigma, \phi) = H_{max} - \Delta H e^{-a^{\frac{1-2a}{a}}(\bar{\sigma}\phi)^a} \tag{4.21}$$

Physically the hardening cross-section constant $\bar{\sigma}$ represents a characteristic cross-sectional area which has been modified due to the interaction between the ion and the target. The greater the

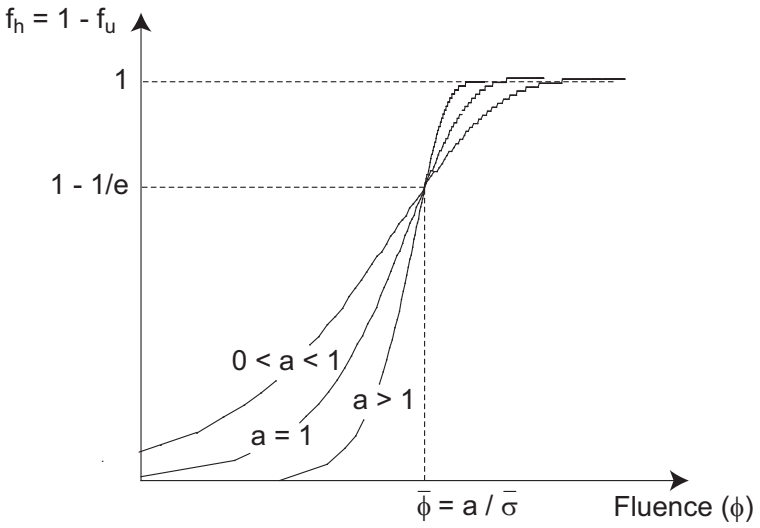

Figure 4.30: Qualitative behavior of the probability $f_h(\bar{\sigma}, \phi)$ as a function of the ion fluence for different value of hardening coefficient (thus for different ion species)

value of $\bar{\sigma}$, the greater the hardening effect of the ion species used. With the increase in fluence (ions per cm^2) the target matter modifies from a soft sol-gel film to a ceramic like film. This transformation shows a gradual increase in hardness, thus the target changes its characteristic with increasing fluence. For this reason, the hardening cross-section is believed to vary proportionally to the degree of modification, and the hardening coefficient a is an index which is proportional to the hardening cross-section gradient with respect to fluence. For instance, when $1 > a > 0$, the gradient of the hardness cross-section decreases with respect to the fluence or in regards to multiple ion hits, a smaller value of a will require that more ion hits be needed in the same region in order to harden the film. For $a > 1$, the gradient of the hardening cross-section increases with respect to the fluence, however a value of $a > 1$ is not physically possible due to the fact that the film cannot be hardened with less than one hit (Figure 4.30). Model A is a particular case of Model B, and it can be obtained from Model B by using a value for the hardening coefficient, $a = 1$. In this study the hardening coefficient is expected to vary in the range from 1 to 0. The hardening coefficient can also be expressed as:

$$a = \bar{\sigma}\bar{\phi} \tag{4.22}$$

by multiplying $\bar{\sigma}$ by $\bar{\phi}$ from equations 4.17 and 4.18.

Fitting

The hardness data, obtained from irradiations with a projected range greater than the target film thickness, was fitted using both models. The measured hardness values as a function of ion fluence for the 250 keV N^{2+} and 125 keV H^{+} ion irradiated films are shown in Figure 4.31 and 4.32 (the fluence (x axis) has been plotted on a logarithmic scale).

The hardness data was fitted using both Model A (Figure 4.31) and Model B (Figure 4.32). Considering Model B, the hardening cross-section for the H^{+} irradiation was found to be 0.30 $Å^2$ thus having a hardening cross-section radius of 0.31 Å, and the hardening cross-section for the N^{2+} irradiation was found to be 3.17 $Å^2$ thus having a hardening cross-section radius of 1.00 Å. The hardness coefficient was found to be smaller for the case of H^{+} irradiation (0.57) compared to the case of N^{2+} irradiation (0.70). Therefore, the N^{2+} irradiation hardening is expected to pass from H_{min} to H_{max} over a shorter fluence range (from approximately 1 x 10^{13} to 1 x 10^{16} as shown in Figure 4.32) than the H^{+} irradiation (from approximately 1 x 10^{13} to a value greater than 1 x 10^{17} as shown in Figure 4.32).

The hardening effect of a sol-gel film heat treated at 800 °C before ion irradiation is also fitted with Model B. Figure 4.33 compares the hardening effect of two target films having different initial mechanical properties. As expected, for the two irradiations, the values of the hardening coefficient are very different while the hardening cross-section constants remain similar. This strengthens the link between the hardening coefficient and the properties of the target material.

The hardening cross-section is postulated to be related to the electronic stopping power, in particular the hardening cross-section is expected to increase monotonically with increasing electronic stopping power.

$H = H_{max} - (H_{max} - H_{min}) * \exp\{-\sigma\phi\}$				
	H^+	H^+ Error	N^{2+}	N^{2+} Error
H_{max} (GPa)	3.2826	0.11902	6.9228	0.069316
H_{min} (GPa)	0.41067	0.041669	0.37166	0.033308
σ (Å^2)	0.7141	0.11428	6.0176	0.34406

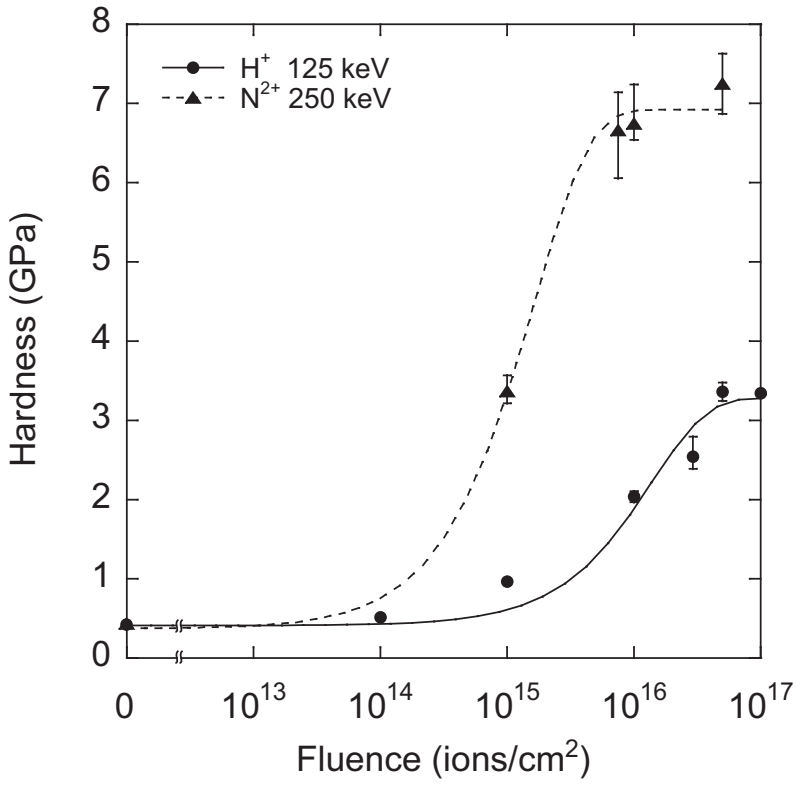

Figure 4.31: Hardening process as a function of N^{2+} and H^+ ion irradiation fluence (fitted following Model A). All reported data represent the average of five indentations, and the error bars represent the maximum and minimum values obtained.

$H = H_{max} - (H_{max} - H_{min}) * \exp\{-(a^{\wedge}[(1-2a)/a])(\bar{\sigma}\phi)^a\}$				
	H^+	H^+ Error	N^{2+}	N^{2+} Error
H_{max} (GPa)	3.6837	0.24863	7.2331	0.037187
H_{min} (GPa)	0.37283	0.027016	0.36946	0.010801
$\bar{\sigma}$ (Å^2)	0.29967	0.10931	3.1707	0.15717
a	0.57329	0.065086	0.69776	0.015059

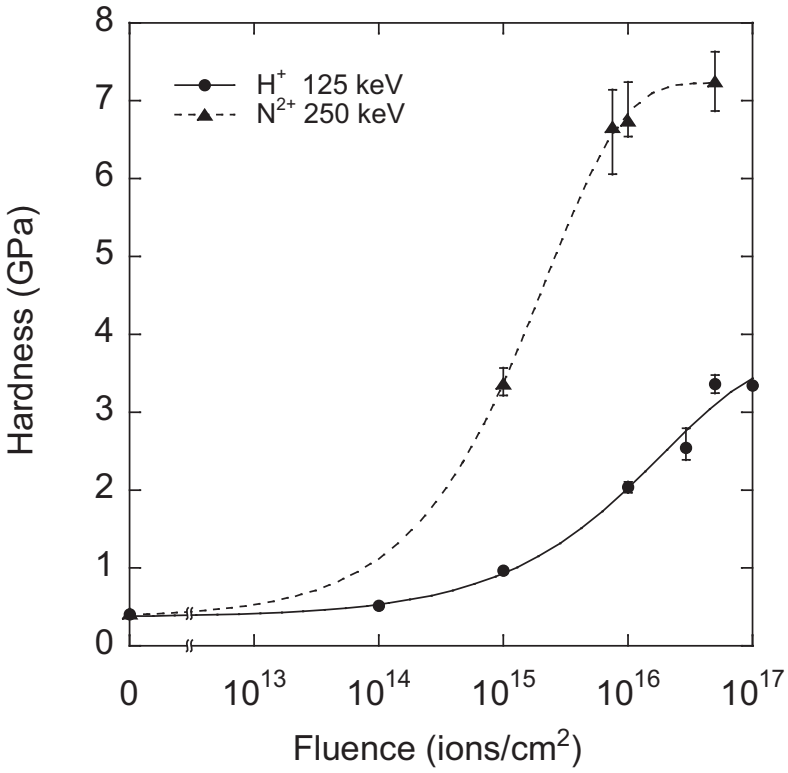

Figure 4.32: Hardening process as a function of N^{2+} and H^+ ion irradiation fluence (fitted following Model B). All reported data represent the average of five indentations, and the error bars represent the maximum and minimum values obtained.

$H = H_{max} - (H_{max} - H_{min}) * \exp\{-(a^{[(1-2a)/a]})(\bar{\sigma}\phi)^a\}$				
	300 ^oC N^{2+}	300 ^oC Error	800 ^oC N^{2+}	800 ^oC Error
H_{max} (GPa)	7.2331	0.037187	7.6627	0.037187
H_{min} (GPa)	0.36946	0.010801	1.1779	0.010801
$\bar{\sigma}$ (Å^2)	3.1707	0.15717	2.9726	1.0335e-4
a	0.69776	0.015059	1	0

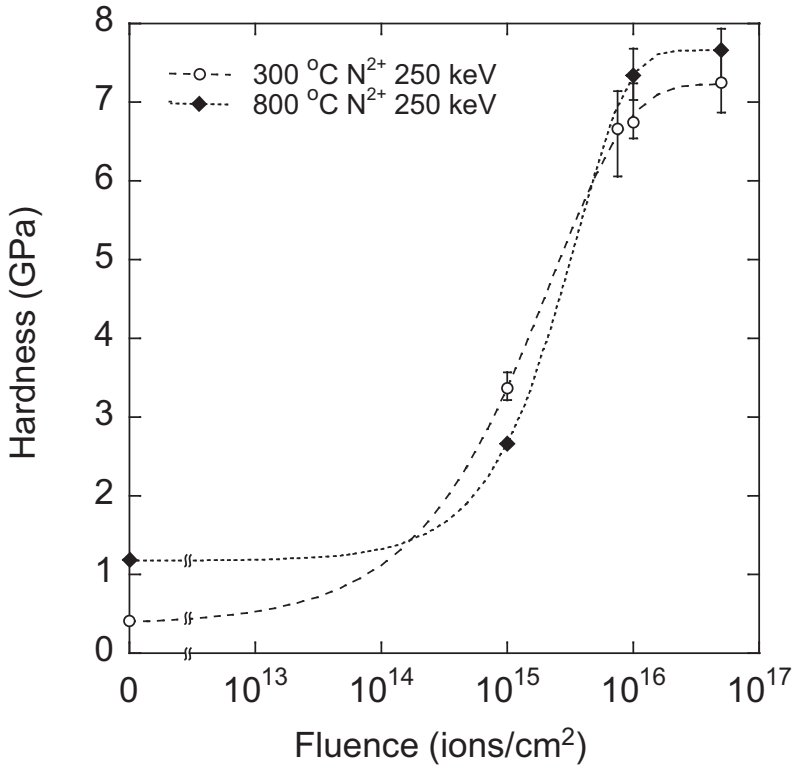

Figure 4.33: Hardening process as a function of N^{2+} ion irradiation fluence for target films heat treated at 300 and 800 °C before ion irradiation (fitted following Model B). All reported data represent the average of five indentations, and the error bars represent the maximum and minimum values obtained.

Chapter 5

Conclusions and Future Work

A study on the effects of ion irradiation on the surface mechanical behavior of hybrid sol-gel derived thin films has been performed. All films investigated were synthesized by sol-gel processing from tetraethoxysilane (TEOS) and methyltriethoxysilane (MTES) precursors and spin-coated onto (100) Si substrates. The synthesized films were investigated by nanoindentation, photoluminescence spectroscopy, and Raman spectroscopy.

5.1 Conclusions

The major conclusions of this work are:

1. The hybrid TEOS/MTES sol-gel films modified by ion irradiation with electronic energy of 1.87 x 10^{25} eV/cm^3 or higher showed higher values of reduced elastic modulus and hardness than 800 °C heat treated films. Ion irradiation was found to be an effective means in converting the polymer sol into ceramic type coatings.

2. Both the reduced elastic modulus and hardness were seen to increase monotonically with the increase in ion fluence, with a maximum hardness of 7.7 GPa (19 fold increase with respect to the unirradiated film hardness of 0.4 GPa) and a maximum reduced elastic modulus of 84.0 GPa (12 fold increase with respect to the unirradiated film reduced elastic modulus of 7.1 GPa).

3. The electronic stopping power was found to be principally responsible for the film hardening, while the role of nuclear stopping power was minimal. A monotonic increase in hardness with the increase in electronic energy deposited to the film surface was found.

4. The hardness was found to be not simply related to electronic energy deposited in the film, but also dependent on the ion species. A linear dependence of hardness with electronic stopping power at constant electronic energy deposited to the surface was observed.

5. The increase in mechanical properties of hybrid sol-gel films following ion irradiation is postulated to be linked to structural changes. Ion irradiation results in a cross-linked silica film as well as the segregation of carbon clusters, both of which contributed to increase the mechanical properties of the films. But neither could explain in full the highest hardness achieved.

6. A model describing the hardening effect of ion irradiating films was presented. The model is based on a rain-drop type model introduced by Gibbons. In the model put forth in this study, the cross-sectional area transformed by the interaction of the incident ion with the target matter was considered to vary with fluence. This assumption is based on the fact that the hardening cross-section is not related to the physical dimension of the incident ion but on its electronic disturbance with the target matter, which is influenced by the properties of the target.

   Knowing that the hardening process depends upon the ion irradiated species, the model characterizes the hardening effectiveness of the ion species considered by two parameters: the constant hardening cross-section and the hardening coefficient. The constant hardening cross-section represents the cross-sectional area hardened by the interaction of an incident ion with the target, and the hardening coefficient represents an index of the cross-sectional area gradient as a function of fluence.

Secondary conclusions are:

1. ERD has shown a loss of more than 50% hydrogen after ion irradiation. Hardness was also found to have an exponential dependence with H loss in the film.

2. XPS measurements indicated that in addition to the H content, C, O, and Si are the principal elements present in both the heat treated and ion irradiated films. For the heat treated films, the atomic ratio of O/Si was seen to increase from 1.4 to 1.8 for heat treatment temperatures from 300 °C to 800 °C, with this ratio increasing from 1.4 to 1.7 for the ion irradiated film. This movement is consistent with the films' evolution toward a silica based film. The atomic ratio of C/Si for films heat treated at 600 °C and higher, showed a significant reduction, which is consistent with the thermal decomposition of the Si-CH_3 and PVP organic components.

For the ion irradiated film, the atomic ratio of C/Si showed little change from that prior to irradiation.

3. Changes in photoluminescence response of the hybrid sol-gel films with respect to the heat treatment temperature, holding time, and ion irradiation were investigated. The luminescence response was found to be more intense in films heat treated at 300 °C, where a broad peak (FWHM 100 nm) centered at 510 nm (2.43 eV) and two sharper peaks centered at 445 nm (2.79 eV) and 470 nm (2.64 eV) were observed. As the films were heat treated at higher temperatures, the luminescence intensity decreased by a factor of approximately 30. The same trend was observed for heat treatment holding time longer than 10 minutes. For the ion irradiated films the photoluminescence response was observed to reach a maximum when the electronic energy deposited to the film surface was approximately 5 to 40 eV/atom. For higher values of electronic energy deposited the photoluminescence intensity decreased.

4. The measured reduced elastic modulus and hardness exhibited a substantial decrease with increase in contact depth, for ion irradiated films having a projected range smaller than the film thickness. The reduced elastic modulus and hardness depth profiles were influenced by the soft unirradiated sol-gel film underneath the irradiated hard surface layer.

5. It was observed that film shrinkage was correlated with a monotonic increase in hardness and reduced elastic modulus. Heat treating an ion irradiated film at 800 °C was found to cause an additional 30 % shrinkage of the irradiated film, but the hardness of the film decreased from 3.4 GPa to 0.8 GPa.

6. Raman spectroscopy confirmed the presence of carbon clusters in the form of amorphous carbon for films irradiated with fluences higher than 1 x 10^{16} ions/cm^2. The Raman shifts observed were centered at 1386 and 1584 cm^{-1}.

5.2 Future Work

- Perform ion irradiation using 125 keV H^+ ions with fluences of 0.01 and 3 x 10^{15} ions/cm^2, as well as 250 keV N^{2+} ions with fluences of 0.01, 0.1, and 3 x 10^{15} ions/cm^2. These experiments will allow for a more complete fitting of the hardness as a function of fluence by the model proposed in this study.

- In order to confirm the validity of the hardening model put forth, it is proposed that ion

irradiation be conducted using an ion with a large value of electronic stopping power (such as 61.2 eV/Å) for 2 MeV Cu^{2+} irradiation. This ion species was used in this study for a constant value of electronic energy deposited (1.87 x 10^{25} eV/cm^3). If this ion is used for the purpose of further validating the model, the fluence will need to be varied (with a possible range of 1 x 10^{13} to 5 x 10^{16} ions/cm^2) in order to determine the ion's hardening cross-section constant and hardening coefficient. The hardening cross-section constant is expected to be on the order of tens of $Å^2$ which is larger than the value obtained for the 250 keV N^{2+} irradiation.

- Perform ion irradiation with a lower electronic energy deposited on the film surface than the one used in this study in order to investigate the effect of ion irradiation on the photoluminescence response. As shown in this study, the photoluminescence spectra of ion irradiated films exhibited a maximum between 5 and 40 eV/atom (corresponding to 20 to 160 x 10^{22} eV/cm^3 for the films used in this study). For a future study it is proposed that 250 keV N^{2+} ions with fluences ranging from 8 x 10^{13} to 7 x 10^{14} ions/cm^2 be used.

- Perform a study on the variation of the molecular bonds in the film investigated by employing Fourier Transform InfraRed (FT-IR) spectroscopy. This future study could provide further evidence on the presence of cross-linking silica films.

- Investigate the thermal stability of the ion irradiated films by heat treating the films at temperatures ranging from 250 to 600 °C. Potential uses of such films are as mold coatings for injection molding of PMMA optical components with working temperatures of 230 °C and as mold coatings for hot-pressing production of glass lenses with an estimated working temperature of 580 °C.

- Modify the sol-gel films by X-ray. The X-ray mass absorption of silica film is reported to be 5.86 cm^2/g [115], thus the energy absorbed by the sol-gel film (1.1 g/cm^3 density and 600 nm thick) can be estimated to be 1 - exp[-(5.86)(1.1)(600 x 10^{-7})] = 4.9 x 10^{-4} multiplied by the incoming photon energy, i.e. 10 keV (0.124 nm wavelength). In order to excite the film with an energy per unit volume of 1.87 x 10^{25} ev/cm^3 (common electronic energy deposited used in this study), the photon dose can be estimated to be (1.87 x 10^{25} ev/cm^3)/(1 x 10^5 eV)(4.9 x 10^{-4}) = 3.8 x 10^{24} photons/cm^3.

Bibliography

[1] J. Livage, F. Beteille, C. Roux, M. Chatry, and P. Davidson. Sol-gel synthesis of oxide materials. *Acta Materialia*, 46(3):743–750, 1998.

[2] N.-L. Wu, S.-Y. Wang, and I.A. Rusakova. Inhibition of crystallite growth in the sol-gel synthesis of nanocrystalline metal oxides. *Science*, 285:1375–1377, 1999.

[3] W. Datchary, A. Mehner, H.-W. Zoch, D.A. Lucca, M.J. Klopfstein, R. Ghisleni, D. Grimme, and E. Brinksmeier. High precision diamond machining of hybrid sol-gel coatings. *Journal of Sol-Gel Science and Technology*, 35:245–251, 2005.

[4] S.I. Stupp and P.V. Braun. Molecular manipulation of microstructures: biomaterials, ceramics, and semiconductors. *Science*, 277:1242–1248, 1997.

[5] J.F. Gibbons. Ion implantetion in semiconductors - Part II: Damage production and annealing. *Proceedings IEEE*, 60(9):1062–1096, 1972.

[6] S. Jeong and J. Moon. Fabrication of refreactive index controllable inorganic-organic hybrid thick film. *Advanced Si-Based Ceramics and Composites Key Engineering Materials*, 287:69–74, 2005.

[7] A.B. Wojcik, A. Ting, and L.C. Klein. High molecular weight poly(ethylene oxide) / silica hybrids by the sol-gel process. *Materials Science and Engineering C*, C6:115–120, 1998.

[8] A. Conde, A. Duran, and J.J. De Damborenea. Polymeric sol-gel coatings as protective layers of aluminium alloys. *Progress in Organic Coatings*, 46:288–296, 2003.

[9] J. Malzbender and G. de With. Elastic modulus, hardness and fracture toughness of SiO_2-filled methyltrimethoxysilane coatings on glass substrates. *Journal of Non-Crystalline Solids*, 265:51–60, 2000.

[10] B.A. Latella, M. Ignat, C.J. Barbe, C.J. Cassidy, and H. Li. Cracking and delamination of sol-gel hybrid coatings on metallic substrates. *Journal of Sol-Gel Science and Technology*, 31:143–149, 2004.

[11] S. Pellice, U. Gilabert, C. Solier, Y. Castro, and A. Duran. Mechanical behavior of glass reinforced with SiO_2 hybrid sol-gel coatings. *Journal of Non-Crystalline Solids*, 348:172–179, 2004.

[12] G.R. Atkins, R.M. Krolikowska, and A. Samoc. Optical properties of an Ormosil system comprising methyl- and phenyl-substituted silica. *Journal of Non-Crystalline Solids*, 265:210–220, 2000.

[13] A. Matsuda, Y. Matsuno, M. Tatsumisago, and T. Minami. Fine patterning and characterization of gel films derived from methyltriethoxysilane and tetraethoxysilane. *Journal of American Ceramic Society*, 81(11):2849–2852, 1998.

[14] E.O. Oh, R.K. Gupta, and C.M. Whang. Effects of pH and dye concentration on the optical and structural properties of coumarin-4 dye-doped SiO_2-PDMS xerogels. *Journal of Sol-Gel Science and Technology*, 28:279–288, 2003.

[15] S. Yu, T.K.S. Wong, X. Hu, and M.S. Yong. Dielectric and mechanical properties of surface modified organosilicate films. *Journal of Sol-Gel Science and Technology*, 35:69–75, 2005.

[16] H. Izumi, H. Tanaka, Y. Uchida, N. Tohge, and T. Minami. Influence of firing conditions on adhesion of methytrialkoxysilane-derived coatings on steel sheets. *Journal of Non-Crystalline Solids*, 147-148:483–487, 1992.

[17] Y. Liu, W. Ren, L. Zhang, and X. Yao. New method for making porous SiO_2 thin films. *Thin Solid Films*, 353:124–128, 1999.

[18] P. Innocenzi, M.O. Abdirashid, and M. Guglielmi. Structure and properties of sol-gel coatings from methyltriethoxysilane and tetraethoxysilane. *Journal of Sol-Gel-Science and Technology*, 3:47–55, 1994.

[19] S. Santucci, S. Di Nardo, L. Lozzi, M. Passacantando, and P. Picozzi. XPS analysis on SiO_2 sol-gel thin films. *Journal of Electron Spectroscopy and Related Phenomena*, 76:623–628, 1995.

[20] M.T. Murtagh, M.R. Shahriari, and M. Krihak. A study of the effect of organic modification and processing technique on the luminescence quenching behavior of Sol-Gel oxygen sensors based on a Ru(II) complex. *Chemistry of Materials*, 10:3862–3869, 1998.

[21] M. Nocuń, E. Leja, J. Jedliński, and J. Najman. Structure and optical properties of hybrid glasses based on tetraethylorthosilicate-trimethoxyoctysilane and tetraethylorthosilicate-tetraethylorthotitanate-trimethoxyoctylsilane systems. *Journal of Molecular Structure*, 744-747:597–602, 2005.

[22] S. Fujihara and S. Kitta. Broadband visible emission from sol-gel-derived silica/poly(vinyl pyrrolidone) hybrids. *Chemical Physics Letters*, 397:479–483, 2004.

[23] H. Kozuka, S. Takenaka, H. Tokita, T. Hirano, Y. Higashi, and T. Hamatani. Stress and cracks in gel-derived ceramic coatings and thick film formation. *Journal of Sol-Gel Science and Technology*, 26:681–686, 2003.

[24] C.-K. Chan, I-M. Chu, C.-F. Ou, and Y.-W. Lin. Interfacial interactions and their influence to phase behavior in poly(vinyl pyrrolidone)/silica hybrid materials prepared by sol-gel process. *Materials Letters*, 58:2243–2247, 2004.

[25] K.S. Huang, E.C. Lee, and Y.S. Chang. Synthesis and characterization of soluble hybrids of poly(vinyl pyrrolidone) or its copolymer. *Journal of Applied Polymer Science*, 100:2164–2170, 2006.

[26] H. Kozuka, M. Kajimura, T. Hirano, and K. Katayama. Crack-free, thick ceramic coating films via non-repetitive dip-coating using polyvinylpyrrolidone as stress-relaxing agent. *Journal of Sol-Gel Science and Technology*, 19:205–209, 2000.

[27] T. Iwamoto and J.D. Mackenzie. Hard ormosils prepared with ultrasonic irradiation. *Journal of Sol-Gel Science and Technology*, 4:141–150, 1995.

[28] J.D. Mackenzie, Q. Huang, and T. Iwamoto. Mechanical properties of ormosils. *Journal of Sol-Gel Science and Technology*, 7:151–161, 1996.

[29] F. Mammeri, L. Rozes, C. Sanchez, and E. Le Bourhis. Mechanical properties of SiO_2-PMMA based hybrid organic-inorganic thin films. *Journal of Sol-Gel-Science and Technology*, 26:413–417, 2003.

[30] J.D. Mackenzie and E.P. Bescher. Physical properties of sol-gel coatings. *Journal of Sol-Gel Science and Technology*, 19:23–29, 2000.

[31] Y. Han, J. Lin, and H. Zhang. Photoluminescence of organic-inorganic hybrid SiO_2 xerogels. *Materials Letters*, 54:389–396, 2002.

[32] V. Pilla, A.A. Andrade, S.M. Lima, T. Catunda, D.A. Donatti, D.R. Vollet, and A.I. Ruiz. Spectroscopic and thermal characterization in poly(p-phenylene vinylene)/sol-gel silica sample. *Optical Materials*, 24:483–489, 2003.

[33] D. Pan, N. Zhao, Q. Wang, S. Jiang, X. Ji, and L. An. Facile synthesis and characterization of luminescent TiO_2 nanocrystals. *Advanced Materials*, 17:1991–1995, 2005.

[34] A. Anedda, C.M. Carbonaro, F. Clemente, R. Corpino, and P.C. Ricci. Mesoporous silica photoluminescence properties in samples with different pore size. *Materials Science and Engineering C*, 23:1073–1076, 2003.

[35] L.T. Canham, A. Loni, P.D.J. Calcott, A.J. Simons, C. Reeves, M.R. Houlton, J.P. Newey, K.J. Nash, and T.I. Cox. On the origin of blue luminescence arising from atmospheric impregnation of oxidized porous silicon. *Thin Solid Films*, 276:112–115, 1996.

[36] S.S. Yi, J.S. Bae, K.S. Shim, B.K. Moon, J.H. Jeong, S.T. Chung, and J.H. Kim. Luminescence characteristics of Eu-doped $GdVO_4$ thin films grown by pulsed-laser deposition. *Journal of Vacuum Science and Technology A*, 23(4):1124–1127, 2005.

[37] Y. Posada, L. San Miguel, L.F. Fonseca, O. Resto, S.Z. Weisz, C.-H. Kim, and J. Shinar. Optical properties of nanocrystalline silicon whitin silica gel monoliths. *Journal of Applied Physics*, 96(4):2240–2243, 2004.

[38] C.M. Carbonaro, F. Clemente, R. Corpino, P.C. Ricci, and A. Anedda. Ultraviolet photoluminescence of silanol species in mesoporous silica. *Journal of Physical and Chemistry B*, 109:14441–14444, 2005.

[39] Y. Ogawa and S. Fujihara. Band-gap modification and tunable blue luminescence of wurtzite $Mg_xZn_{1-x}O$ thin films. *Physica Status Solidi A*, 202(9):1825–1828, 2005.

[40] M.J. García, M.A. Mondragíon, C. Téllez, A. Campero, and V.M. Castaño. Blue emission in tetraethoxysilane and silica gels. *Materials Chemistry and Physics*, 41:15–17, 1995.

[41] V. Bekiari, P. Lianos, U.L. Stangar, B. Orel, and P. Judeinstein. Optimization of the intensity of luminescence emission from Silica/Poly(ethylene oxide) and Silica/Poly(propylene oxide) nanocomposite gels. *Chemistry of Materials*, 12:3095–3099, 2000.

[42] B.E. Yoldas. Photoluminescence in chemically polymerized SiO_2 and Al_2O_3-SiO_2 systems. *Journal of Materials Research*, 5(6):1157–1158, 1990.

[43] L.D. Carlos, R.A. Sá Ferreira, R.N. Pereira, M. Assunção, and V.de Zea Bermudes. White-light emission of amine-functionalized organic/inorganic hybrids: emitting centers and recombination mechanisms. *Journal of Physical and Chemistry B*, 108:14924–14932, 2004.

[44] A. Anedda, C.M. Carbonaro, F. Clemente, R. Corpino, and P.C. Ricci. Visible and ultraviolet emission of porous silica excited by synchrotron radiation. *Journal of Non-Crystalline Solids*, 351:1924–1927, 2005.

[45] W.H. Green, K.P. Le, J. Grey, T.T. Au, and M.J. Sailor. Whitephosphors from a silicate-carboxylate Sol-Gel precoursor that lack metal acticator ions. *Science*, 276:1826–1828, 1997.

[46] V. Bekiari and P. Lianos. Characterization of photoluminescence from a material made by interaction of (3-Aminopropyl)triethoxysilane with acetic acid. *Langmuir*, 14(13):3459–3461, 1998.

[47] R. Tohmon, Y. Shimogaichi, H. Mizuno, Y. Ohki, K. Nagasawa, and Y. Hama. 2.7-eV luminescence in as-manufactured high-purity silica glass. *Physical Review Letters*, 62(12):1388–1391, 1989.

[48] D.P. Yu, Q.L. Hang, Y. Ding, H.Z. Zhang, Z.G. Bai, J.J. Wang, Y.H. Zou, W. Qian, G.C. Xiong, and S.Q. Feng. Amorphous silica nanowires: Intensive blue light emitters. *Applied Physics Letters*, 73(21):3076–3078, 1998.

[49] Y.D. Glinka, S.-H. Lin, and Y.-T. Chen. The photoluminescence from hydrogen-related species in composites of SiO_2 nanoparticles. *Applied Physics Letters*, 75(6):778–780, 1999.

[50] Y.D. Glinka, S.-H. Lin, and Y.-T. Chen. Two-photon-excited luminescence and defect formation in SiO_2 nanoparticles induced by 6.4-eV ArF laser light. *Physical Review B*, 62(7):4733–4743, 2000.

[51] A.S. Zyubin, A.M. Mebel, S.H. Lin, and Y.D. Glinka. Photoluminescence of silanone and dioxasilyrane groups in silicon oxides: A theoretical study. *Journal of Chemical Physics*, 116(22):9889–9896, 2002.

[52] G. Schottner. Hybrid sol-gel derived polymers: applications of multifunctional materials. *Chemistry of Materials*, 13:3422–3435, 2001.

[53] H.Y. Jung, R.K. Gupta, E.O. Oh, Y.H. Kim, and C.M. Whang. Vibrational spectroscopic studies of sol-gel derived physical and chemical bonded ORMOSILs. *Journal of Non-Crystalline Solids*, 351:372–379, 2005.

[54] X. Li and T.A. King. Spectroscopic studies of sol-gel-derived organically modified silicates. *Journal of Non-Crystalline Solids*, 204:235–242, 1996.

[55] A. Anedda, C.M. Carbonaro, F. Clemente, R. Corpino, and P.C. Ricci. Raman investigation of surface OH-species in porous silica. *Journal of Physical and Chemistry B*, 107:13661–13664, 2003.

[56] G. Wang, L. Feng, R.L. Luck, D.G. Evans, Z. Wang, and X. Duan. Sol/gel synthesis, characterization and catalytic property of silicas modified with oxomolybdenum complexes. *Journal of Molecular Catalysis A: Chemical*, 241:8–14, 2005.

[57] G. Conti, Y. Uritsky, and C.R. Brundle. Application of micro-Raman and photoluminescence spectrsocopy to defect and thin film characterization. *Characterization and Metrology for ULSI Technology: 2000 International Conference*, pages 332–336, 2000.

[58] T. Venkatesan. High energy ion beam modification of polymer films. *Nuclear Instruments and Methods in Physics Research B*, 7/8:461–467, 1985.

[59] S.K. Srivastava, D.K. Avasthi, and J.C. Pivin. Mechanism of H release from Si-based polymers under ion irradiation. *Nuclear Instruments and Methods in Physics Research B*, 191:718–722, 2002.

[60] J.C. Pivin, P. Colombo, A. Martucci, G.D. Soraru, E. Pippel, and M. Sendova-Vassileva. Ion beam induced conversion of Si-based polymers and gels layers into ceramics coatings. *Journal of Sol-Gel Science and Technology*, 26:251–255, 2003.

[61] J.C. Pivin, P. Colombo, M. Sendova-Vassileva, J. Salomon, G. Sagon, and A. Quaranta. Ion-induced conversion of polysiloxanes and polycarbosilanes into ceramics: Mechanisms and properties. *Nuclear Instruments and Methods in Physics Research B*, 141:652–662, 1998.

[62] J.C. Pivin. Formation of nanostructures with a controlled size distribution in si-based gels by ion irradiation. *Materials Science-Poland*, 23(1):101–109, 2005.

[63] A. Kumar, F. Singh, J.C. Pivin, and D.K. Avasthi. Photoluminescence studies of carbon clusters formed by irradiation of Si-based polymer. *Radiation Measurements*, 40:785–788, 2005.

[64] A. Tripathi, A. Kumar, F. Singh, D. Kabiraj, D.K. Avasthi, and J.C. Pivin. Ion irradiation induced surface modification studies of polymers using SPM. *Nuclear Instruments and Methods in Physics Research B*, 236:186–194, 2005.

[65] J.C. Pivin and P. Colombo. Conversion of organic-inorganic polymers to ceramics by ion implantation. *Nuclear Instruments and Methods in Physics Research B*, 120:262–265, 1996.

[66] D.L. Baptista, C.E. Foerster, C.M. Lepienski, and F.C. Zawislak. Hard three-dimensional sp^2 carbon-bonded phase formed by ion beam irradiation of fullerene, a-C and polymeric a-C:H films. *Nuclear Instruments and Methods in Physics Research B*, 218:61–67, 2004.

[67] S.O. Cho and H.Y. Jun. Surface hardening of poly(methyl methacrylate) by electron irradiation. *Nuclear Instruments and Methods in Physics Research B*, 237:525–532, 2005.

[68] E.C. Rangel, N.C. Cruz, and C.M. Lepienski. Effect of helium implantation on the properties of plasma polymer films. *Nuclear Instruments and Methods in Physics Research B*, 191:704–707, 2002.

[69] J.C. Pivin, P. Viel, G. Zalczer, and G. Marletta. Effects of ionizations and displacements on the hardness and optical absorption of some ion irradiated polymers. *Nuclear Instruments and Methods in Physics Research B*, 105:192–196, 1995.

[70] J.C. Pivin, D.K. Avasthi, F. Singh, A. Kumar, E. Pippel, and G. Sagon. Precipitation of C, Si and metals nanoparticles in silicon-based gels induced by swift heavy ion irradiation. *Nuclear Instruments and Methods in Physics Research B*, 236:73–80, 2005.

[71] S.O. Kucheyev, T.E. Felter, M. Anthamatten, and J.E. Bradby. Deformation behavior of ion-irradiated polyimide. *Applied Physics Letters*, 85(5):733–735, 2004.

[72] C. Brun, M. Fromm, F. Berger, P. Delobelle, J. Takadoum, E. Beche, A. Chambaudet, and F. Jaffiol. Modifications of polypropylene surface properties by He^+ ion implantation. *Journal of Polymer Science*, 41:1183–1191, 2003.

[73] D.A. Lucca, M.J. Klopfstein, R. Ghisleni, A. Gude, A. Mehner, and W. Datchary. Investigation of sol-gel derived ZrO_2 thin films by nanoindentation. *Annals of CIRP*, 53(1):475–478, 2004.

[74] A. Mehner, W. Datchary, N. Bleil, M.J. Klopfstein, and D.A. Lucca. The influence of sol-gel processing parameters on crack formation, microstructure, density and hardness of sol-gel derived zirconia films. *Journal of Sol-Gel-Science and Technology*, 36(1):25–32, 2005.

[75] J.F. Ziegler. SRIM, www.srim.org, 2003.

[76] B. Bhushan. Nanomechanical properties of solid surfaces and thin films. In *Handbook of Micro/Nanotribology*, pages 321–396. CRC Press, Inc., 1995.

[77] J.L. Loubet, J.M. Georges, O. Marchesini, and G. Meille. Vickers indentation curves of magnesium oxide (MgO). *Journal of Tribology*, 106:43–48, 1984.

[78] M.F. Doerner and W.D. Nix. A method for interpreting the data from depth-sensing indentation instruments. *Journal of Materials Research*, 1:601–609, 1986.

[79] S.V. Hainsworth, H.W. Chandler, and T.F. Page. Analysis of nanoindentation load-displacement loading curves. *Journal of Materials Research*, 11, 1996.

[80] W.C. Oliver and G.M. Pharr. An improved technique for determining hardness and elastic modulus using load and displacement sensing indentation experiments. *Journal of Materials Research*, 7:1564–1583, 1992.

[81] J. Woirgard and J-C. Dargenton. An alternative method for penetration depth determination in nanoindentation measurements. *Materials Research Society*, 12:2455–2458, 1997.

[82] F.F. Ling, W.M. Lai, and D.A. Lucca. *Fundamentals of Surface Mechanics with Applications*. Springer-Verlag, New York, 2002.

[83] K.L. Johnson. *Contact Mechanics*. Cambridge University Press, Cambridge, 1985.

[84] A.E.H. Love. Boussinesq's problem for a rigid cone. *Quarterly Journal of Mathematics (Oxford)*, 10:161–175, 1939.

[85] I.N. Sneddon. The relation between load and penetration in the axisymmetric Boussinesq problem for a punch of arbitrary profile. *International Journal of Engineering Science*, 3:47–57, 1965.

[86] D. Tabor. A simple theory of static and dynamic hardness. *Proceedings of the Royal Society A*, page 247, 1948.

[87] R.B. King. Elastic analysis of some punch problems for a layered medium. *International Journal of Solids and Structures*, 23:1657–1664, 1987.

[88] J.B. Pethica, R. Hutchings, and W.C. Oliver. Hardness measurement at penetration depths as small as 20 nm. *Philosophical Magazine A*, 48:593–606, 1983.

[89] L.E. Seitzman. Mechanical properties from instrumented indentation: Uncertainties due to tip-shape correction. *Journal of Materials Research*, 13:2936–2944, 1998.

[90] D.W. Hamby. *Effects of surface damage on the photoluminescence of ZnO*. Dissertation, Oklahoma State University, 2003.

[91] K.G. Budinski and M.K. Budinski. *Engineering Materials Properties and Selection*. Prentice Hall, New Jersey, 8th edition, 2004.

[92] L.S. Ornstein and U. Rekveld. Intensity measurements in the Raman effect and the distribution law of Maxwell-Boltzmann. *Physical Review*, 34:720–725, 1929.

[93] Raymund Kwok. Xpspeak, 2000.

[94] D. Briggs. *Surface analysis of polymers by XPS and static SIMS*. Cambridge University Press, Cambridge UK, 1998.

[95] R. Ghisleni, L. Shao, D.A. Lucca, V. Doan, M. Nastasi, J. Dong, and A. Mehner. Effects of heat treatment and ion irradiation on hybrid organic/inorganic sol-gel derived thin films. *Nuclear Instruments and Methods in Physics Research B*, xxx:in press, 2007.

[96] J.C. Pivin, P. Colombo, and G.D. Soraru. Comparison of ion irradiation effects in silicon-based preceramic thin films. *Journal of American Ceramic Society*, 83(4):713–720, 2000.

[97] K. Manzoor, S.R. Vadera, N. Kumar, and T.R.N. Kutty. Energy transfer from organic surface adsorbate-polyvinyl pyrrolidone molecules to luminescent centers in ZnS nanocrystals. *Solid State Communications*, 129:469–473, 2004.

[98] G. Allan, C. Delerue, and M. Lannoo. Quantum confinement in amorphous silicon layers. *Applied Physics Letters*, 71(9):1189–1191, 1997.

[99] M.V. Wolkin, J. Jorne, P.M. Fauchet, G. Allan, and C. Delerue. Electronic states and luminescence in porous silicon quantum dots: the role of oxygen. *Physical Review Letters*, 82(1):197–200, 1999.

[100] I. Barin and O. Knacke. *Thermochemical properties of inorganic substances*. Springer-Verlag, Berlin, 1973.

[101] D.A. Lucca, R. Ghisleni, M. Nastasi, L. Shao, Y.Q. Wang, J. Dong, and A. Mehner. Effect of ion implantation on the surface mechanical properties of sol-gel derived TEOS/MTES thin films. *Nuclear Instruments and Methods in Physics Research B*, 257:577–580, 2007.

[102] J.W. Park, C.W. Sohn, and B.H. Choi. Some characteristics of materials surface-modified by ions beam bombardment. *Current Applied Physics*, 6:188–193, 2006.

[103] M. Guenther, G. Gerlach, G. Suchaneck, K. Sahre, K.-J. Eichhorn, B. Wolf, A. Deineka, and L. Jastrabik. Ion-beam induced chemical and structural modification in polymers. *Surface and Coatings Technology*, 158-159:108–113, 2002.

[104] I. Manika and J. Maniks. Size effect in micro- and nanoscale indentation. *Acta Materialia*, 54:2049–2056, 2006.

[105] H Buckle. Progress in microindentation hardness testing. *Metallurgical Reviews*, 4:49–100, 1959.

[106] J.C. Pivin and P. Colombo. Ceramic coatings by ion irradiation of polycarbosilanes and polysiloxanes. part I Conversion mechanism. *Journal of Materials Science*, 32:6163–6173, 1997.

[107] M.P. de Jong, A.J.H. Maas, L.J. van Ijzendoorn, S.S. Klein, and M.J.A. de Voigt. A model for ion-irradiation induced hydrogen loss from organic materials. *Journal of Applied Physics*, 82(3):1058–1064, 1997.

[108] A. Taniike, N. Kubota, M. Takeuchi, Y. Furuyama, and A. Kitamura. Ion-irradiation induced hydrogen loss from polyethylene film. *Journal of Applied Physics*, 92(11):6489–6494, 2002.

[109] R. Ghisleni, D.A. Lucca, M. Nastasi, L. Shao, Y.Q. Wang, J. Dong, and A. Mehner. Effect of electronic stopping on the irradiation-induced changes in hybrid modified silicate thin films. *Nuclear Instruments and Methods in Physics Research B*, 257:581–584, 2007.

[110] G.D. Sorarù, G. D'Andrea, and A. Glisenti. XPS characterization of gel-derived silicon oxycarbide glasses. *Materials Letters*, 27:1–5, 1996.

[111] M. Nocuń, E. Leja, and W. Bugajski. Microstructure and optical properties of methylmethacrylate-modified silica hybrid glasses and thin films. *Materials Science*, 21(4):471–479, 2003.

[112] A.S.M. Chong and X.S. Zhao. Functionalization of SBA-15 with APTES and characterization of functionalized materials. *Journal of Physical and Chemistry B*, 107:12650–12657, 2003.

[113] J. Gallardo, A. Duran, D. Di Martino, and R.M. Almeida. Structure of inorganic and hybrid SiO_2 sol-gel coatings studied by variable incidence infrared spectroscopy. *Journal of Non-Crystalline Solids*, 298:219–225, 2002.

[114] K.E. Sickafus. Introduction to mathematical models for irradiation-induced phase transformations. In K.E. Sickafus, E.A. Kotomin, and B.P. Uberuaga, editors, *Radiation effects in solids*. Springer, Dordrecht, 2006.

[115] B.R. Jr. Roof. X-ray absorption coefficients of the elements with Z = 1 to 17 for Mo K_α radiation. *Physical Review*, 113(3):826–827, 1959.

[116] M. Nastasi, J.W. Mayer, and J.K. Hirvonen. *Ion-solid interactions*. Cambridge Solid State Science Series. Cambridge University Press, Cambridge, 1996.

[117] N. Bohr. Velocity-range relation for fission fragments. *Physical Review*, 59:270–275, 1941.

[118] O.B. Firsov. A qualitative interpretation of the mean electron excitation energy in atomic collisions. *Soviet Physics JETP*, 36:1076, 1959.

Appendix A

Molecular Structures

An estimate of the film density, for sol-gel films heat treated at 300 °C, was made using the measured film thickness, the areal dimensions of the film, and the measured weight gain after coating and found to be 1.1 g/cm^3. This corresponds to an atomic density of 3.98 x 10^{22} atoms/cm^3 in the case of 48 at.% C, 31 at.% O, and 21 at.% Si (as measured by XPS).

MTES

Name: Methyltriethoxysilane

CAS number: 2031-67-6

Formula: $(CH_3)Si(OC_2H_5)_3$

Structure: Figure A.1

TEOS

Name: Tetraethylorthosilane or Tetraethoxysilane

CAS number: 78-10-4

Formula: $Si(OC_2H_5)_4$

Structure: Figure A.2

PVP

Name: Polyvinylpyrrolidone

CAS number: 9003-39-8

Formula: $(C_6H_9NO)_n$

Structure: Figure A.4

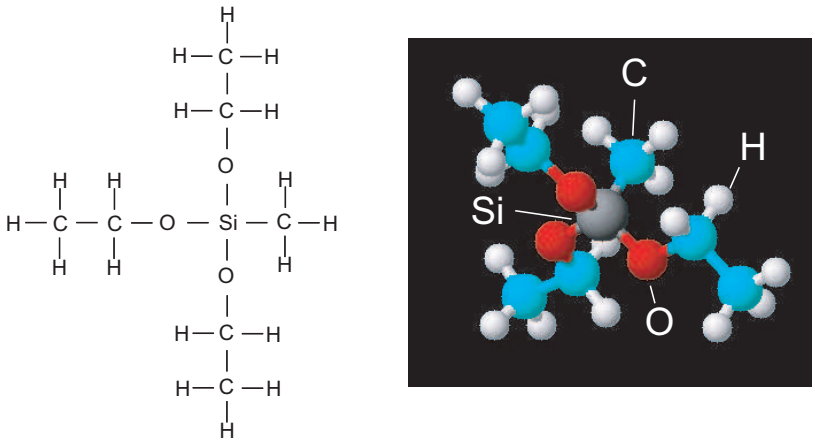

Figure A.1: MTES (Methyltriethoxysilane) molecular structure.

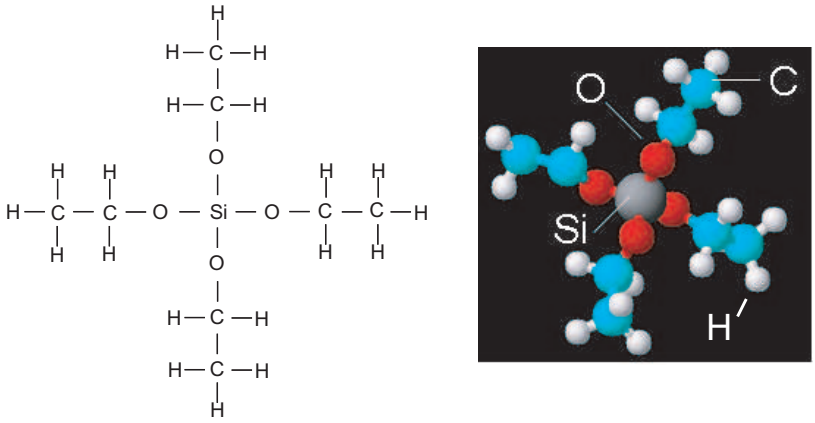

Figure A.2: TEOS (Tetraethylorthosilane or Tetraethoxysilane) molecular structure.

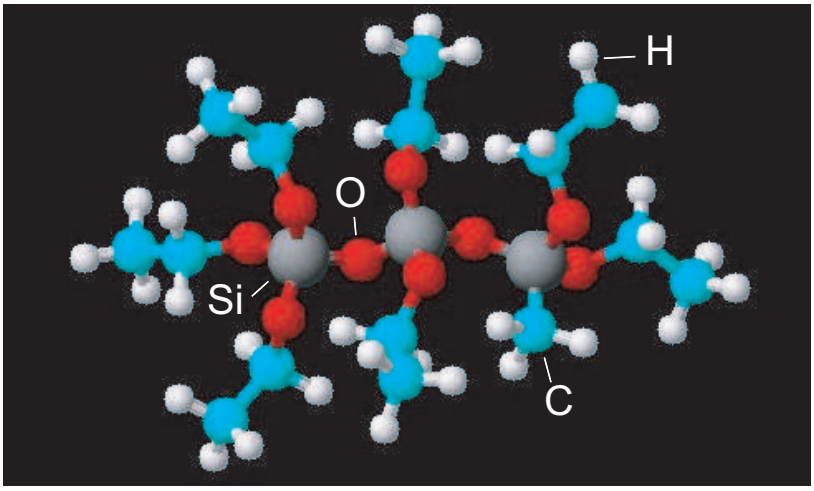

Figure A.3: MTES/TEOS hydrolysis and condensation.

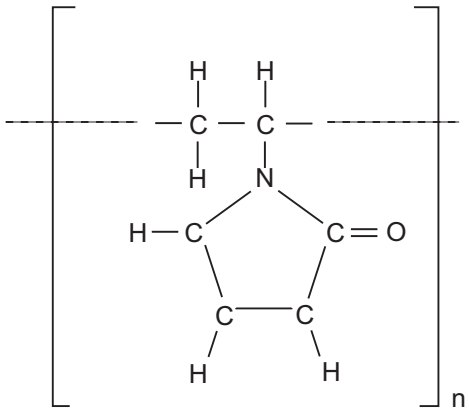

Figure A.4: PVP (Polyvinylpyrrolidone) molecular structure.

Appendix B

Electronic Stopping

Since the electronic stopping power is identified to be the dominating irradiation variable on the hardness increase of the sol-gel films investigated, a description on soft collision is reported by reviewing the "Ion-Solid Interactions" book by Nastasi et al. [116].

Based on the Thomas-Fermi description of the atom, Bohr [117] suggested that the ion charge fraction, or the effective ion charge, should be given by

$$\frac{Z_1^*}{Z_1} = \left(\frac{v_1}{v_0 Z_1^{2/3}} \right) \tag{B.1}$$

where Z_1^* is the incident ion ionization, Z_1 is the atomic number of the incident ion, v_1 is the incident ion velocity, and v_0 is the Bohr velocity (2.188 x 10^6 m/s).

From the above equation, two velocity regimes can be distinguished into: a) high-energy electronic energy-loss, $Z_1^*/Z_1 < 1$, where the incident ion is not fully stripped by the interaction with the target, thus the ion carried its electrons and neutralizes by capturing electrons from the target material, and b) low-energy electronic energy-loss, $Z_1^*/Z_1 \cong 1$, where the incident ion is fully stripped by the interaction with the target, thus the ion can be seen as a positive charge Z_1 moving with a velocity higher than the target electrons.

In the experiments conducted in this study all ion irradiation falls into the low-energy electronic energy-loss velocity regime, except for H^+ irradiation.

For 125 keV H^+ irradiation, even though the velocity of the incident ion (4.89 x 10^7 m/s, ion mass: 1.6726 x 10^{-27} kg) is greater than the Bohr velocity (2.188 x 10^6 m/s), the incident ion is initially fully stripped. Thus the irradiation is seen to be carried out by a positive charge moving with a velocity higher than the target electrons, the resulting collision can be described as pure Coulomb interaction potential.

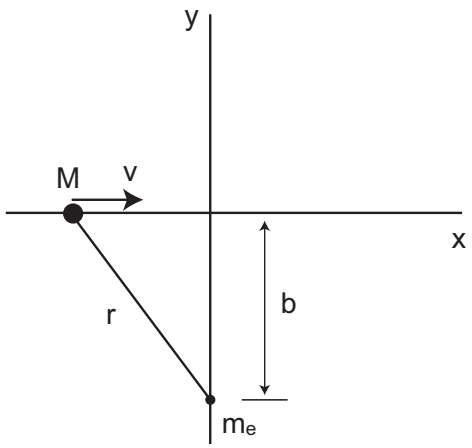

Figure B.1: Diagram for momentum (impulse) between an incident ion of mass M and a target electron of mass m_e.

The kinetic energy, T, transfered to the target electrons from the incident ion can be evaluated as:

$$T = \frac{\Delta p^2}{2m_e} \tag{B.2}$$

where Δp is the momentum transferred to the target electron by the incident ion, and m_e is the target electron mass. Δp can be obtained by integrating the Coulomb interaction force, F_0, between the incident ion and the target electron with respect to time, giving:

$$\begin{aligned} \Delta p &= \int_{-\infty}^{\infty} F_0 dt \\ \Delta p &= \frac{1}{v}\int_{-\infty}^{\infty} F_0 dx \end{aligned} \tag{B.3}$$

F_0 can be calculated using the diagram in Figure B.1 as

$$F_0 = -\frac{dV(r)}{dy} = -\frac{dV((x^2+b^2)^{1/2})}{db} \tag{B.4}$$

where $V(r)$ is the interaction potential, thus

$$\Delta p = -\frac{1}{v}\frac{d}{db}\int_{-\infty}^{\infty} V((x^2+b^2)^{1/2})dx \tag{B.5}$$

Since the interaction potential is considered to be purely Coulombic, the potential $V(r)$ can be expressed by

$$V(r) = k_c \frac{Z_1 Z_2 e^2}{r} \tag{B.6}$$

where k_c is the Coulomb force constant (8.988 x 10^9 Nm^2C^{-2}), e the unit charge (1.602 x 10^{-19} C), and $r = (x^2 + b^2)^{1/2}$, thus

$$\Delta p = k_c \frac{Z_1 Z_2 e^2}{vb} \int_{-\infty}^{\infty} \frac{b^2}{(x^2+b^2)^{3/2}} dx = k_c \frac{2Z_1 Z_2 e^2}{vb} \tag{B.7}$$

Substituting Δp into Equation B.2 it is obtained:

$$T = k_c^2 \frac{2Z_1^2 e^4}{m_e v^2 b^2} \tag{B.8}$$

In the case of 125 keV (2 x 10^{-14} J) H^+ irradiation, $Z_1 = 1$, $m_e = 9.1095$ x 10^{-31} kg, $e = 1.602$ x 10^{-19} C, $k_c = 8.988$ x 10^9 Nm^2C^{-2}, $v = \sqrt{2E/M} = \sqrt{2(2\,\text{x}\,10^{-14}\text{J})/1.6726\,\text{x}\,10^{-27}\text{kg}} = 4.89$ x 10^7 m/s (M mass of the incident ion, 1.6726 x 10^{-27} kg) at the surface, thus

$$T = \frac{4.88\,\text{x}\,10^{-41}\text{J m}^2}{b^2} = \frac{3.05\,\text{x}\,10^{-2}\text{eV Å}^2}{b^2} \tag{B.9}$$

and the value for b can be estimated at 0.5 Å for a fluence of 1 x 10^{16} ions/cm^2 ($\sqrt{1\,\text{x}\,10^{16}}$ ions/cm = 1 ion/Å). Then the kinetic energy lost by the incident ion and gained by the target electron is on the order of 0.12 eV. This energy is lower than the ionization energy of any atom present in the sol-gel film, thus this energy is not high enough to strip an electron from the target atom.

In the case of a hard collision between the incident H^+ ion and the target electron, the kinetic energy transfered to the target electron can be calculated as:

$$T = \frac{1}{2} m_e \Delta v_e^2 \tag{B.10}$$

where the variation in velocity of the target electron Δv_e, is

$$\Delta v_e = \left(\frac{2M}{M + m_e} \right) v + \left(\frac{m_e - M}{M + m_e} - 1 \right) v_{ei} \tag{B.11}$$

where v is the initial velocity (prior collision) of the incoming ion and v_{ei} is the initial electron velocity, which can be assumed negligible with respect to the velocity of the ion, thus

$$T = \frac{1}{2} m_e \left(\frac{2M}{M + m_e} v \right)^2 \tag{B.12}$$

where M is the ion mass, $2.32587\,\text{x}\,10^{-27}$ kg, which is 5 orders of magnitude greater than the electron mass m_e, $9.1095\,\text{x}\,10^{-31}$ kg, thus the above equation can be reduced to:

$$\begin{aligned} T &= \frac{1}{2} m_e (2v)^2 \\ T &= 2(9.1095\,\text{x}\,10^{-31}\,\text{kg}) \left(4.89\,\text{x}\,10^7\,\text{m/s}\right)^2 = 4.35\,\text{x}\,10^{-15}\,\text{J} = 2.7\,\text{x}\,10^5\,\text{eV} \end{aligned} \tag{B.13}$$

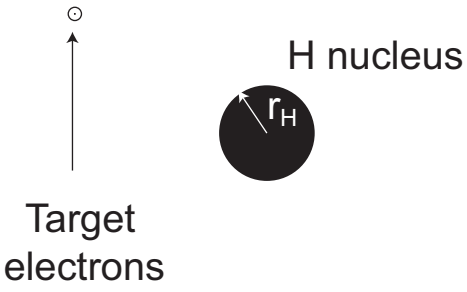

Figure B.2: Sketch used to determine the probability of a hard collision between the incoming H^+ ion and the target electron. Assuming this entire page to represent the area affected by the incoming ion, 1 $Å^2$, then the probability that the target electron gets hit by the incoming ion is the ratio between the ion cross-sectional area, circular area of radius r_H, and the area affected by the incoming ion.

the kinetic energy determined using Equation B.13 is transfered to the target electron due to the hard collision and causes the electron to be stripped from the target atom it belongs to.

The probability, p_H, that a hard collision between the incoming ion and the target electron takes place can be calculated as the ratio between the ion cross-sectional area, circular area of radius r_H (1.2 x 10^{-3} Å), and the area affected by the incoming ion, circular area of radius r_i, assumed to be a circular area of 1 $Å^2$ for the case of 1 x 10^{16} ions/cm^2 fluence:

$$p_H = \frac{\pi r_H^2}{\pi r_i^2} \,\mathrm{x}\, 100 = \frac{\pi\,(1.2\,\mathrm{x}\,10^{-3}\,Å)^2}{1\,Å^2}\,\mathrm{x}\,100 = 4.5\,\mathrm{x}\,10^{-4}\,\% \tag{B.14}$$

From this value of probability, hard collisions can be neglected.

The electronic energy loss per unit thickness traveled by a 125 keV H^+ ion is 6.5 eV/Å (this value can be assumed constant for the entire film thickness, 600 nm), evaluated using the simulation software SRIM [75]. The following equations will be used to verify that this value is equal to the integration of Equation B.9 with respect to b, the distance between the incoming ion and the electron:

$$\left.\frac{dE}{dx}\right|_e = \int_{r_{min}}^{r} T\rho_e 2\pi b db = \int_{r_{min}}^{r} \frac{3.05\,\mathrm{x}\,10^{-2}\mathrm{eV}\ Å^2}{b}\rho_e 2\pi db \cong 1.9\,\mathrm{x}\,10^{-1}\mathrm{eV}\ Å^2 \rho_e ln(r) = 6.5\,\mathrm{eV/Å} \tag{B.15}$$

where ρ_e is the electronic density estimated to be 8 electrons/$Å^3$ (the atomic density of the film estimated by XPS measurements is 4 x 10^{23} atoms/cm^3, where every atom has an average of 20

electrons), thus

$$ln(r) = \frac{6.5\,\text{eV/Å}}{(1.9\,\text{x}\,10^{-1}\text{eV Å}^2)\,(8\,\text{electrons /Å}^3)} \tag{B.16}$$

$$r = e^{4.27} = 72\,\text{Å}$$

where r is the radius of the area affected by the incoming ion, which is a reasonable value, confirming the validity of the calculation of the energy loss by the ion due to a soft collision.

In the case of 250 keV (4 x 10^{-14} J) N^{2+} ion irradiation, the majority of the target electrons move faster than the ions (low-energy electronic energy-loss velocity regime). For ions moving in this velocity regime, the collision energy has been assumed to arise from the work involved in the transfer of momentum as target electron are picked up or captured by the incident ion, as described by Firsov's model [118]. The energy transfered to the target electron is proportional to $m_e v$ (m_e denotes the electron mass, and v denotes the ion velocity) since the captured electron has to be accelerated up to the ion velocity. The ion velocity can be calculated to be $v = \sqrt{2E/M} = \sqrt{2(4\,\text{x}\,10^{-14}\text{J})/2.32587\,\text{x}\,10^{-26}\text{kg}} = 1.85$ x 10^6 m/s, meaning the energy involved in this collisions is on the order of 5 x 10^{-5} eV.

For a hard collision between the incident N^{2+} ion and the target electron, the target electron has a higher velocity than the incoming ion, thus the kinetic energy transfered to the target electron can be calculated as:

$$T = \frac{1}{2}m_e\Delta v_e^2 = \frac{1}{2}m_e\left(\left(\frac{2M}{M+m_e} - 1\right)v_{ei}\right)^2 \tag{B.17}$$

since M, $2.32587\,\text{x}\,10^{-27}$ kg, is 5 orders of magnitude greater than m_e, $9.1095\,\text{x}\,10^{-31}$ kg, the above equation can be reduced to:

$$T = \frac{1}{2}m_e v_{ei}^2 \tag{B.18}$$
$$T = \frac{1}{2}\left(9.1095\,\text{x}\,10^{-31}\,\text{kg}\right)\left(8.01\,\text{x}\,10^6\,\text{m/s}\right)^2 = 2.92\,\text{x}\,10^{-17}\,\text{J} = 1.8\,\text{x}\,10^3\,\text{eV}$$

similar to hard collision between the incident H^+ ion and the target electrons, the energy transfered to the target electron due to the collision causes the electron to be tripped from the target atom it belongs to.

The probability, p_N, that a hard collision between the incoming ion and the target electron takes place can be calculated as the ratio between the ion cross-sectional area, circular area of radius r_N

(1.3 x 10^{-2} Å), and the area affected by the incoming ion, circular area of radius r_i, assumed to be a circular area of 1 $Å^2$ for the case of 1 x 10^{16} ions/cm^2 fluence.

$$p_N = \frac{\pi r_N^2}{\pi r_i^2} \,\mathrm{x}\, 100 = \frac{\pi\,(1.3\,\mathrm{x}\,10^{-2}\,Å)^2}{1\,Å^2} \,\mathrm{x}\, 100 = 5.3\,\mathrm{x}\,10^{-2}\,\% \tag{B.19}$$

also for this case the probability that a hard collision takes place is very small. Suggesting that the incoming ion loses energy by moment transfer to the target electrons, as suggested by Firsov's model [118].

VITA

Rudy Ghisleni

Candidate for the Degree of

Doctor of Philosophy

Thesis: EFFECTS OF ION IRRADIATION ON THE SURFACE MECHANICAL BEHAVIOR OF HYBRID SOL-GEL DERIVED SILICATE THIN FILMS

Major Field: Mechanical Engineering

Biographical:

Personal Data: Born in Osio Sotto, Bergamo, Italy on September 12, 1976, the son of Maurizio Ghisleni and Loredana Poli

Education: Graduated from I.T.I.S. "P. Paleocapa" High School, Bergamo, Italy in June 1995; attended 4 years of university in Italy before entering in a program of double degree: Master of Science degree with a major in Mechanical Engineering at Oklahoma State University in August, 2001 and Laurea in Mechanical Engineering at Politecnico di Milano, Milano, Italy, in July, 2002. Completed the requirements for the Doctor of Philosophy degree with a major in Mechanical Engineering at Oklahoma State University in May, 2007.

Experience: Employed by Oklahoma State University, Stillwater, Department of Mechanical and Aerospace Engineering as graduate research assistant - 2000 to 2001 and 2003 to present.

Professional Memberships: American Society for Precision Engineering; Honor Society of Phi Kappa Phi.

Name: Rudy Ghisleni Date of Degree: May, 2007

Institution: Oklahoma State University Location: Stillwater, Oklahoma

Title of Study: EFFECTS OF ION IRRADIATION ON THE SURFACE MECHANICAL BEHAVIOR OF HYBRID SOL-GEL DERIVED SILICATE THIN FILMS

Pages in Study: 103 Candidate for the Degree of Doctor of Philosophy

Major Field: Mechanical Engineering

A study on the effects of ion irradiation on the surface mechanical behavior of hybrid sol-gel derived thin films has been performed. Hybrid organic/inorganic modified silicate thin films were synthesized by sol-gel processing from tetraethoxysilane (TEOS) and methyltriethoxysilane (MTES) precursors and spin-coated onto (100) Si substrates. The synthesized films were investigated by nanoindentation, photoluminescence spectroscopy, and Raman spectroscopy.

Hybrid TEOS/MTES sol-gel films modified by ion irradiation with deposited electronic energies of 1.87 x 10^{25} eV/cm^3 or higher showed higher values of reduced elastic modulus and hardness than 800 ^{o}C heat treated films. Thus, ion irradiation was found to be an effective means in converting the polymer sol into ceramic type coatings. The ions used in this study were Cu^{2+}, N^{2+}, Si^{+}, O^{+}, N^{+}, He^{+}, and H^{+}, with incident energies ranging from 100 keV to 2 MeV, and fluences ranging from 1 x 10^{14} to 1 x 10^{17} ions/cm^2.

Both the reduced elastic modulus and hardness were seen to increase monotonically with the increase in ion fluence, with an observed maximum hardness of 7.7 GPa (an unirradiated film hardness was 0.4 GPa) and a maximum reduced elastic modulus of 84.0 GPa (an unirradiated film reduced elastic modulus was 7.1 GPa) for 250 keV N^{2+} irradiation with a 5 x 10^{16} ions/cm^2 fluence. The electronic stopping power was found to be principally responsible for the film hardening, while the role of nuclear stopping power was minimal. A monotonic increase in hardness with increase in electronic energy deposited to the film surface was found.

A model describing the hardening of ion irradiated films was developed. This model characterizes the hardening effectiveness of the ion species considered by two parameters: the constant hardening cross-section and the hardening coefficient. Where the hardening cross-section represents the cross-sectional area hardened by the interaction of an incident ion with the target, and the hardening coefficient represents an index of the cross-sectional area gradient as a function of fluence.

The increase in hardness of hybrid sol-gel films following ion irradiation was linked to structural changes. Ion irradiation results in a cross-linked silica film as well as the segregation of amorphous carbon clusters, both of which contributed to increase the mechanical properties of the films.

ADVISOR'S APPROVAL: Don A. Lucca